Light-induced Electrokinetics: A path to a versatile micro total analysis system

Justin K Valley
Ming C. Wu, Ed.

Electrical Engineering and Computer Sciences
University of California at Berkeley

Technical Report No. UCB/EECS-2011-34
http://www.eecs.berkeley.edu/Pubs/TechRpts/2011/EECS-2011-34.html

April 26, 2011

Acknowledgement

Acknowledgments are too long too list here, please see main text.

Light-induced Electrokinetics: A path to a versatile micro total analysis system

by

Justin K. Valley

A dissertation submitted in partial satisfaction of the

requirements for the degree of

Doctor of Philosophy

in

Engineering - Electrical Engineering and Computer Sciences

and the Designated Emphasis in

Nanoscale Science and Engineering

in the

Graduate Division

of the

University of California, Berkeley

Committee in charge:

Professor Ming C. Wu, Chair
Professor Michel M. Maharbiz
Professor Amy E. Herr

Spring 2011

The thesis of Justin K. Valley, titled Light-induced Electrokinetics: A path to a versatile micro total analysis system, is approved:

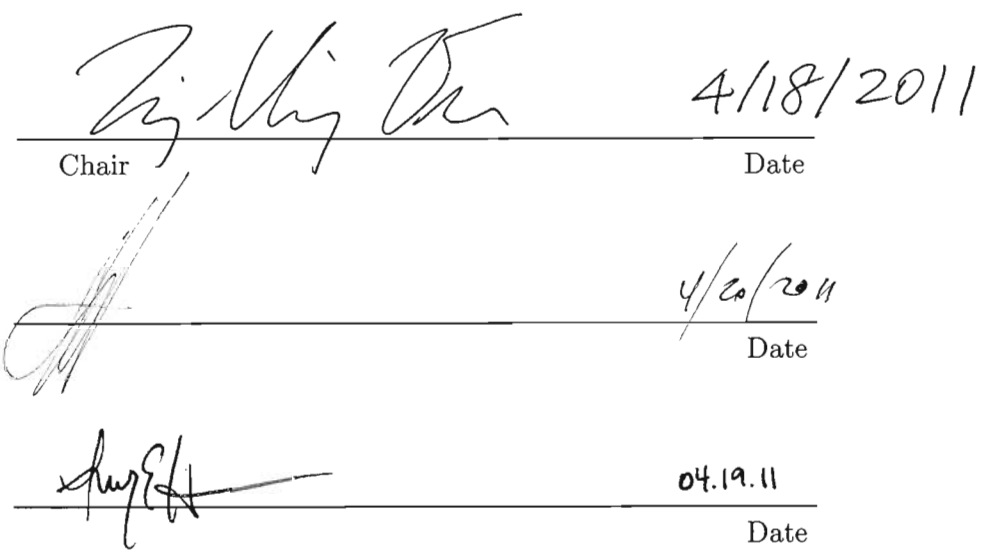

University of California, Berkeley

Spring 2011

Light-induced Electrokinetics: A path to a versatile micro total analysis system

Abstract

Light-induced Electrokinetics: A path to a versatile micro total analysis system

by

Justin K. Valley

Doctor of Philosophy in Engineering - Electrical Engineering and Computer Sciences
and the Designated Emphasis in Nanoscale Science and Engineering

University of California, Berkeley

Professor Ming C. Wu, Chair

The micro total analysis system (μTAS) has seen great interest and advances since its definition over two decades ago. By harnessing the fabrication tools of the semiconductor industry and exploiting the unique physical phenomena that dominate at the micro- to nano-scale, these devices aim to address applications ranging from point-of-care diagnostics to pharmaceutical development. A truly versatile μTAS technology platform will enable reconfigurable, parallel, and high resolution analysis, processing, and sorting/purification. To this end, we present the concept of light-induced electrokinetics, which enables the patterning of electric fields using low-intensity light. This platform allows for the manipulation of both fluids (optoelectrowetting (OEW)) and particles (optoelectronic tweezers (OET)) over a featureless substrate. In this work, we will discuss three examples of how this technology demonstrates each of the μTAS requirements. Specifically, we will use this platform to assess the developmental potential of preimplantation-stage embryos, perform high throughput light-induced electroporation of single cells, and, finally, demonstrate the ability to unify the OET and OEW device enabling both droplet and particle manipulation on a single device. Within the context of these examples, the potential of light-induced electrokinetics as a generic μTAS platform is elucidated.

If I have seen a little further it is by standing on the shoulders of Giants.

Letter from Isaac Newton to Robert Hooke, 1676.

This work is dedicated to all those Giants...

Contents

List of Figures **v**

List of Tables **vii**

1 Introduction **1**

2 Light-induced Electrokinetics **5**
2.1 Motivation . . . 5
2.1.1 Optical particle manipulation . . . 5
2.1.2 Droplet manipulation . . . 7
2.2 Physical forces present in the OET Device . . . 8
2.2.1 Light-Induced Dielectrophoresis . . . 8
2.2.2 A Brief Note on DEP and Optical Tweezers in the Rayleigh Limit . . . 14
2.2.3 Light-induced AC Electro-osmosis (LACE) . . . 15
2.2.4 Electro-thermal Effects (ET) . . . 19
2.2.5 Buoyancy Effects . . . 21
2.2.6 Development of a Figure of Merit . . . 24
2.2.7 Experimental Methods and Results . . . 26
2.2.8 Summary of Physical Effects in OET . . . 29
2.3 Light-induced Electrowetting . . . 31
2.3.1 Theory of Electrowetting . . . 31
2.3.2 Light-induced Electrowetting in OEW . . . 35

3 Pre-implantation Mouse Embryo Selection Guided by Light-Induced Dielectrophoresis **37**
3.1 Motivation . . . 37
3.2 Experimental Design Methodology . . . 39
3.3 Experimental Results . . . 42
3.3.1 DEP Response of Pre-implantation Mouse Embryos . . . 42
3.3.2 Effects of OET Assay on *in vitro* Embryo Viability . . . 44
3.3.3 Effects of OET Assay on Pup Yield . . . 44
3.3.4 Parallel Manipulation of Embryos . . . 46

3.3.5 Discussion . . . 47
3.4 Summary . . . 49

4 OET Assisted Electroporation **51**
4.1 Motivation . . . 51
4.2 Electroporation Theory: Energetics . . . 53
4.2.1 Membrane Pore Energy . . . 53
4.2.2 Effects on Membrane Pore Energy Landscape through Application of an Electric Field . . . 55
4.3 Device Operation and Experimental Results . . . 58
4.3.1 Electrode-based Electroporation . . . 58
4.3.2 Light-induced Electroporation . . . 60
4.4 Discussion . . . 71
4.5 Summary . . . 72

5 A Unified Platform for Optoelectrowetting and Optoelectronic Tweezers **74**
5.1 Motivation . . . 74
5.2 Device Operation . . . 75
5.3 Materials and Methods . . . 79
5.3.1 Device Fabrication . . . 79
5.3.2 Sample Preparation . . . 79
5.3.3 Experimental Setup . . . 79
5.4 Results and Discussion . . . 80
5.4.1 Speed vs. Frequency Characterization . . . 80
5.4.2 Particle Concentration . . . 80
5.4.3 Serial Particle Concentration . . . 82
5.4.4 Single Cell Selection and Encapsulation . . . 84
5.5 Conclusions . . . 86

6 Conclusion **87**

A Optoelectronic Tweezer Fabrication **89**
A.1 a-Si:H Deposition and Characterization . . . 89
A.2 Channel Integration . . . 90

B Embryo Work Materials and Methods **92**
B.1 Ethics Statement . . . 92
B.2 Device Fabrication . . . 92
B.3 OET Apparatus . . . 92
B.4 Embryo Harvest and in vitro Culture . . . 93
B.5 In vitro development in KSOM+AA and M16 . . . 93
B.6 Embryo selection and preparation for OET assay . . . 94
B.7 OET Assay . . . 94

B.8 OET assay of embryos subjected to varying times in EP Media 95
B.9 Embryo survival and development in culture after OET assay 95
B.10 Medium Conductivity 95
B.11 Statistical Analysis 95

C Experimental Setup Parts List **97**

Bibliography **100**

List of Figures

1.1 Generic μTAS Platform 2
1.2 Light-induced Electrokinetics 3

2.1 Force on a Dipole 9
2.2 Dipole Induced Field 9
2.3 Dielectrophoresis 13
2.4 LACE 17
2.5 Electro-thermal 22
2.6 Buoyancy Effects 23
2.7 Figure of Merit 25
2.8 Experimental Setup 27
2.9 Experimental Results 28
2.10 Competition between ET and Buoyancy Effects 29
2.11 OET Operating Regimes 31
2.12 Electrowetting contact angle 32
2.13 Electrowetting force 34

3.1 Overview of Light-induced Dielectrophoresis for Embryo Assessment. 40
3.2 Experimental Results. 43
3.3 Effects of Assay Media. 44
3.4 Viability of *in vitro* Embryos Post-assay. 45
3.5 Effects of Assay Media on OET Speed. 46
3.6 *In vivo* OET-related stress 47

4.1 Lipid Bilayer and Pore Types 53
4.2 Pore Energetics 55
4.3 Effects of Electric Field on Pore Energy 57
4.4 Electric Field Constriction in Hydrophilic Pore 58
4.5 Microelectrode Electroporation with OET Schematic 59
4.6 Microelectrode Electroporation with OET: Positioning 59
4.7 Microelectrode Electroporation with OET: Electroporation 60
4.8 Device schematic 62
4.9 Parallel Single Cell Electroporation 64

4.10 DEP Force Scaling 65
4.11 Cell Viability 68
4.12 Electric Field Response of HeLa Cells. 69
4.13 Automated Cell Transfection with Light-induced Electroporation 70
4.14 Automated Cell Recognition and Optical Pattern Generation 70
4.15 HeLa Cell Transfection 71

5.1 Device Schematic 76
5.2 Frequency Response 78
5.3 Particle Concentration 81
5.4 Serial Concentration 83
5.5 Single Cell Encapsulation 85

A.1 Fabrication 89
A.2 Channel Integration 90

C.1 OET/OEW Experimental Setup 97
C.2 OET/OEW Optical Schematic 98

List of Tables

2.1 OET Regimes of Operation 31

3.1 Conductivity variation 49

C.1 OET/OEW Parts List 99

Acknowledgments

This work would not have been possible if it were not for the support and mentorship of a great many people. Inevitably, I will leave out someone and I apologize in advance for this. First, and foremost, I would like to thank my parents whose unwavering support and love has afforded me the opportunity to experience and pursue all that life has to offer. It is only upon their shoulders that any of this would have been possible. My advisor, Professor Ming C. Wu, has provided the perspective, patience, and resources to make these ideas reality. His quiet, humble nature is preceded only by his love and intellectual command of the sciences. Additionally, I would like to thank Professor Kensall Wise of the University of Michigan for sparking and cultivating my interest in microsystems; his outstanding reputation both as a scholar and a mentor is something I greatly admire. Professor Maurice Garcia of the University of California San Francisco has been instrumental in finding and pursuing the translational aspects of this work. His infectious enthusiasm and razor sharp wit make him someone I am proud to call both a mentor and a friend. Arash Jamshidi, Hsan-Yin Hsu, Aaron Ohta, Steven Neale, Shao Ning Pei, Erwin Lau, the BOTW crew, and the rest of my Berkeley academic colleagues have provided countless resources, advice, stimulating discussion as well as friendship over my tenure here. I will certainly miss not having someone to discuss the physical/political/emotive intricacies of the world at all hours of the day and night. Additionally, I would like to thank Professor Amy E. Herr and Michel M. Maharbiz for serving on my dissertation committee and providing constructive feedback throughout the process. I would also like to thank the entity that is the University of California Berkeley which has exposed me to so many different ideas, cultures, opportunities, and resources (not to mention free lunches!) that I hope every student one day may experience. On a less academic note, I would like to acknowledge all the mountains, crags, nuts, cams, ropes, axes, helmets, and belayers that have provided a wonderful escape from the demands of all aspects of life. Through these adventures, I have gained a valuable perspective on life and a great appreciation for the outdoors (as well as a healthy respect for gravity!). Finally, I would like to thank the person in my life whose love, support, and selflessness have propelled me to pursue my dreams while keeping my feet (and personality) firmly grounded. I love you Liz.

Chapter 1

Introduction

Truth gains more even by the errors of one who, with due study, and preparation, thinks for himself, than by the true opinions of those who only hold them because they do not suffer themselves to think.

- John Stuart Mill, *On Liberty*, 1859.

In the mid-nineteenth century, engineers faced an increasingly difficult problem which many referred to as the 'tyranny of numbers'. This 'tyranny' related to the large number of discrete components that had to be assembled, and subsequently connected, in order to realize even basic computer hardware. It was not until 1958 when Jack Kilby, at Texas Instruments, was left alone in the lab (the others were all on summer vacation) to 'come up with a good idea very quickly' regarding the integration of multiple electronic components on chip [1]. The result was the concept of the integrated circuit, which combined with Robert Noyce's ideas, formed an elegant solution to the tyranny of numbers. This concept enabled the monolithic integration of transistors, resistors, capacitors, and interconnects on the same chip. And perhaps, more importantly, it enabled a cost scaling model which has provided the semiconductor industry with a well defined roadmap for producing ever cheaper products with ever increasing performance. As a result, it is responsible today for the permeation of high-performance electronics in nearly every facet of our lives.

As with many great ideas, this idea of monolithic integration, as a segway to higher performance and lower cost, has been applied in a variety of different contexts aside from the semiconductor industry. One of these, and the most pertinent to this discussion, is the idea of the lab on a chip, or micro-total analysis system (μTAS). This concept pertains to the shrinking of one, or several, laboratory functions to a single chip. The main motivation for this is, once again, cost and performance. On a cost basis, smaller laboratory experiments/analyses require smaller analyte consumption. These analytes are often very cost-prohibitive (e.g. antibodies) and/or scarce in nature (e.g. forensic DNA). Additionally, the creation of these systems can piggy-back on the fabrication capabilities of the semiconductor industry enabling minimal (per die) fabrication costs and high yield. From a performance perspective, the simple fact that the reactions/functions of interest are occurring on a small scale enables faster (e.g. due to shorter diffusion lengths) and more sensitive (e.g. due to higher surface

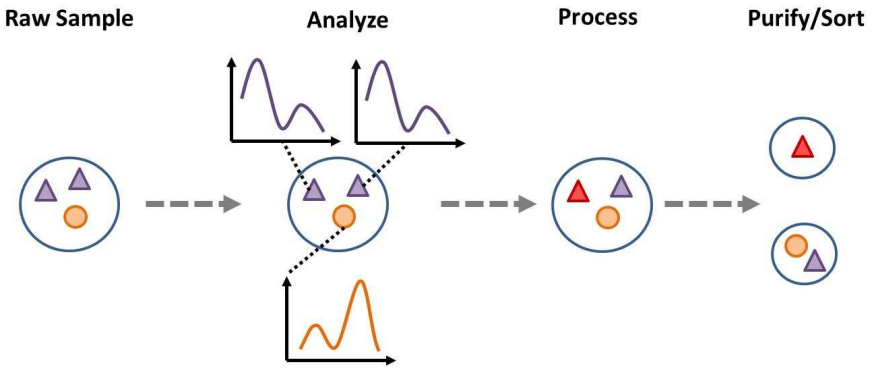

Figure 1.1: Functions of a generalized μTAS system in which a raw heterogenous sample is analyzed through measurement of some intrinsic property (e.g. impedance, mobility), then processed (e.g. tagged) based on said property, and finally purified and/or sorted from its native environment.

area to volume ratios) analysis. Additionally, since many functions can be implemented in a small footprint, massively parallel functions are enabled increasing throughput dramatically. The applications for these devices vary widely, but include point-of-care diagnostics, pharmaceutical development, and environmental monitoring.

While the idea of μTAS has been around since 1990 [2], the wide scale commercial adoption and commercialization of the field has yet to be realized. In part this is due to both the lack of a 'killer application' and a standardized toolset (i.e. functional elements) upon which to build complex systems. While largely academic in nature, elegant work has been realized that demonstrates the large scale integration of basic elements (e.g. valves) to create fluidic-based comparators, multiplexors, etc [3]. However, in most cases, this has led to a series of 'one-off' devices which are tailored to a very specific need, and not easily transferable to other applications/situations.

Ideally, we would be able to create a generic platform which can be utilized in a variety of different scenarios. Each system should be able to perform one or more specific functions as depicted, in very general terms, in Fig. 1.1. These functions include the ability to take a raw sample (e.g. blood, DNA, etc.) and perform some sort of analysis (e.g. measure, impedance, mobility, etc.) on it. Based on this analysis that sample is then processed (e.g. chemically tagged, genetically modified, etc.) and, finally, purified or sorted into its constituents. These functions can be applied in any order and in combined in various feedback loops *ad nauseam* in order to realize a vast array of applications. Of course, one would also like the platform to be reconfigurable, intrinsically parallel in nature, while still affording high resolution (e.g. single cell/particle). In this manner, the user can custom build their application into the chip by placing and rearranging where these functions are performed (In the context of the technology presented here, the various applications are chosen simply by changing the electrical bias and optical patterns projected onto the device.).

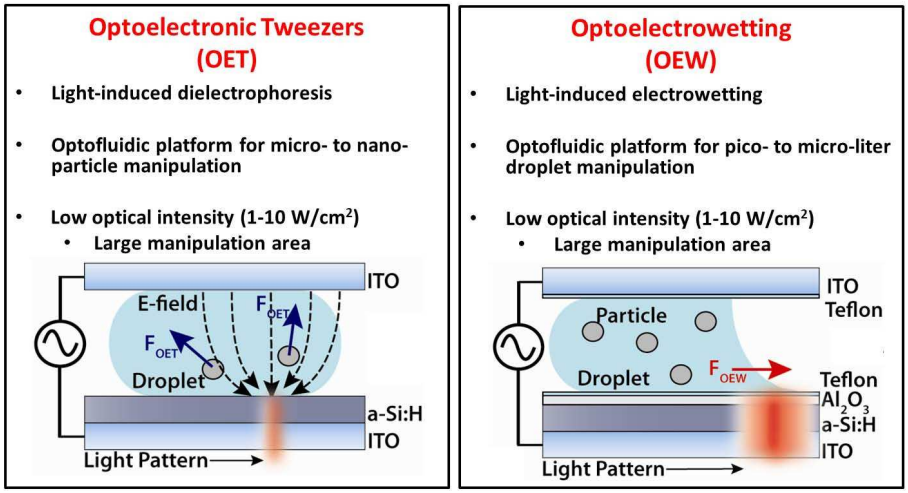

Figure 1.2: The two main modalities of light-induced electrokinetics. Optoelectronic tweezers (OET) uses low-intensity light to induce dielectrophoretic forces on particles within solution. Whereas, optoelectrowetting (OEW) uses low-intensity light to induce an electrowetting force on a droplet, enabling droplet translation. In OET (OEW) parallel single particle (droplet) control and movement is realized.

A technology platform which fits well within the above definition of a generalized μTAS is that of light-induced electrokinetics. Light-induced electrokinetics refers to the use of light, interacting with a photosensitive substrate and externally applied electrical bias, to exert forces on either particles or fluids. These forces can be controlled such that individual particle or droplet manipulation can occur. While a variety of physical forces can be manifested (all of which will be described in the Ch. 2), the two of most interest are dielectrophoresis and electrowetting. Specific names are attributed to a light-induced electrokinetic device operating in either modality. Optoelectronic tweezers refers to a device where dielectrophoresis is the main force being produced and is used for particle manipulation. Optoelectrowetting refers to a device where electrowetting is the primary mechanism and is used to droplet manipulation. The physical manifestation of these forces will be described in Ch. 2. Fig. 1.2, summarizes the relationship between the two primary modalities of light-induced electrokinetics. Both use low intensity light that is patterned on a photosensitive substrate to alter the local electric field profile in the device. This alteration of the electric field drives either dielectrophoretic (OET) or electrowetting (OEW) forces on particles or droplets, respectively. In both cases, parallel single particle/droplet control is afforded simply by altering the projected optical pattern.

Due to the use of light to define where these forces are exerted in space, light-induced electrokinetics is a reconfigurable, parallel, and high resolution platform. Now the question is **can we use light-induced electrokinetics, namely OET and OEW, to perform each of the generic requirements of the μTAS platform** depicted in Fig. 1.1? This

will be the subject, and main goal, of the following pages.

First, we will start with a closer look at light-induced electrokinetics and describe all of the forces present during operation of either the OET or OEW device. With this background, we can then proceed to use this platform to address specific applications which address the requirements of the μTAS platform: analysis, process, and purify/sort. In Ch. 3, we will quantitatively analyze the developmental potential of pre-implantation stage embryos in the context of *in vitro* fertilization. Next, in Ch. 4, we will use the ability to control the location and strength of the electric field to electroporate (i.e. process) individual cells in parallel for genetic engineering applications. Finally, in Ch. 5, we will show that the OEW device can operate in either an electrowetting (OEW) or dielectrophoretic (OET) modality through a simple change in device bias. This enables both particle and droplet manipulation on the same chip. We will use this concept to achieve sample concentration (i.e. purification) and single cell encapsulation (i.e. sorting). At the conclusion of this discussion, we hope to show that light-induced electrokinetics provides a truly generic μTAS platform that is capable of a variety of different applications and may lead to a foundation for future academic, as well as commercial, enterprise.

Chapter 2

Light-induced Electrokinetics

This is a very complicated case...You know, a lotta ins, a lotta outs, a lotta what-have-yous.
- The Dude, *The Big Lebowski*, 1998.

2.1 Motivation

Light-induced electrokinetics involves the use of light to induce forces on particles, continuous liquids, and discrete volumes of liquids (e.g. droplets). In this chapter, we will review current techniques for optical particle and droplet manipulation and then provide some insight into the physical mechanisms present in the light-induced electrokinetic platform.

2.1.1 Optical particle manipulation

Much of the difficulty in the individual manipulation of micro- and nano-scopic objects stems from the fact that macroscale objects are used to interface with objects many orders of magnitude ($10^3 - 10^6$) smaller in scale. As a result, much work has been performed to reduce the size disparity between the manipulation tool and object of interest. These techniques include, amongst others, the use of ultra-small probes (e.g. atomic force microscopy tips [4]), fixed electrode-based dielectrophoresis [5, 6], and various microfluidic/flow-based techniques [7]. These techniques do not, however, afford the highly selective and dynamic capabilities of optical manipulation platforms. In general, optical manipulation platforms afford the user the ability to create on-demand particle traps in regions only defined by the optical pattern. Therefore, simply by translating the optical pattern, the particle of interest will follow. These virtual electrodes replace the need for physical ones, (as in [5, 6]) and, thus, greatly simplify fabrication and operation, as well as, lower device cost as complicated address circuitry is no longer necessary. In a sense, these techniques replace cumbersome, material-based micro- and nano-scale "tweezers" with photonic ones.

The most conventional method of optical manipulation is optical tweezers [8, 9]. Here, a highly focused laser beam creates a large gradient in an optical field, resulting in stable

particle trapping at the beam focus. Since the trapping occurs only at the focal point, true three-dimensional trapping can occur. Particles in scale from cells (μms) to individual molecules (nms) are routinely studied with this technique [10, 11]. However, due to the large amounts of optical power necessary to create traps of adequate stiffness, large optical intensities are necessary ($10^6 W/cm^2$ [12]). This makes it difficult to create and control multiple traps on the same device since multiple high-powered lasers and/or holography techniques must be employed [13]. Additionally, the high optical powers can be harmful to sensitive objects such as biological cells [14, 15].

Another form of optical manipulation that has been recently employed is that of plasmonic tweezers [16,17]. Here, a substrate that consists of an array of nanoscopic objects (e.g. nanoparticles or lithographically defined nano-scale pillars) is illuminated with a laser beam. The small particles on the surface absorb the incident radiation into resonant plasmonic modes. Due to the tight spacing of the nanoparticles on the surface, the plasmonic modes of the particles are coupled to one another, resulting in very large and localized electric fields. The localization of these fields establishes large electric field gradients, which cause particles in the general area to polarize and experience a dielectrophoretic force. Thus, wherever the laser illuminates the device, the electric field gradients are produced and particle traps are created. While this technique uses lower optical intensity than optical tweezers ($10^4 W/cm^2$ [17]), the required intensity is still significant, requiring high-power lasers and making parallelization difficult. Additionally, the conversion of plasmonic energy into heat is also an area of concern with this device, especially for biological applications. This plasmonic heating effect is exploited in other applications, such as the intracellular delivery of RNA interference plasmids [14]. Lastly, due to the highly textured plasmonic substrate, observation of particle movement using dark-field microscopy is difficult.

The final method of optical manipulation, optoelectronic tweezers (OET), removes the restriction of high optical intensities imposed by the other techniques [18]. By using a photosensitive substrate and an externally applied electrical bias, incident light creates localized regions of high conductivity (in the photosensitive substrate) resulting in the creation of large electric field gradients. Therefore, particles in the illuminated region will experience a dielectrophoretic force. Due to the conversion of optical field to electrical field, very low ($< 1 W/cm^2$) optical powers are necessary to apply the same level of forces as optical tweezers (tens to 100s of pN) to the particles of interest. This means that a standard data projector, or spatial light modulator (SLM), can be used for manipulation. Thousands of simultaneous traps can be created on demand for the massively parallel manipulation of single particles. Another benefit of low optical intensity is that sensitive objects, such as cells, are not adversely affected by the incident light energy making OET an ideal platform for biological applications [19]. Additionally, it should be noted that the conductivity of the liquid layer plays an important role in device operation. The conductivity of the liquid must fall between the light and dark conductivity of the photosensitive layer. For example, if the liquid conductivity is too high, an insufficiently small field will be switched to the liquid when illuminated and DEP actuation cannot occur. For the devices presented here, this typically limits the liquid conductivity to $< 100 mS/m$. For applications requiring operation

in a highly conductive environment (e.g. cell culture media), we have developed a different structure utilizing phototransistors instead of photoconductors to effectively switch the field to the highly conductive liquid [20].

Until now there has not been a comprehensive study of the various physical effects present in the operation of the OET device. Light-induced DEP is but one of these forces and lends itself to only a specific set of bias and device parameters. In addition to DEP, localized light-induced heat gradients and electrical double layers in the fluid can interact with the electric fields present resulting in predictable fluid flow and particle movement. It has already been reported that light-induced AC electro-osmosis (LACE) is the dominant effect at low bias frequencies [21]. It is imperative to understand the underlying physics of these effects so that accurate predictions can be made as to what effect is dominant given a set of bias conditions.

2.1.2 Droplet manipulation

The ability to quickly perform large numbers of chemical reactions in parallel using low reagent volumes is a field well addressed by digital microfluidics. Compared to continuous flow-based techniques, digital microfluidics offers the advantage of individual sample addressing, reagent isolation, and compatibility with array-based techniques used in chemistry and biology [22, 23]. Several biological and non-biological applications, such as DNA amplification with polymerase chain reaction [24], purification of peptides and proteins from heterogeneous mixtures [25], and chemical synthesis [26], have been demonstrated using digital microfluidics.

Digital microfluidics is generally realized by sandwiching a liquid droplet between two layers of electrodes. One layer has a grounding electrode over its entire surface while the other contains an array of lithographically defined, individually addressable electrodes. The spacing of these electrodes is such that the droplet covers more than one electrode at a time so that a voltage may be applied to only part of the droplet [22, 23]. The droplet is moved towards the region of high electric potential through a combination of electromechanical forces. A caveat to this technique, however, is that when multiple droplets need to be manipulated simultaneously, a large and complex electrode network must be created. Additionally, since the electrode size determines the minimum droplet volume that can be actuated, as electrodes scale to smaller sizes, interconnect and addressing of these electrodes grows proportionally. Consequently, large scale droplet manipulation requires complex addressing schemes and multi-layer metal deposition [27].

In 2003, we reported a device which removed the need for individual electrode addressing imposed by current techniques. Instead of lithographically defined interconnects, photosensitive interconnects were used to selectively address electrodes [28]. While this device removed the constraint of complex addressing schemes, the size of the manipulated droplet was still governed by the size of the patterned electrodes. We subsequently reported a device which utilized a continuous photosensitive film which replaced both the electrodes and interconnects to achieve droplet manipulation [29]. Since the electrode size is now defined by the size of the optical pattern, instead of the physical size of the electrode, one can ma-

nipulate picoliter to microliter scale droplets on the same device without the need to change the electrode spacing.

In the following chapter, we first describe the variety of effects present in the OET device. We develop the basic theory behind each effect and then present FEM modeling of the phenomena as it manifests itself in the OET device. Next, we develop a figure of merit to quantify the relative contributions of each of these effects and predict which effect will be dominant for some parameter set and we compare experimental results to the developed theory to confirm its validity. Finally, we will discuss a variant of the OET device (Optoelectrowetting (OEW)) which enables droplet manipulation through a light-induced electrowetting phenomena. This background chapter will serve as the theoretical backbone for understanding the various physics and capabilities of the light-induced electrokinetic platform and will provide a segway to applications of the technology in subsequent chapters.

2.2 Physical forces present in the OET Device

2.2.1 Light-Induced Dielectrophoresis

Dielectrophoresis Theory

The presence of an electric field will induce a dipole moment in a particle. If the field is non-uniform this induced dipole will feel a net force. This force is known as Dielectrophoresis (DEP). To quantify this force we first consider the effect of an infinitesimal dipole in an externally imposed electric field as in Fig. 2.1. The force will be the sum of the forces acting on the constituent charges of the dipole:

$$\boldsymbol{F}_{dipole} = q\boldsymbol{E}(\boldsymbol{r}+\boldsymbol{d}) - q\boldsymbol{E}(\boldsymbol{r}) \tag{2.1}$$

where q is the unit electron charge, $\boldsymbol{d}$ is the dipole vector, and $\boldsymbol{E}(\boldsymbol{r})$ is the electric field. If we assume that $d \ll r$, we can expand the first term on the right hand side of Eq. 2.1:

$$\boldsymbol{E}(\boldsymbol{r}+\boldsymbol{d}) = \boldsymbol{E}(\boldsymbol{r}) + \boldsymbol{d}\cdot\nabla\boldsymbol{E}(\boldsymbol{r}) + \dots \tag{2.2}$$

Plugging Eq. 2.2 into Eq. 2.1, and taking the limit that $\boldsymbol{d}$ is infinitesimally small, we receive a net force acting on the dipole of:

$$\boldsymbol{F}_{dipole} = q\boldsymbol{d}\cdot\nabla\boldsymbol{E}(\boldsymbol{r}) = \boldsymbol{\mu}\cdot\nabla\boldsymbol{E} \tag{2.3}$$

where $\boldsymbol{\mu}$ is defined as the dipole moment. We can see that the dipole will only experience a force in the presence of a non-uniform electric field.

In DEP, the electric field induces an effective dipole moment (and higher order multipole moments) in the particle which we shall call $\boldsymbol{\mu}_{eff}$. If we neglect the higher order multipoles, we can generalize Eq. 2.3 to obtain an equation for the DEP force:

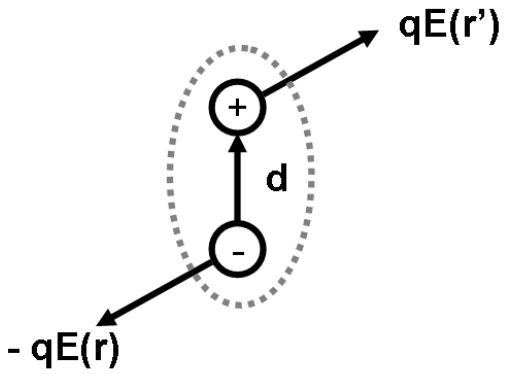

Figure 2.1: Forces acting on a dipole with charge $\pm q$, in an external, non-uniform electric field $\boldsymbol{E}$.

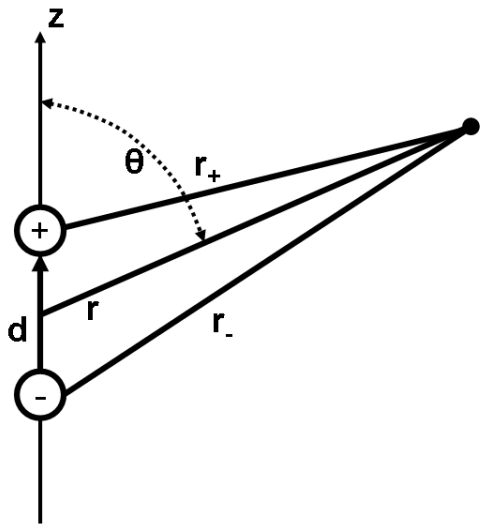

Figure 2.2: Definition of geometric parameters for calculation of induced electric field due to a dipole.

$$\boldsymbol{F}_{dipole} = \boldsymbol{\mu}_{eff} \cdot \nabla \boldsymbol{E} \tag{2.4}$$

Now, our problem has been reduced to finding an expression for the effective induced dipole moment of a particle in an electric field. But, first, since DEP induces a dipole moment in a particle, let us find the induced field due to a dipole and then generalize to a particle. The following takes the approach of *Jones* [30].

Consider Fig. 2.2, where a dipole (with two point charges of charge q separated by a distance d) is oriented along the z-axis in a medium of permittivity ϵ_m. We want to find the potential at a point defined by r and θ. Using superposition, we can find the potential at this point to be:

$$V(r,\theta) = \frac{q}{4\pi\epsilon_m r_+} - \frac{q}{4\pi\epsilon_m r_-} \tag{2.5}$$

where r_+ and r_- are defined in Fig. 2.2. We want to find a relation between d and $r_\pm$ to write V in a more familiar form. Using geometry one can show that:

$$\frac{r}{r_\pm} = \left[1 + \left(\frac{d}{2r}\right)^2 \mp \frac{d}{r}\cos\theta\right]^{-1/2} \tag{2.6}$$

By expanding the left hand side of Eq. 2.6 in a Maclaurin series one can transform Eq. 2.6 into:

$$\frac{r}{r_\pm} = P_0 \pm \left(\frac{d}{2r}\right) P_1 + \left(\frac{d}{2r}\right)^2 P_2 \pm \left(\frac{d}{2r}\right)^3 P_3 + \ldots \tag{2.7}$$

where $P_n(\cos\theta)$ is the n^{th} Legendre polynomial. Using Eq. 2.7 with Eq. 2.12 and a moderate amount of algebra, one can obtain a new expression for V:

$$V(r,\theta) = \frac{qdP_1(\cos\theta)}{4\pi\epsilon_m r^2} + \frac{qd^3P_3(\cos\theta)}{16\pi\epsilon_m r^4} + \ldots \tag{2.8}$$

Notice that the first term in the above equation is proportional to the dipole moment μ defined previously. The first term in the above series is the induced dipole moment, while the subsequent terms are the higher order multipole terms. Thus, generalizing to an arbitrary dipole moment we find that the electric potential due to the induced dipole is:

$$V_{dipole} = \frac{\mu_{eff}P_1(\cos\theta)}{4\pi\epsilon_m r^2} \tag{2.9}$$

Now, let us return to the problem of determining $\boldsymbol{\mu}_{eff}$. For the sake of simplicity, we will derive $\boldsymbol{\mu}_{eff}$ for the simplest case of a dielectric particle in a dielectric medium. This can then be generalized for particles and solutions which are lossy.

Consider a spherical dielectric particle with radius a and permittivity ϵ_p suspended in a medium with permittivity ϵ_m. Let there be a uniform electric field, $\boldsymbol{E}_0$, with a source at infinity and no free charge in the system. Using these facts combined with Laplace's equation, we can solve for the electric potential outside (V_1) and inside (V_2) of the particle. In spherical coordinates, the solution is:

$$V_1 = -E_0 r\cos\theta + \frac{A\cos\theta}{r^2}, r > a \tag{2.10}$$

$$V_2 = -Br\cos\theta, r < a \tag{2.11}$$

where E_0 is the electric field and A, B are constants. Note, that the second term in Eq. 2.10 is the induced dipole field from the particle. To determine A and B we must apply the necessary boundary conditions which state that:

1: The potential V must be continuous across the solid-liquid boundary.

2: The component of the displacement flux density normal to the surface of the particle must also be continuous.

Applying the above conditions, the resultant expressions for A and B are:

$$A = \frac{\epsilon_p - \epsilon_m}{\epsilon_p + 2\epsilon_m} a^3 E_0 \tag{2.12}$$

$$B = \frac{3\epsilon_m}{\epsilon_p + 2\epsilon_m} E_0 \tag{2.13}$$

Next, let us compare the induced dipole component of Eq. 2.10 and that of Eq. 2.9. Using the above two equations, we deduce that:

$$\boldsymbol{\mu}_{eff} = 4\pi\epsilon_m a^3 \boldsymbol{E}_0 \frac{\epsilon_p - \epsilon_m}{\epsilon_p + 2\epsilon_m} = 4\pi\epsilon_m K a^3 \boldsymbol{E}_0 \tag{2.14}$$

where K is called the Claussius-Mossotti (CM) factor and accounts for the polarization of the particle in a given medium. It can range from -0.5 to 1. Thus, combining this with Eq. 2.4, we find the DEP force acting on a lossless spherical, dielectric particle in a dielectric medium:

$$\boldsymbol{F}_{dep} = \boldsymbol{\mu}_{eff} \cdot \nabla \boldsymbol{E}_0 = 2\pi a^3 \epsilon_m K \nabla (\boldsymbol{E}_0)^2 \tag{2.15}$$

where we have used the vector identity $\boldsymbol{E}_0 \cdot \nabla \boldsymbol{E}_0 = 1/2\nabla(\boldsymbol{E}_0)^2$. This is the DEP equation for the case of a lossless, dielectric particle and medium under a DC electric field. If we generalize to the case of a lossy medium and an AC electric field, we find that the time averaged force felt by the spherical particle has the same form as Eq. 2.15 [30]:

$$\langle \boldsymbol{F}_{dep} \rangle = 2\pi a^3 \epsilon_m Re[K^*] \nabla (\boldsymbol{E}_{rms})^2 \tag{2.16}$$

where $\boldsymbol{E}_{rms}$ is the rms electric field and K^* is the complex conjugate of the Clausius-Mossotti (CM) factor for a lossy particle and medium, defined as:

$$K^* = \frac{\epsilon_p^* - \epsilon_m^*}{\epsilon_p^* + 2\epsilon_m^*} \tag{2.17}$$

where ϵ_p^* and ϵ_m^* are equal to the complex conjugate of the complex permittivity of the particle and medium respectively which is equal to $\epsilon - j\sigma/\omega$ where ϵ, σ, ω are the electrical permittivity, conductivity, and frequency.

DEP in OET

The OET device structure and setup are depicted in Fig. 2.3a. The device consists of a photoconductive layer of hydrogenated amorphous silicon (a-Si:H) on an indium tin oxide (ITO) coated glass substrate. Liquid containing the particles of interest is sandwiched between this lower device and a top piece of ITO coated glass. An AC bias is applied between the two ITO layers. In the absence of light, the majority of the voltage drops across the a-Si:H layer. However, upon illumination, the a-Si:H layer's conductivity increases by many orders of magnitude (Fig. 2.3c) due to the creation of electron-hole pairs.

The conductivity measurement was obtained by patterning a-Si:H electrodes on an ITO coated glass substrate. Aluminum electrodes were then patterned on top of the a-Si:H. A 10 mW, 632 nm diode laser is sent through a continuous attenuator to a beam splitter which splits the beam between a photo detector and a 10x objective that focuses the laser light onto a lithographically patterned 50 μm x 50 μm a-Si:H square. A series of voltage sweeps are performed across the a-Si:H electrode for varying laser powers. The current is measured for each of these sweeps and the conductivity is extracted.

The result of the conductivity increase upon illumination causes the voltage to now drop across the liquid layer in the vicinity of the illuminated region causing a localized electric field gradient to occur. All subsequent simulations are carried out in a commercially available FEM package (COMSOL Multiphysics 3.2a).

In the presence of light, a localized electric field gradient is created in the illuminated region as shown in Fig. 2.3b. The time averaged force felt by a spherical particle due to this gradient is defined by Eq. 2.16. Depending on the value of the CM factor, the DEP force can either be repulsive or attractive. For the case of polystyrene beads in slightly conducting medium (1 mS/m), the CM factor is less than zero (-0.5) resulting in repulsion from the electric field intensity maxima and attraction to electric field intensity minima. Thus, the particle is repelled from the illuminated region [30].

Using Stokes' formula; we can calculate the velocity under the influence of the DEP force for a spherical particle according to:

$$\boldsymbol{U}_{dep} = \frac{\boldsymbol{F}_{dep}}{6\pi\eta a}\nabla(\boldsymbol{E}_0)^2 \tag{2.18}$$

where $\boldsymbol{U}_{dep}$ is the DEP-induced particle velocity and η is the viscosity of the fluid. The direction of the velocity vector is parallel to the induced electric field gradient. Fig. 2.3d shows the maximum DEP velocity for a 10 μm diameter polystyrene bead at one particle radius away from the surface of the a-Si:H for a 1 mW laser focused to a 20 μm spot size at 10 Vpp and 100 kHz. Note the dotted portion of Fig. 2.3d at the beam center. Points in this region are not valid simulated velocities. This is because the vertical, negative DEP force component will cause the particle to rise off of the OET substrate near the beam center. This occurs when the vertical DEP component and buoyancy forces balance one another. Our simulations and experiments suggest that this occurs at around 18 μm from the beam center for the bias conditions of Fig. 2.3d. It is important to note that the horizontal DEP

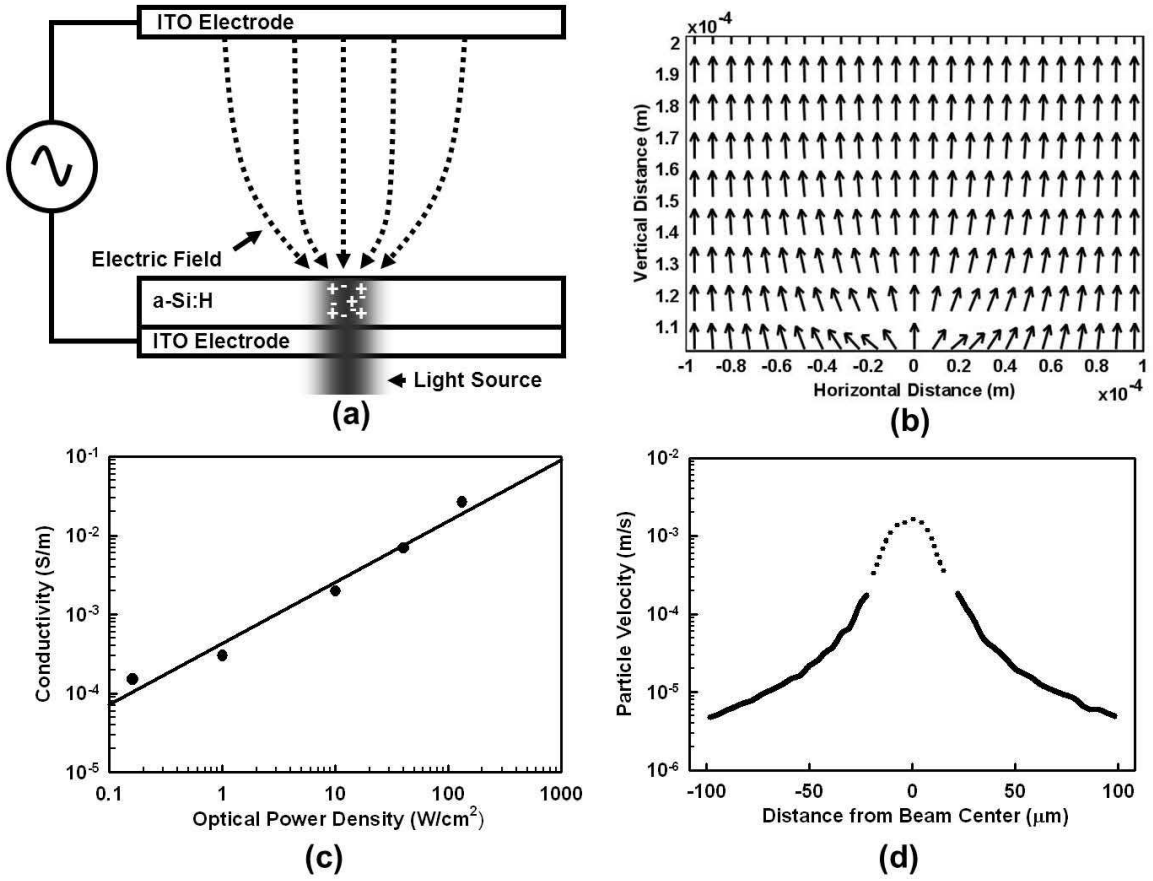

Figure 2.3: (a) OET structure. Electron-hole pairs generated in the illuminated region increase the conductivity of the a-Si:H, resulting in the majority of the applied voltage dropping across the liquid layer. The light pattern is centered at position zero. (b) Simulated electric field distribution. (c) Experimental a-Si:H conductivity versus optical power density. (d) Simulated 10 μm particle velocity versus distance for an optical power of 1 mW and an illumination spot size of 20 μm at 5 μm above the a-Si:H surface. The dotted region corresponds to points within 18 μm of the beam center which are not valid due to the effects of vertical DEP forces acting on the particle. The bias conditions are 10 Vpp and 100 kHz. The velocity of the particle is parallel to the gradient of the electric field. The light pattern is centered at position zero.

force drops dramatically as one moves away from the substrate-liquid interface. Once the particle leaves the surface, the particle often slips over the light pattern and results in loss of particle control. Therefore, the DEP-induced velocity is only meaningful for distances from the beam center at which the particle still remains on the OET surface.

For this calculation, a Gaussian distribution in conductivity was used to simulate the effect of the illumination spot. The electric field gradient profile, with this conductivity distribution, was then extracted via FEM, and the DEP force and particle velocity calculated. These simulations also assume that the relative permittivity of the medium and particle are 78 and 2.56 respectively. These values remain constant throughout the remainder of the paper. Additionally, all formulas assume a 10 μm particle diameter and a 1 mS/m liquid conductivity, unless otherwise stated.

The simulated velocities of Fig. 2.3d agree with our experimental observations. By scanning a laser line across the OET surface and determining the fastest scan rate at which the particle is still trapped by DEP, one can determine the maximum DEP-induced velocity. For the bias and device conditions of Fig. 2.3d, we find a maximum particle velocity of 105 $\mu m/s$. This agrees with the maximum valid simulated velocities in Fig. 2.3d.

2.2.2 A Brief Note on DEP and Optical Tweezers in the Rayleigh Limit

As mentioned above, the other major optical manipulation platform is that of optical tweezers (OT). This technique uses highly focused coherent radiation to trap individual particles. Typically in the literature, the forces associated with OT are described in one of two limits: the Rayleigh and Mie limit.

The Mie limit describes the scenario when the wavelength of the trapping beam is much smaller than the particle of interest. In this case, ray optics are used to describe the transfer of photon momentum to the particle when the trapping beam refracts at the particle-ambient interface. If the beam is focused tightly enough, this momentum transfer results in the particle being trapped at the focal point (actually the particle is slightly offset from the exact focal point due to the additional axial scattering force (acting in the direction of beam propagation)).

In the Rayleigh limit, the wavelength of the trapping beam is much larger than that of the particle. In this case, the Rayleigh scattering limits are satisfied and the particle can be treated as a point dipole in an inhomogeneous field (due to the focusing of the trapping beam). This is identical to the situation described in 2.2.1. Thus, the resulting optical trapping force in the Rayleigh limit should be identical in form to the DEP equation already derived above.

In order to further elucidate this, lets consider the simplified case of a lossless, dielectric particle. In the Rayleigh limit, the optical trapping force of a dielectric particle is typically called the optical gradient force and has the form (in SI units) [31]:

$$\boldsymbol{F}_{grad} = 2\pi n_m^2 r^3 \frac{n_p^2 - n_m^2}{n_p^2 + 2n_m^2} \nabla(\boldsymbol{E})^2 \tag{2.19}$$

where r is the particle's radius, $\boldsymbol{E}$ is the electric field, and n_m and n_p are the medium and particle's indices of refraction, respectively. Already this looks nearly identical to the standard DEP force equation. Remembering that the refractive index, for a lossless particle, is defined such that $n^2 = \epsilon$, where ϵ is the electrical permittivity of the sample (which, in general, is frequency dependent), Eq. 2.19 turns into:

$$\boldsymbol{F}_{grad} = 2\pi \epsilon r^3 \frac{\epsilon_p - \epsilon_m}{\epsilon_p + 2\epsilon_m} \nabla(\boldsymbol{E})^2 \tag{2.20}$$

Which is identical to that derived for lossless, dielectric particle undergoing DEP.

So, the physics of optical tweezers, in the Rayleigh limit, is identical to dielectrophoresis. The only differences being the electric field gradient, in the optical tweezing case, is provided by the trapping beam itself and the material properties utilized in the equation must be associated with the frequency of the light wave.

2.2.3 Light-induced AC Electro-osmosis (LACE)

Theory of Electro-osmosis

The application of an electrical potential on an ionic fluid results in the formation of an electrical double layer. If a tangential electric field component is present in the double layer region, ions in the layer will move in response to this field. The velocity of these ions is called the slip velocity. We can deduce an equation for the velocity of a liquid layer of thickness dx of these ions by equating the electrical and viscous forces per unit area acting on the ions [32]:

$$\rho_q \boldsymbol{E}_t dx = \left(\eta \frac{d\boldsymbol{v}}{dx}\right)_{x+dx} - \left(\eta \frac{d\boldsymbol{v}}{dx}\right)_x = \frac{d}{dx}\left(\eta \frac{d\boldsymbol{v}}{dx}\right) dx \tag{2.21}$$

where ρ_q is the charge density, $\boldsymbol{E}_t$ is the tangential electric field, η is the fluid viscosity, and $\boldsymbol{v}$ is the fluid velocity. Next, we can insert the Poisson equation for the charge density to obtain:

$$-\boldsymbol{E}_t \frac{d}{dx}\left(\epsilon_m \frac{d\phi}{dx}\right) = \frac{d}{dx}\left(\eta \frac{d\boldsymbol{v}}{dx}\right) dx \tag{2.22}$$

where ϵ_m is the permittivity of the liquid. Next, after one round of integration we obtain:

$$-\boldsymbol{E}_t \left(\epsilon_m \frac{d\phi}{dx}\right) = \left(\eta \frac{d\boldsymbol{v}}{dx}\right) + constant \tag{2.23}$$

The constant must be zero since we choose at $x = \infty$, $\frac{d\phi}{dx} = \frac{d\boldsymbol{v}}{dx} = 0$. Noting this and integrating once again:

$$-\boldsymbol{E}_t \epsilon_m \phi = \eta \boldsymbol{v} + constant \tag{2.24}$$

Again, the constant will be zero assuming that at $x = \infty$, $\phi = \boldsymbol{v} = 0$. Also, let us define at $x = 0$, $\phi = \zeta$ and $\boldsymbol{v} = \boldsymbol{v}_{slip}$. Rearranging, we obtain:

$$\boldsymbol{v}_{slip} = -\frac{\epsilon \zeta \boldsymbol{E}_t}{\eta} \tag{2.25}$$

where ζ is known as the zeta potential (defined as the voltage drop across the electrical double layer) and $\boldsymbol{v}_{SLIP}$ is the slip velocity of the liquid at the liquid/solid interface. Eq. 2.25 is known as the Helmholtz-Smoluchowski equation [33]. This fluid velocity is present at the edge of the electrical double layer and results in an overall fluidic flow.

Light-induced AC Electro-osmosis in OET

Traditional electro-osmosis uses a DC bias and is often employed in the use of microfluidic pumps [34]. AC electro-osmosis has been observed more recently [35]. Here, the ionic charge at the surface of the double layer switches polarity in response to the applied AC field and results in a steady state motion of the ions in one direction. Lastly, Light Induced AC Electro-osmosis, or LACE, has been reported using the OET device for nanoparticle trapping [21]. In this scheme, a virtual electrode created by patterned light replaces the need for traditional metal electrodes.

AC Electro-osmosis and LACE both exhibit frequency dependence. This dependence arises out of the fact that the electrical double layer acts as a capacitor and, therefore, has an intrinsic roll-off frequency. Above this critical frequency, the double layer can no longer sustain a voltage drop across itself and the zeta potential, along with the slip velocity, approach zero.

In the OET device, the creation of a virtual electrode upon localized illumination results in a tangential electric field which produces a slip velocity. In order to model this effect, an equivalent circuit model, depicted in Fig. 2.4a, is used to extract the zeta potential. In this model, the electrical double layer is treated as a simple parallel plate capacitor in series with resistors accounting for the liquid and a-Si:H layers. The double layer capacitance varies with the layer's thickness, which is a function of liquid conductivity. In accordance with Gouy-Chapman theory, we can derive an expression for the double layer thickness as a function of liquid conductivity.

Gouy-Chapman theory assumes that the double layer charge follows a Boltzmann distribution and that the surrounding medium only affects the double layer by means of its permittivity. It is assumed that the permittivity is the same in the double layer as outside of it. Lastly, the solvent species will be of one type and have a charge number z [32].

Given the above assumptions, let us first define the electric potential ϕ at a distance x above the surface. The positive (n_+) and negative (n_-) ionic charge densities are give by the Boltzmann distributions:

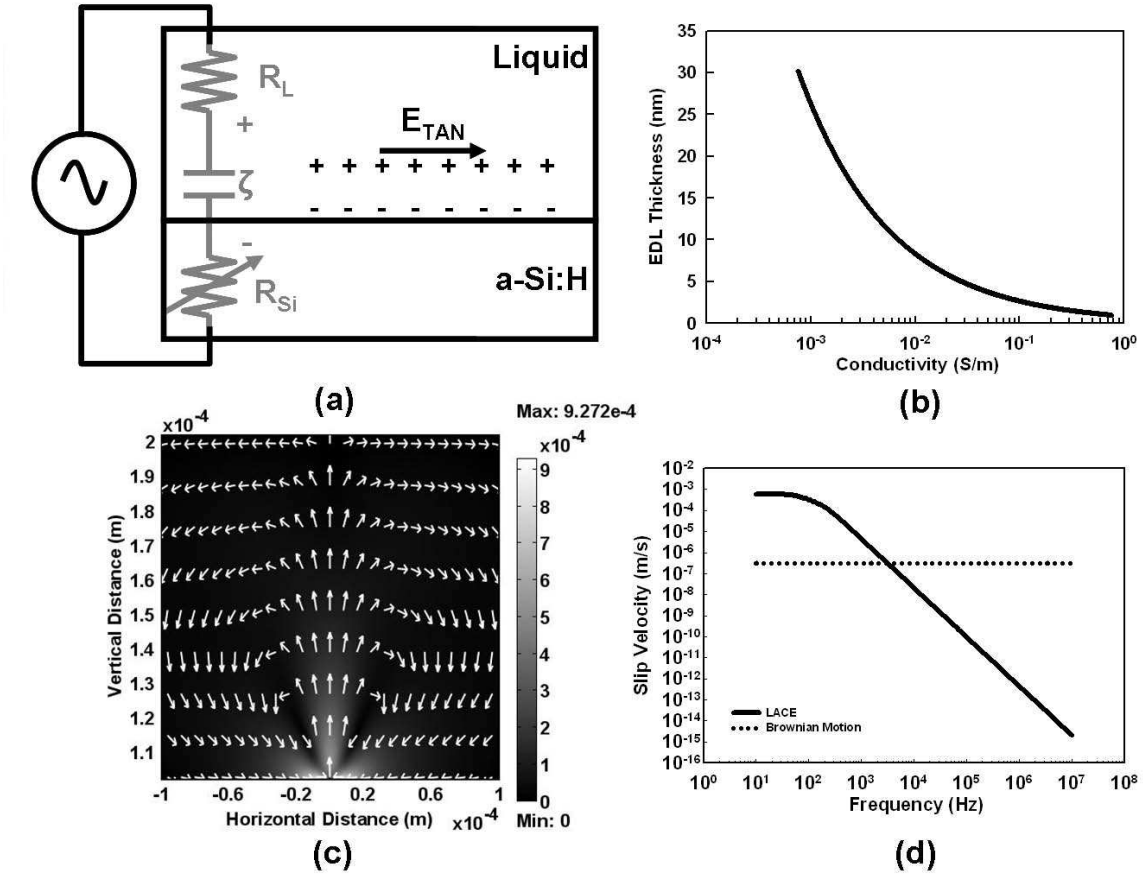

Figure 2.4: (a) Equivalent circuit schematic of LACE. Ions in the electrical double layer respond to the tangential electric field resulting in a slip velocity. (b) Electrical Double Layer (EDL) thickness versus conductivity of a KCl solution. (c) Fluid flow pattern due to LACE in the absence of other forces at 1 kHz and 20 Vpp with an optical power density of 250 W/cm^2. Units of color bar are in m/s. (d) Fluid velocity due to LACE versus frequency at 20 Vpp and 250 W/cm^2. A line depicting the distance traveled in 1 second due to Brownian motion for a 10 μm particle is overlaid. Note that above 1 kHz the effects of LACE are negligible.

$$n_+ = n_0 \exp\left(\frac{-ze\phi}{kT}\right) \tag{2.26}$$

$$n_- = n_0 \exp\left(\frac{ze\phi}{kT}\right) \tag{2.27}$$

where n_0 is the intrinsic ion concentration, k is Boltzmann's constant, T is the temperature, e is the electron charge, and z is the valence of the ionic species (e.g. 1 for KCl). The net charge density, ρ_q, will be:

$$\begin{aligned} \rho_q &= ze(n_+ - n_-) \\ &= zen_0\left(\exp\left(\frac{-ze\phi}{kT}\right) - \exp\left(\frac{ze\phi}{kT}\right)\right) \\ &= -2zen_0 \sinh\frac{ze\phi}{kT} \end{aligned} \tag{2.28}$$

Now, applying Poisson's equation to Eq. 2.28 we receive a differential equation:

$$\frac{d^2\phi}{dx^2} = \frac{2zen_0}{\epsilon}\sinh\frac{ze\phi}{kT} \tag{2.29}$$

Applying the appropriate boundary conditions (at $x = \infty$, $d\phi/dx = \phi = 0$ and at $x = 0$, $\phi = \phi_0$) the solution to the above equation is [32]:

$$\phi = \frac{2kT}{ze}\ln\left(\frac{1 + \gamma\exp[-x/d]}{1 - \gamma\exp[-x/d]}\right) \tag{2.30}$$

where

$$\gamma = \frac{\exp[ze\phi_0/2kT] - 1}{\exp[ze\phi_0/2kT] + 1} \tag{2.31}$$

and the damping term, d, which can be interpreted as the electrical double layer thickness, is:

$$d = \left(\frac{2e^2n_0z^2}{\epsilon kT}\right)^{-1/2} \tag{2.32}$$

If we assume that the liquid conductivity, σ_m, is equal to $e\mu_m n_0$, where μ_m is the bulk ion mobility ($8 \times 10^{-8} m^2V^{-1}s^{-1}$ for KCl), we can transform 2.32 into an equation relating the liquid conductivity to electrical double layer thickness:

$$d = \left(\frac{2\sigma_m z^2 e}{\mu_m \epsilon kT}\right)^{-1/2} \tag{2.33}$$

Fig. 2.4b shows the dependence of the electrical double layer thickness on liquid conductivity for KCl. For a 1 mS/m solution, the double layer thickness is about 25 nm.

Now, we can find the electrical double layer thickness for a given solution. From this, we can determine the appropriate capacitance defined in the equivalent LACE circuit described in Fig. 2.4a. Now, we know the value of each of the circuit elements and, thus, for a given bias voltage and frequency, we can extract an approximate zeta potential.

Once the zeta potential is known, the tangential electric field is extracted from simulation and a slip velocity is calculated. This velocity enters into the Navier-Stokes equation as a boundary condition at the a-Si:H/liquid interface. The resulting fluid flow pattern is shown in Fig. 2.4c for a bias of 20 Vpp, 1 kHz, and 250 W/cm^2. Fig. 2.4d shows the maximum fluid flow due to LACE versus frequency for a bias of 20 Vpp and 250 W/cm^2. A line depicting the average Brownian motion in 1 second of a 10 μm particle is drawn for reference. Based on this analysis we expect LACE to be the dominant effect for frequencies below a frequency of 1 kHz.

2.2.4 Electro-thermal Effects (ET)

Theory of Electro-thermal Effects

The energy of incident photons absorbed in the a-Si:H is dissipated through either electron-hole pair or phonon generation. The latter can be modeled as a localized heat source in the a-Si:H layer. Additionally, joule heating in the liquid and a-Si:H occurs from the applied electric field ($\boldsymbol{E}$) according to the equation:

$$W = \sigma|\boldsymbol{E}|^2 \tag{2.34}$$

where W is the power generated per unit volume and σ is the conductivity of the medium. The generated heat results in a gradient in electrical permittivity and conductivity in the solution. In turn, these gradients interact with the surrounding electric field to produce a body force on the surrounding liquid. Following the approach of *Ramos et. al.*, we develop an expression for this effect.

The general expression for the electrical force, per unit volume, on an incompressible fluid is [36]:

$$\boldsymbol{f}_e = \rho_q \boldsymbol{E} - \frac{1}{2}\boldsymbol{E}^2 \nabla \epsilon_m \tag{2.35}$$

where ρ_q is the volume charge density, $\boldsymbol{E}$ is the electric field, and ϵ_m is the electrical permittivity of the medium. The first term in Eq. 2.35 is due to columbic attraction between ions in solution, whereas the second term is due to the dielectric force generated due to the liquid acting like a non-uniform dielectric. Dielectric forces dominate for AC fields with frequencies well above the inverse of the charge relaxation time of the liquid, while columbic forces dominate at the other end of the spectrum. The charge relaxation time for a liquid is $\tau = \epsilon_m/\sigma_m$ [36]. Therefore, for a 1 mS/m KCl solution, the transition between dielectric

and columbic forces will occur at around $f_c = 1/(2\pi\tau) = 230kHz$. Therefore, since OET typically operates in the hundreds of kilohertz range, we expect both dielectric and columbic forces to be present.

For small temperature gradients, we can express the temperature dependence of the conductivity and permittivity as: $\nabla\epsilon_m = \kappa_\epsilon\epsilon_m\nabla T$ and $\nabla\sigma_m = \kappa_\sigma\sigma_m\nabla T$, where T is the temperature, σ_m is the liquid conductivity, and κ_ϵ and κ_σ are empirical constants. Let us account for these small changes in conductivity and permittivity by introducing a small corrective term to the applied field $\boldsymbol{E}_0$. That is, $\boldsymbol{E} = \boldsymbol{E}_0 + \boldsymbol{E}_1$, where $\boldsymbol{E}_1$ accounts for the perturbation due to temperature. Noting that $\nabla \cdot \boldsymbol{E}_0 = 0$ and that $E_1 \ll E_0$, the volume charge density is:

$$\begin{aligned} \rho_q &= \nabla \cdot \epsilon_m \boldsymbol{E} \\ &= \nabla \cdot \epsilon_m(\boldsymbol{E}_0 + \boldsymbol{E}_1) \\ &\approx \nabla\epsilon_m \cdot \boldsymbol{E}_0 + \epsilon_m \nabla \cdot \boldsymbol{E}_1 \end{aligned} \tag{2.36}$$

combining with Eq. 2.35

$$\boldsymbol{f}_e = (\nabla\epsilon_m \cdot \boldsymbol{E}_0 + \epsilon_m \nabla \cdot \boldsymbol{E}_1)\boldsymbol{E}_0 - \frac{1}{2}\boldsymbol{E}_0^2\nabla\epsilon_m \tag{2.37}$$

Now, we want to find an expression for $\nabla \cdot \boldsymbol{E}_1$. To do this, let us look at the electrical continuity equation:

$$\frac{\partial \rho_q}{\partial t} + \nabla \cdot \sigma_m \boldsymbol{E} = 0 \tag{2.38}$$

where we assume that the divergence of the conduction of charge dominates the diffusion of charge [36]. Eq. 2.38 can be rewritten with our perturbed electric field, $\boldsymbol{E} = \boldsymbol{E}_0 + \boldsymbol{E}_1$:

$$\frac{\partial}{\partial t}(\nabla\epsilon_m \cdot \boldsymbol{E}_0 + \epsilon_m \nabla \cdot \boldsymbol{E}_1) + \nabla\sigma_m \cdot \boldsymbol{E}_0 + \sigma_m \nabla \cdot \boldsymbol{E}_1 = 0 \tag{2.39}$$

since $\boldsymbol{E}$ is time varying Eq. 2.39 can be rewritten as:

$$j\omega\nabla\epsilon_m \cdot \boldsymbol{E}_0 + j\omega\epsilon_m \nabla \cdot \boldsymbol{E}_1 + \nabla\sigma_m \cdot \boldsymbol{E}_0 + \sigma_m \nabla \cdot \boldsymbol{E}_1 = 0 \tag{2.40}$$

solving for the divergence of the perturbing field yields:

$$\nabla \cdot \boldsymbol{E}_1 = \frac{-(\nabla\sigma_m + j\omega\nabla\epsilon_m) \cdot \boldsymbol{E}_0}{\sigma_m + j\omega\epsilon_m} \tag{2.41}$$

Since we are dealing with a time dependent electric field, we can rewrite Eq. 2.37 to express the time averaged force:

$$\langle \boldsymbol{f}_e \rangle = \frac{1}{2} Re[\nabla\epsilon_m \cdot \boldsymbol{E}_0 + \epsilon_m \nabla \cdot \boldsymbol{E}_1 \boldsymbol{E}_0^*] - \frac{1}{2}|\boldsymbol{E}_0|^2\nabla\epsilon_m \tag{2.42}$$

and using our expressions for the divergence of the perturbing field (Eq. 2.41), $\nabla\epsilon_m$, and $\nabla\sigma_m$, we obtain the final expression for the time averaged force per unit volume due to electro-thermal forces ($\langle \boldsymbol{f}_{et} \rangle$):

$$\langle \boldsymbol{f}_{et} \rangle = \frac{1}{2} Re \left[\frac{\sigma_m \epsilon_m}{\sigma_m + j\omega\epsilon_m} (\kappa_\epsilon - \kappa_\sigma)(\nabla T \cdot \boldsymbol{E}_0)\boldsymbol{E}_0^* \right] - \frac{1}{2} |\boldsymbol{E}_0|^2 \kappa_\epsilon \epsilon_m \nabla T \tag{2.43}$$

For typical electrolytes, κ_σ = 2% K^{-1} and κ_ϵ = -0.4% K^{-1} [37].

Electro-thermal Effects in OET

The simulated fluid temperature distribution in the OET device for a 1 mW laser with a 20 μm beam diameter (250 W/cm^2) at a bias of 20 Vpp is shown in Fig. 2.5a. The maximum temperature increase is about 2.4 K. Here we assume a laser source with a Gaussian distribution and a 20 μm spot size for the heat source in the a-Si:H. The amount of heat generated is calculated by taking into account the laser power and spot size. It should be noted that if the heat generation due to optical absorption is too high, this will cause the liquid to boil. Our simulations indicate that this occurs for an optical power density of greater than 11 kW/cm^2. In reality, we expect this bound to be even higher due to the fact that we are assuming all incident optical power results in heat generation. Therefore, all simulations use this as an upper bound when plotting an effect versus optical power.

By calculating the temperature distribution for a given optical power density and bias, Eq. 2.43 can be entered into the Navier-Stokes equation as a perturbing force and the resulting fluid flow can be observed (Fig. 2.5b). Bias conditions assume 20 Vpp, 100 kHz, with an optical power density of 250 W/cm^2. The maximum fluid velocity versus optical power density (in the absence of all other effects) is shown Fig. 2.5c assuming a bias of 20 Vpp and 100 kHz. Notice that ET flow does not become prevalent for a 10 μm bead until the optical power is above 100 W/cm^2. In this figure, we linearly extrapolate the plot of Fig. 2.3c to predict the conductivities at high optical powers. This ignores the fact that the a-Si:H conductivity will saturate at high enough optical powers. Therefore, Fig. 2.5c provides a lower bound for when ET effects will occur.

In summary, the effects of ET flow will be dominant at high optical power densities (higher temperature gradients) and high electric fields.

2.2.5 Buoyancy Effects

Theory of Buoyancy Effects

The density of a liquid is a function of temperature. Therefore, a localized temperature gradient can result in a fluid density gradient which, under the influence of gravity, will result in fluid flow. To model this, we look at the potential energy density difference between two adjacent infinitesimal volumes of water:

$$\Delta E_g = \Delta\rho_v(T) \cdot \boldsymbol{g} \cdot \Delta\boldsymbol{x} \tag{2.44}$$

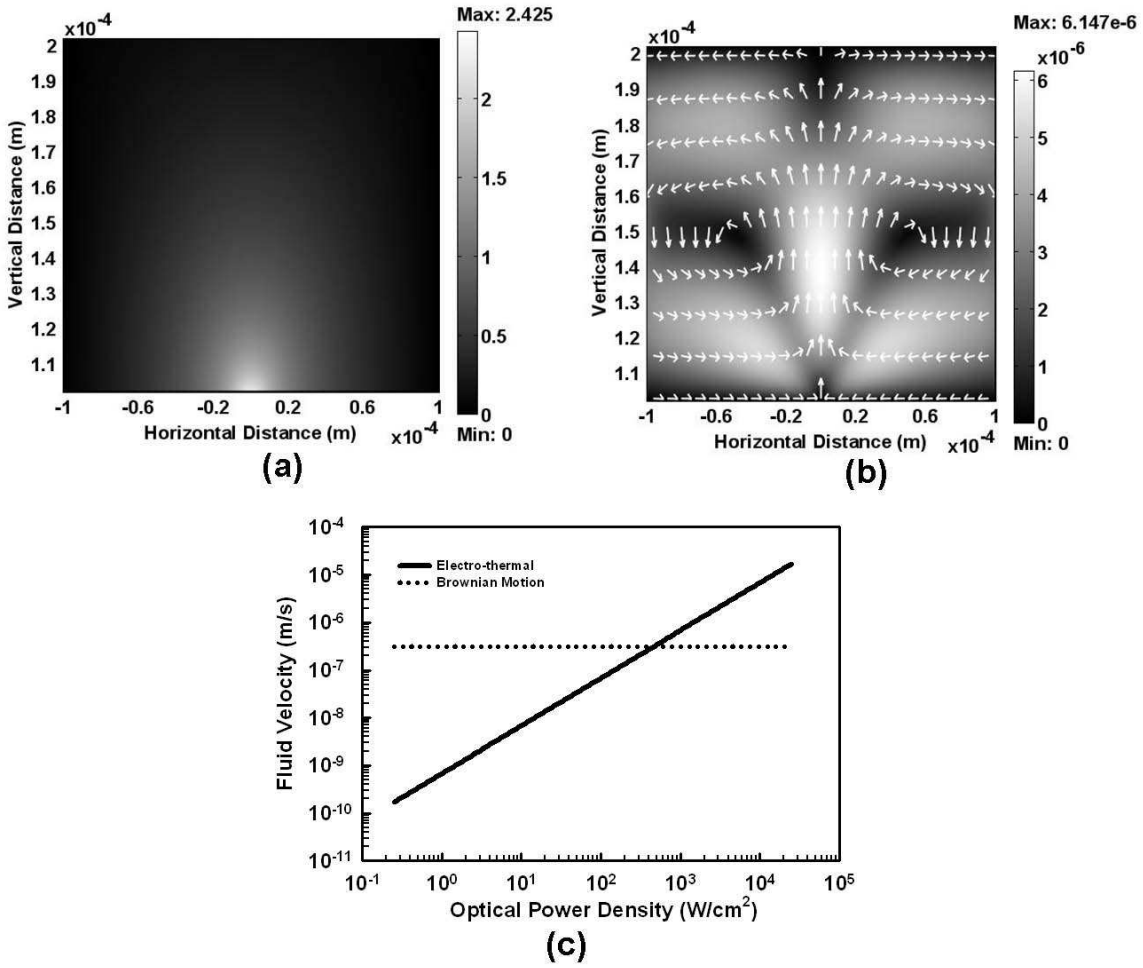

Figure 2.5: (a) Temperature increase distribution due to a 1 mW laser focused to a 20 μm spot size. (b) Simulated flow due to electro-thermal effects at 20 Vpp, 100 kHz, with an optical power density of 250 W/cm^2. Units of color bar are in m/s. (c) Dependence of ET fluid velocity on incident optical power density at 20 Vpp and 100 kHz.

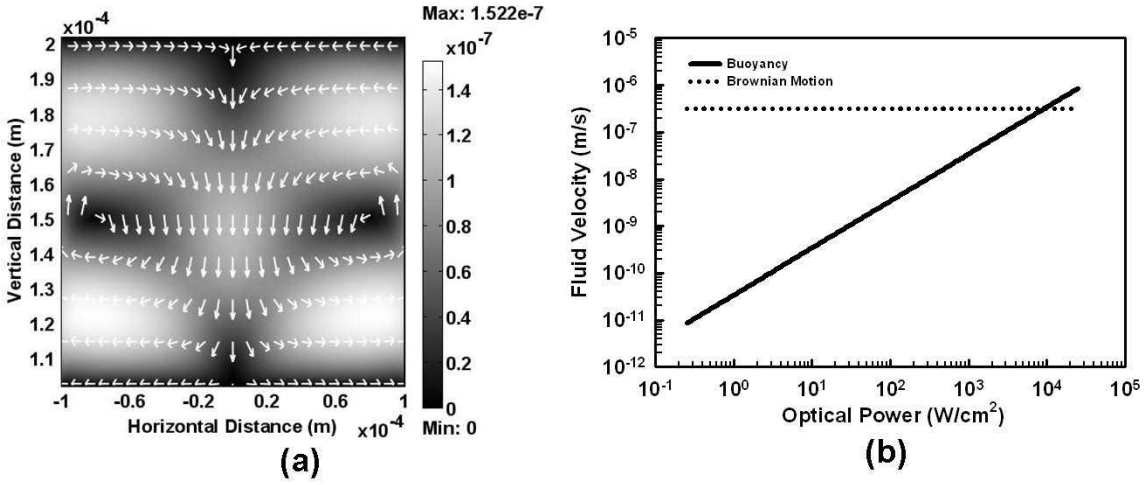

Figure 2.6: (a) Simulated fluid flow due to buoyancy effects at 20 Vpp, 100 kHz, and 250 W/cm^2. Units of color bar are in m/s. (b) Dependence of buoyancy fluid velocity on optical power density at 20 Vpp and 100 kHz. Note that the fluid velocity due to buoyancy is much smaller than that imposed by the other effects.

where, $\rho_v(T)$ is the temperature dependent fluid density and $\boldsymbol{g}$ is the acceleration due to gravity (9.8 m/s^2). Thus, the force density acting on the liquid is:

$$\boldsymbol{f}_g = \frac{\Delta E_g}{\Delta \boldsymbol{x}} = \Delta\rho_v(T) \cdot \boldsymbol{g} = \frac{\partial \rho_v}{\partial T}\Delta T \cdot \boldsymbol{g} \tag{2.45}$$

where ΔT is the difference in temperature between the two infinitesimal regions of fluid.

Buoyancy Effects in OET

Unlike the other effects mentioned already, this flow can occur in the OET device in the absence of applied bias. Thus, given a high enough temperature gradient, it is possible to move objects in the absence of applied bias. This force, like the ET force, is entered into the Navier-Stokes equation as a fluidic perturbation. The resulting fluid flow is shown in Fig. 2.6a at 20 Vpp, 100 kHz, and 250 W/cm^2. The maximum fluid velocity versus optical power density is shown in Fig. 2.6b at 20 Vpp and 100 kHz.

As one can see, the magnitude of buoyancy driven flow is much less than the other effects. Buoyancy does not exceed Brownian motion for a 10 μm bead until the optical power is above 104 W/cm^2. However, one should note that the flow pattern is anti-parallel to that of both ET and LACE. This will result in a minimum in the fluid velocity as buoyancy is overcome by the other effects. As explained above, the a-Si:H conductivity has been linearly extrapolated for high optical power densities from Fig. 2.3c.

Therefore, we do not expect buoyancy to play a role in OET operation except in the absence of external biasing.

2.2.6 Development of a Figure of Merit

In order to determine which of the aforementioned effects is dominant for a given set of device and bias conditions, a figure of merit must be developed. Since all of the effects described eventually manifest themselves as a fluid or particle velocity, it is natural for the figure of merit to be a function of velocity. Specifically, we can compare the speed due to DEP to that induced by other effects in the fluid. Thereby, we define a dimensionless value β for each point in the liquid as:

$$\beta \equiv \frac{X_{DEP}}{X_{DEP} + X_{EXT} + \langle X_{BROWNIAN} \rangle} \tag{2.46}$$

where X_{DEP}, X_{EXT}, and $\langle X_{BROWNIAN} \rangle$ refer to the distance the particle travels in one second due to DEP, external forces (LACE, ET, and Buoyancy), and Brownian motion, respectively. The average distance a spherical particle travels in one second due to Brownian motion is [38]:

$$\langle X_{BROWNIAN} \rangle = \sqrt{\frac{kT}{3\pi\eta a}} \tag{2.47}$$

Therefore, a β value close to 1 corresponds to near complete dominance, or control, by the DEP force. Likewise, a β value near 0 indicates DEP has little control over the particle motion.

Applying this definition of β to the simulation grid, one receives a value of β for each point in the mesh. It is therefore necessary to reduce this array of β values down to a single number, or figure of merit. Thus, we define a number B as:

$$B \equiv \frac{1}{A} \int \beta dx dy, x \in [-r, r], y \in [0, d] \tag{2.48}$$

where r is defined as a control radius, d is the thickness of the liquid layer, and A is the area of integration equal to $2 \times r \times d$. The control radius is determined by the greatest radius from the beam center at which any particle perturbation is expected. Fundamentally, ignoring all other effects, DEP can induce a particle velocity at a distance, defined in Fig. 2.7a, from the beam center until it is overcome by Brownian motion. Fig. 2.7b shows this distance as a function of particle size. It can be seen that for a 10 μm particle operating at 10 Vpp in 1 mS/m solution, the control radius is about 240 μm. Therefore, for this particle in a device with a 100 μm, 1 mS/m liquid layer, we integrate β over an area equal to $2 \times 240 \times 100$ μm^3 and then divide by this area.

The control radius described above is difficult to measure experimentally. This is due to its definition. The control radius assumes that there are no external forces, outside of DEP

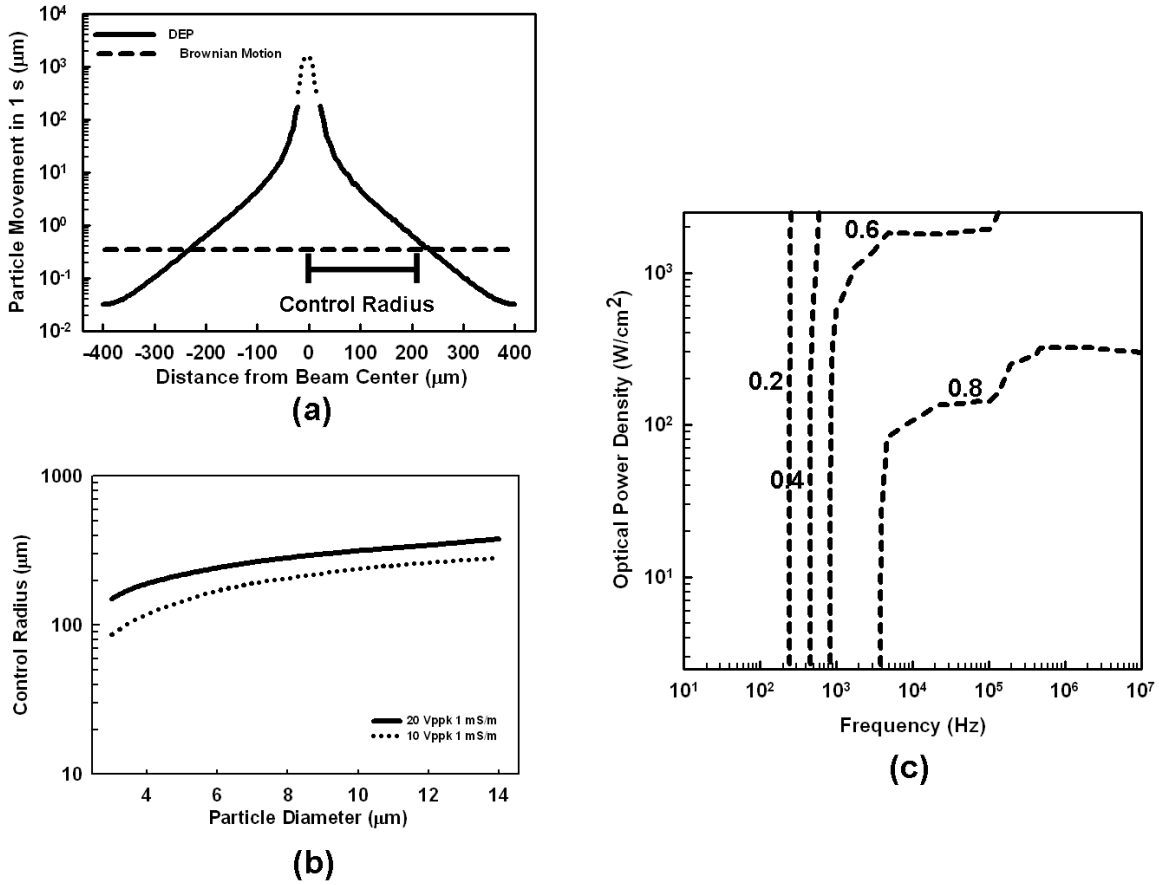

Figure 2.7: (a) Definition of control radius. The dotted region corresponds to points within 16 μm of the beam center which are not valid due to the effects of vertical DEP forces acting on the particle. (b) Dependence of control radius on particle size for 1 mS/m solution biased at 20 Vpp and 10 Vpp. (c) Contour plot of B for a 10 μm particle in 1 mS/m at 10 Vpp.

and Brownian Motion, acting on the particle. In reality, the other forces are always present to some degree. This greatly reduces the measured control radius relative to the experimental value. For example, for a 15 μm particle under the conditions listed for Fig. 2.7b at 20 Vpp, we measure a control radius of 190 μm. Theoretically, we expect a value of 280 μm. The discrepancy is due to the fact that at large distances other forces, namely electro-thermal, counteract the relatively weak DEP force and, thus, reduce the measured control radius. Since the measured control radius is highly dependent on experimental setup, it is proposed that the theoretical control radius should be used in the calculation of B as it provides a more consistent and fundamental definition.

B is an average value of β over a predefined area. Therefore, it exists between 0 and 1, and can be interpreted as the likelihood of DEP control for a given set of parameters. Fig. 2.7c shows a contour plot of B as a function of optical power density and frequency for a typical set of device parameters and biasing. One can see that for low frequencies and high optical power densities, it is predicted that DEP has little control due to LACE and ET effects, respectively.

2.2.7 Experimental Methods and Results

Methods

A 10 mW, 635 nm diode laser in series with a continuous attenuator and 10x objective was used as the illumination source. Fig. 2.8 shows the experimental setup.

The OET device was fabricated as described Appendix A.1 and subjected to a variety of bias points which varied in voltage, frequency, and optical power for a solution containing 10 μm polystyrene beads with a conductivity of 1 mS/m.

For each bias point, the dominant effect was recorded (DEP, LACE, ET, Buoyancy, or Brownian motion). Video images of particle movement were analyzed and the dominant effect was determined based on the following rules. DEP was defined as when a particle could be repelled greater than 5x its diameter from the beam center and not be moved further by any ambient induced flow. LACE was differentiated from ET flow by assuming if a flow based effect was dominate for a frequency below 1 kHz, it was attributed to LACE. If flow was dominant at frequency higher than 1 kHz, it was then assumed to be ET in origin. Arguably, there is a gray area in the transition area around 1 kHz at high optical powers (i.e. where ET would be possible). In this region, both ET and LACE are simultaneously occurring and it is very difficult to distinguish between the two. Thus, for high optical powers and frequencies below 1 kHz, LACE is the putative dominant effect (However, the reader should realize that there is contribution from ET as well in this regime.). Buoyancy was ignored when a non-zero voltage was applied as its effects are much less than the other forces present. If no significant particle response was recorded, it was assumed that Brownian motion was the dominant mechanism. Quite often, electrolysis of the liquid, in conjunction with LACE, occurred for low frequency biasing. This is noted as LACE/Electrolysis.

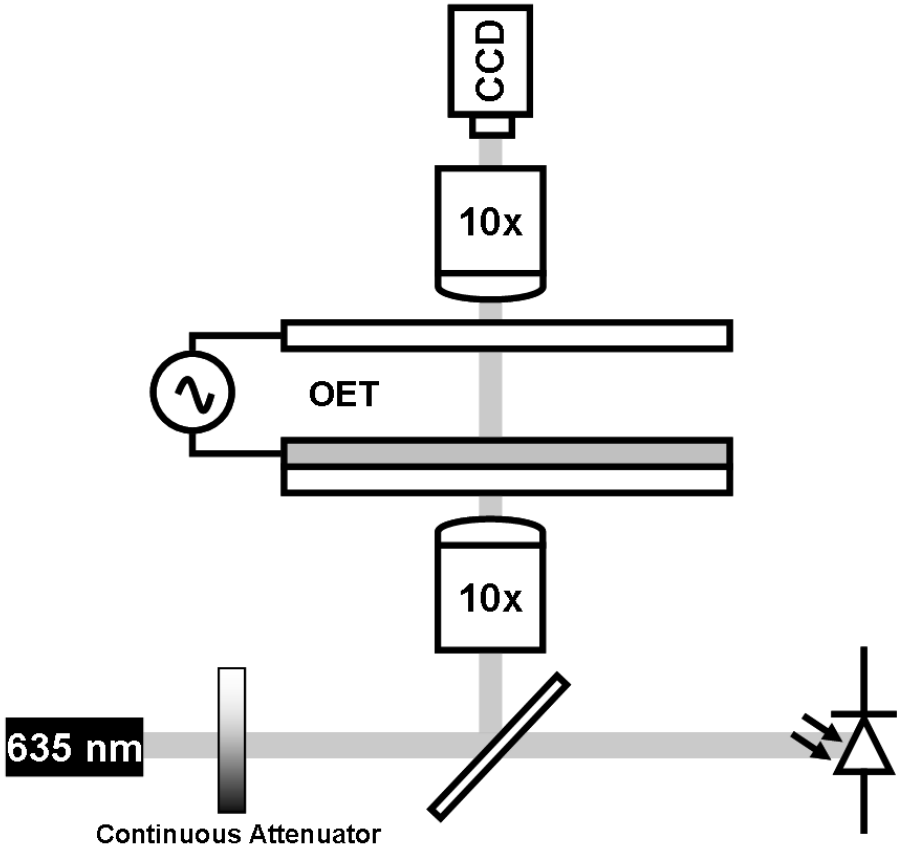

Figure 2.8: Depiction of experimental setup. A 635 *nm* diode laser is fed through a continuous attenuator followed by a 50/50 beam splitter. Half of the beam goes to a photo detector while the other half is sent through a 10x objective and is focused onto the device substrate. Observation occurs through a topside 10x objective connected to a CCD camera.

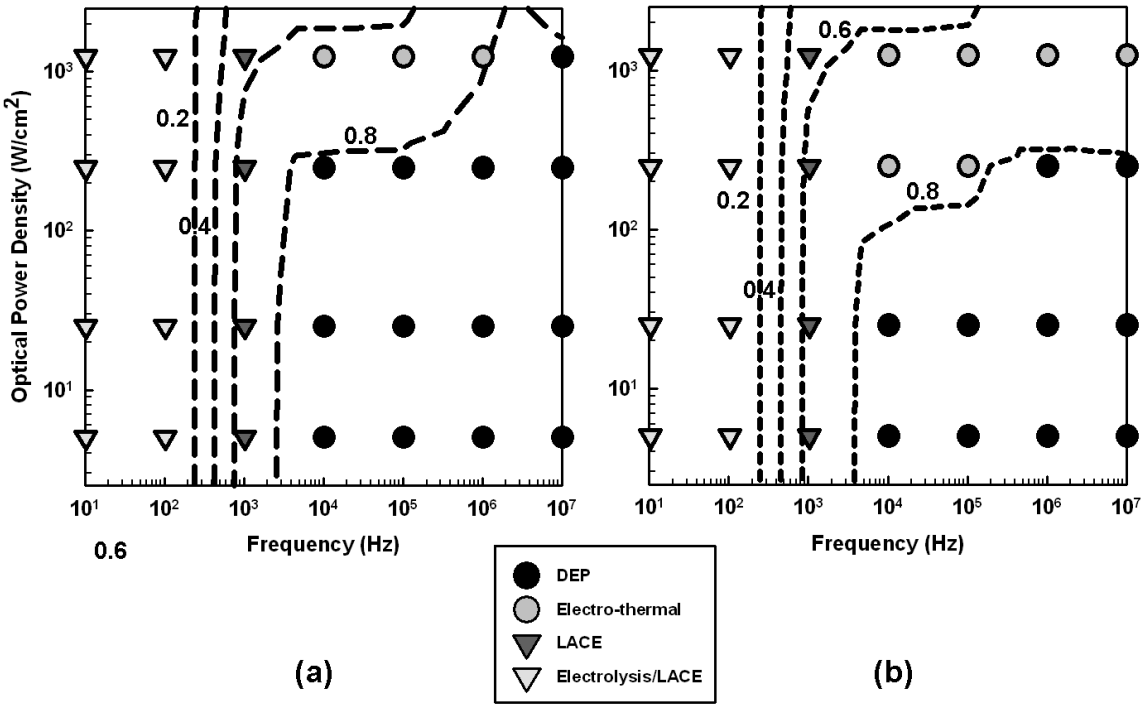

Figure 2.9: Overlay of observed dominant effect with theoretical predictions for 1 mS/m[1] at 20 Vpp (a) and 10 Vpp (b). All DEP observations occur when the B value is greater than 0.8. Note that in the regimes of low frequency ($<$ 1 kHz) and high optical power (>100 W/cm^2) likely both LACE and ET are present, however here LACE is the putative dominant effect.

Experimental Results

The experimental and simulated results are shown in Fig. 2.9. Simulated values of B are plotted on a contour plot while experimental results are overlaid as points. The simulation includes all of the aforementioned effects and assumes all the device dimensions described above.

The experimental results follow the trends of the B contour lines. It appears that, for this liquid solution, a normalized B value of greater than 0.8 results in DEP actuation. DEP actuation, as predicated by the theory, is overcome by LACE at low frequencies, ET at high optical powers, and both LACE and ET at high optical powers and low frequencies. Therefore, it appears that to ensure DEP dominance over external effects (e.g. LACE, ET, Buoyancy) the OET device should be operated at frequencies above the LACE cutoff (1 kHz for 1 mS/m solution) and low optical power densities (less than 1 kW/cm^2 for this device).

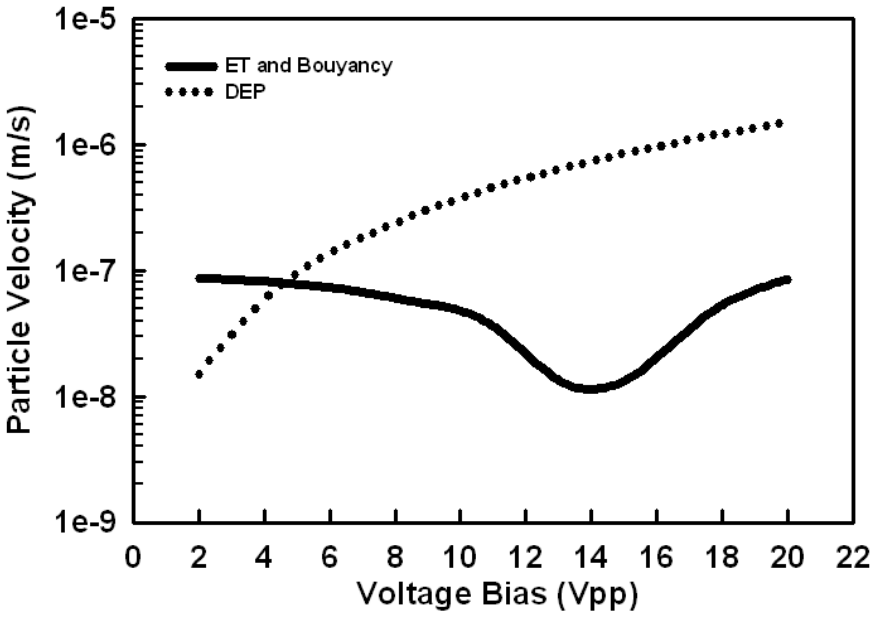

Figure 2.10: Comparison of simulated particle velocity due to ET and buoyancy effects. Competition between ET and buoyancy results in a localized minimum allowing DEP to have greater control at higher voltages.

As one can see, a reduction in voltage (20 Vpp to 10 Vpp) reduces the overall DEP control range (i.e. the arc length of the contour line corresponding to a B of 0.8 shrinks). This is somewhat counterintuitive at first since both DEP and ET scale with the square of the voltage (assuming most of the heat generation is due to laser absorption). However, the effect manifests itself as a competition between buoyancy driven flow and electro-thermal flow. From Fig. 2.5b and 2.6a, one can see that the flow directions are anti-parallel to one another. Therefore, there will be a threshold voltage at which ET driven flow will reverse the direction of the voltage independent buoyancy driven flow (It is assumed that LACE has negligible effect at the frequencies of interest and Joule heating is negligible relative to laser heating.). This results in a minimum fluid velocity. Due to this local minimum, DEP can control a larger area for higher applied voltages. This can be seen from Fig. 2.10.

2.2.8 Summary of Physical Effects in OET

There are a variety of other parameters that affect the percentage of DEP control on a particle in the OET device. Perhaps most prevalent is particle size. The DEP force scales as the cube of particle radius. Since the other effects do not scale with particle size (aside from Brownian motion), the relative contribution of DEP to particle control will decrease sharply with decreasing particle diameter. However, we have only considered particles which exhibit negative DEP. Certain particles have positive CM factors which result in an attractive force

towards the illuminated region. In this case, it is conceivable that external forces can actually aid in particle trapping. This is because external fluid flow, such as LACE or ET, can bring the particle of interest towards the beam where it is trapped by the strong DEP force near the beam center. In these cases, smaller particles may be able to be trapped via DEP despite relatively small forces outside of the beam center. Additionally, particle geometry plays a role. For example, nanowires exhibit a much larger CM factor due to their cylindrical shape. Therefore, it is possible to use DEP to trap and manipulate individual nanowires [39].

It is also possible to alter the device geometry to control smaller particles with DEP. By decreasing the thickness of the liquid layer, a larger electric field gradient is produced which results in an increased DEP force. This technique can be used for the manipulation of particles down to the nanoscale regime [40]. However, for certain biological applications, such as cell manipulation, the gap spacing must be large enough to enable the viability of the cells themselves.

Another major parameter of interest is liquid conductivity. The OET device relies on the ability to switch voltage to the liquid layer upon illumination. If the liquid conductivity increases, the amount of voltage switched to the liquid layer will decrease. Therefore, DEP actuation is decreased for high liquid conductivity. This is an area of concern because many of the biological applications of OET require the use of high conductivity media. As a result, a method of increasing the effects of the light actuated switching mechanism is needed. One way to accomplish manipulation in high conductivity media is to replace the photoconductive layer by a phototransistor structure [41]. With the added gain of the phototransistor, voltage can be more efficiently switched to the liquid layer resulting in DEP actuation even in high conductivity media.

We have presented a framework for the forces present during the use of optoelectronic tweezers. It is clear that a multitude of physical effects are present in the OET device. These effects manifest themselves in different operating regimes. By developing a figure of merit to quantify the relative contributions due to each of these forces, we are able to accurately predict where DEP actuation is most likely to occur for a set of bias and device parameters.

Depending on bias conditions, the particles in the OET device will be influenced by a variety of effects. These include Light Induced AC electro-osmosis, electro-thermal, buoyancy, and dielectrophoresis. Fig. 2.11 summarizes the general operational characteristics of the OET device as functions of optical power and frequency. The exact partitions between different regimes will depend on the device geometry, particle, and suspending medium. As one can see, LACE dominates for low frequencies while ET is prevalent at high optical powers. DEP actuation occurs for higher frequencies and lower optical powers. For the device discussed here, in order to insure DEP actuation, the optical power density must be kept below 100 W/cm^2, the voltage should be in the range of 10 to 20 Vpp, and the bias frequency must be above the LACE cutoff of approximately 1 kHz (Table 2.1).

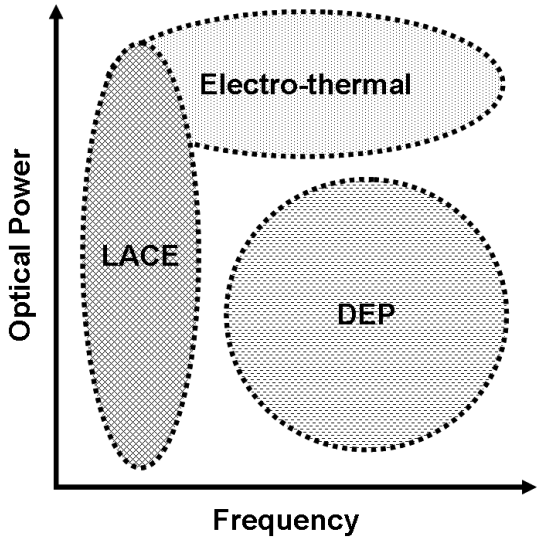

Figure 2.11: Dominant effect present in OET as a function of optical power and frequency.

Table 2.1: OET Regimes of Operation

$\sigma = 1\ mS/m$		
	Frequency Span	Optical Power
DEP	1 kHz - 10 MHz	0.1 W/cm^2 - 100 W/cm^2
LACE	0 kHz - 1 kHz	$> 0.1\ W/cm^2$
ET	0 kHz - 10 MHz	$> 100\ W/cm^2$

2.3 Light-induced Electrowetting

2.3.1 Theory of Electrowetting

Electrowetting refers to the change in contact angle (i.e. change in surface tension) of a liquid on a surface under an applied electrical potential. If the contact angle on one side of a droplet is different than the contact angle on the opposite side, a net force is exerted on the droplet resulting in droplet translation. In general there are other forces, such as DEP or thermocapillary, that also can aid in droplet translation. However, in our case, electrowetting will be the dominant mechanism. In the following section, we will present a very simple energy based model for illustrating the manifestation of the electrowetting force [42]. Then we will discuss how this force is realized in the OEW device (i.e. using light instead of lithographically defined electrodes to exert electrowetting forces).

Electrowetting is typically realized by lithographically patterning electrodes on a substrate. In theory, a droplet placed directly on these electrodes will wet the surface under an applied potential. However, in practice, this is typically not done as unwanted electro-

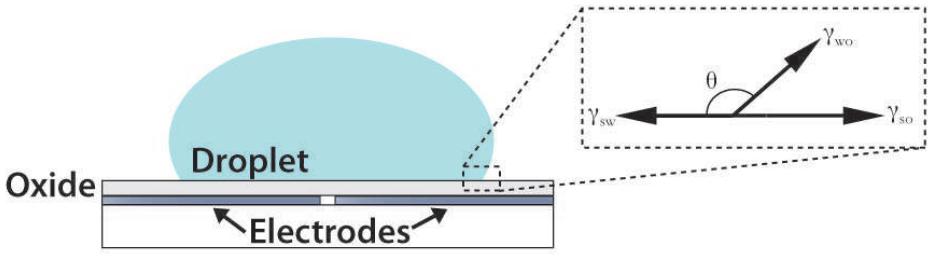

Figure 2.12: Simple electrowetting-on-dielectric setup. Electrodes patterned on a substrate are covered in an insulating oxide layer (additional hydrophobic layer and topside grounding electrode not shown). At the contact point, there is an equilibrium established between the three different surface tensions (γ_{wo}, γ_{so}, γ_{sw}) that defines the contact angle, θ.

chemical reactions (e.g. electrolysis) often occur. This is due to the fact that all of the voltage is dropped across the electrical double layer at the water-electrode interface. To circumvent this issue, a layer of oxide is placed over the electrodes, isolating the metal surface from the liquid droplet. This is referred to in the literature as Electrowetting-on-dielectric (EWOD). Additionally, a hydrophobic layer (e.g. Teflon) is typically deposited on top of the oxide in order maximize the contact angle change under an applied electrical bias (resulting in improved droplet speed/movement). There is also a grounding electrode that typically sandwiches the droplet between a top and bottom substrate. In this simple example we will remove the top substrate and simply use a wire to ground the droplet.

Fig. 2.12 shows the typically electrowetting setup. A substrate has metal electrodes patterned on it and is covered in an oxide layer. The hydrophobic layer is removed for clarity here as well as the top grounding electrode. In order to understand how a force arises, we first want to look at surface tensions of the contact line. This is the point where the substrate, liquid, and external environment (typically an inert oil) meet. At this point, there is an equilibrium that is achieved between the three different surface tensions interacting. Namely, these are the water-oil (γ_{wo}), substrate-oil (γ_{so}), and substrate-water (γ_{sw}). The energy minimization is achieved by varying the contact angle (as defined in Fig. 2.12). Based on Fig. 2.12 we can deduced that, in equilibrium, the horizontal components of the surface tension must cancel. This results in the following relationship:

$$\gamma_{wo} \cos\theta = \gamma_{so} - \gamma_{sw} \tag{2.49}$$

Next we want to understand what happens when an electrical potential is applied to one of the electrodes. To do this, we employ Lippman's equation [43]:

$$\partial\gamma_{sw} = -\sigma_s \partial V \tag{2.50}$$

where V is the applied voltage and σ_s is the surface charge density. This says that the change in contact angle per unit voltage is simply equal to the surface charge density at

the water-substrate interface. Integrating this expression to find the total change in surface tension due to an applied potential is:

$$\begin{aligned} \gamma_{sw} &= \gamma_{sw}^{o} + \int_0^V \partial\gamma_{sw} \\ &= \gamma_{sw}^{o} - \int_0^V \sigma_s \partial V' \end{aligned} \tag{2.51}$$

where γ_{sw}^{o} is the surface tension in the absence of an applied voltage. Now, we assume that the interface charge density is due solely to the surface charge density (ρ) in the stored on the oxide layer and treat this capacitor (C_{ox}) as a perfect parallel plate (we can ignore the charge in the electrical double layer here since the oxide capacitance will dominate because the oxide thickness (100 nm) is much thicker than the double layer thickness (10 nm)). With this we find:

$$\begin{aligned} \rho &= \sigma_s = C_{ox} V \\ &= \frac{\epsilon_{ox}}{d_{ox}} V \end{aligned} \tag{2.52}$$

where ϵ_{ox} and d_{ox} are the oxide electrical permittivity and thickness, respectively. Substituting Eq. 2.52 into Eq. 2.51:

$$\begin{aligned} \gamma_{sw} &= \gamma_{sw}^{o} - \frac{\epsilon_{ox}}{d_{ox}} \int_0^V V' \partial V' \\ &= \gamma_{sw}^{o} - \frac{\epsilon_{ox}}{2 d_{ox}} V^2 \end{aligned} \tag{2.53}$$

Eq. 2.53 states that the substrate-water surface tension will be reduced by a factor equivalent to the energy per unit area stored in the oxide layer under an applied voltage V. Now that we understand how an applied potential will change the surface energy (and contact angle) of the substrate-water interface, we can move towards developing an expression for the force that results when the surface energy (or contact angle) on one side of the droplet is different than that on the other side. In other words, if we apply a voltage to only one of the electrodes in Fig. 2.12.

We know that when only one of the electrodes (say the right one as illustrated in Fig. 2.13), the surface tension on one side of the droplet will be different than that on the other side. This difference will be equal to the capacitative energy density in the oxide layer. This sets up an spatial energy gradient, which, of course, implies there is a net force acting on the droplet. To elucidate this further, using Eq. 2.53 lets first sum up the droplets total energy (E_{tot})in the situation depicted in Fig. 2.13.

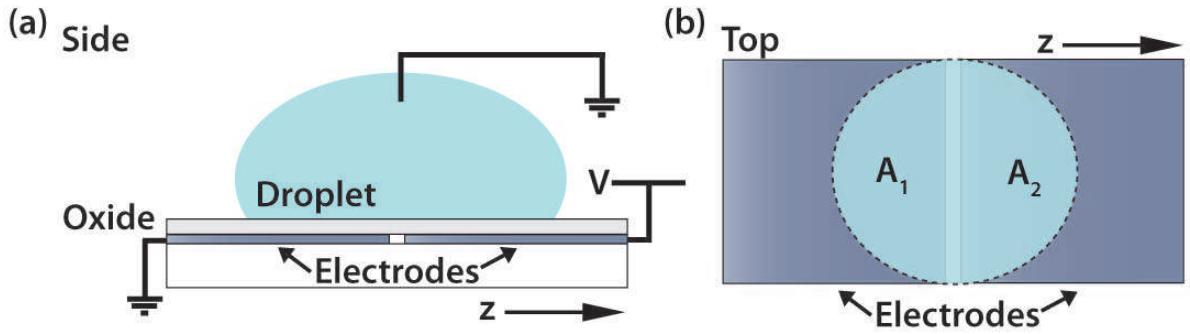

Figure 2.13: (a) Side view of setup for depicting electrowetting force. In this scheme, a voltage, V, is applied to the right-hand electrode while both the droplet itself and other electrode are grounded. This setups up a spatial gradient in surface energy, which drives droplet movement to the right (z-direction). (b) Top view of same scheme but defining the areas the droplet encompasses on the left electrode (A_1) and right electrode (A_2). Note these areas will be functions of position, z, as the droplet translates.

$$\begin{aligned} E_{tot} &= (\gamma_{sw}^{o} - \frac{\epsilon_{ox}}{2d_{ox}} V_1^2) A_1(z) \\ &+ (\gamma_{sw}^{o} - \frac{\epsilon_{ox}}{2d_{ox}} V_2^2) A_2(z) \\ &+ \gamma_{wo} A_{rest} \end{aligned} \tag{2.54}$$

where A_1 and A_2 are the areas that the droplet covers on the left and right electrode, respectively (This is graphically depicted in Fig. 2.13b. Note this will be dependent on the position of the droplet as it translates and therefore are functions of z). V_1 and V_2 are the voltages that drop across the oxide capacitor formed by areas A_1 and A_2. A_{rest} is the remaining surface area of the droplet that is in contact with the surrounding oil environment. The first term in Eq. 2.54 refers to the interfacial energy of the droplet and the left electrode, the second term refers to the interfacial energy of the droplet and the right electrode, and the final terms refers to the interfacial energy of the droplet and surrounding oil environment. Additionally, per the electrode biasing scheme depicted in Fig. 2.13a, the entire applied voltage V will only drop across the capacitor formed by A_2(z). Thus, Eq. 2.54 reduces to:

$$\begin{aligned} E_{tot} &= (\gamma_{sw}^{o} - \frac{\epsilon_{ox}}{2d_{ox}} V^2) A_2(z) \\ &+ \gamma_{wo} A_{rest} \end{aligned} \tag{2.55}$$

Now, to find the net force, we simply differentiate Eq. 2.55 with respect to z:

$$\boldsymbol{F_{ew}} = -\frac{dE_{tot}}{dz}\hat{\boldsymbol{z}} = \left(\frac{\epsilon_{ox} V^2}{2d_{ox}}\right) \frac{dA_2(z)}{dz}\hat{\boldsymbol{z}} + \left(\frac{\epsilon_{ox} V}{d_{ox}}\right) A_2 \frac{dV}{dz}\hat{\boldsymbol{z}} \tag{2.56}$$

The second term in Eq.2.56 will be zero, since the the applied potential V is a constant. In general, this is not true, since the voltage, V_2, across the oxide will not always exactly equal V (and therefore varies as the capacitances associated with left and right electrodes change during droplet translation), particularly if there is a topside oxide layer separating the grounding electrode from the liquid layer. However, in our simplified case, the term does drop out and we are left with the final equation describing the electrowetting force:

$$\boldsymbol{F_{ew}} = \left(\frac{\epsilon_{ox} V^2}{2d_{ox}}\right) \frac{dA_2(z)}{dz} \hat{\boldsymbol{z}} \tag{2.57}$$

As one can see the act of applying an electrical potential to one side of the droplet results in a force that is proportional to the capacitative energy stored in the oxide layer as well as a geometric term which describes how the overlap area of the energized electrode varies spatially (This geometric factor is simply an algebraic formula that can be worked out. For instance see [42]).

Based on Eq. 2.57, in order to maximize the force we want to maximize the capacitance of the oxide layer. This boils down to using as thin an oxide layer as possible. However, the quality of this thin oxide must be high in order to insure there are no pinholes in the layer which would lead to points where electrolysis and other electrochemical interactions could occur. In the case of our device, we use an atomic layer deposited oxide which allows us to produce extremely high quality thin films. In this way, we can maximize the force and subsequently reduce the voltage necessary for droplet translation.

2.3.2 Light-induced Electrowetting in OEW

As described above, electrowetting is typically achieved by patterning individually addressable electrodes on a surface. As the size of the droplet shrinks and the area over which the droplet must be actuated grows, the number of electrodes required becomes very large and complex addressing schemes (and fabrication schemes) must be employed. To get rid of this constraint we replace the patterned electrodes with a uniform photosensitive layer. This structure is identical to the OET device (Fig. 1.2a) save for the existence of an oxide layer between the photosensitive film and liquid. When illuminated, electron-hole pairs are created which locally increases the conductivity of the photosensitive layer. This has the effect of causing the externally applied voltage in the illuminated regions to drop across the oxide layer (in the dark regions it will drop across the photosensitive layer). Therefore, the illumination pattern on the device functions like energizing an electrode whose shape is the same as that of the light pattern. Thus, if one side of a droplet is illuminated, the droplet will experience an electrowetting force which causes translation towards the illuminated region. As above, we refer to this device as Optoelectrowetting (OEW, Fig. 1.2b). Since the light patterns define the location of the electrodes, it is very easy to manipulate large numbers of droplets simultaneously (simple by increasing the number of optical patterns on the chip (this is easily accomplished with a standard spatial light modulator)) as well as droplets of varying size (by projecting different sized light patterns that correspond to the different

sized droplets). These two attributes would be very difficult to implement in a standard, electrode-based electrowetting device.

Now, with an understanding of the various physical phenomena present in both the OET and OEW device, we can proceed to apply these devices towards realizing the three main functions of a generic μTAS system.

Chapter 3

Pre-implantation Mouse Embryo Selection Guided by Light-Induced Dielectrophoresis

Monsters exist, but they are too few in numbers to be truly dangerous. More dangerous are the functionaries ready to believe and act without asking questions.

- Primo Levi, *The Reawakening*, 1963.

Our first task in realizing the generalized functions of the micro-total analysis system is to use Light-induced electrokinetics to analyze and/or interrogate an intrinsic property of a sample. Here, as an example, we will explore the use of OET to profile the electrical properties of developing embryos as a means to assess their developmental potential for *in vitro* fertilzation (IVF).

3.1 Motivation

Human IVF is one of the greatest scientific advances of the twentieth century. Since the first successful report of an IVF live birth in 1978 [44], IVF has provided fertility to countless people previously considered infertile due to idiopathic causes, the natural aging process, anatomic abnormalities, and even the absence of sperm or eggs. Furthermore, IVF allowed human embryo development to be studied in real-time, beginning at the earliest stages of development. Additionally, IVF and related techniques, such as *in vitro* culture, have made human embryonic stem cell research and therapies possible. The use of IVF has increased dramatically in the last 3 decades. In the U.S. today, 1-3% of all births are achieved using *in vitro* assisted reproductive techniques (ART) [45–47].

Despite its rapid rise, IVF is criticized for significant limitations in 3 critical domains: success rate (defined as live births per number of embryos transferred), morbidity (health risk to mother and fetus), and cost (to patient, and health-care system) [45, 46]. In 2007,

the proportion of IVF cycles that resulted in a live birth varied between 8.9% to 39.9%, and likelihood of success decreased significantly after the fourth cycle [48]. Due to the relatively low success rate of IVF, an average of 2-3 embryos are typically transferred to the mother per cycle; this results in a high multiple-birth rate (up to 34.7% in women > 35 years of age) [49]. A multiple-birth pregnancy is the single greatest source of morbidity and mortality to both mother and fetus [45, 50], as these are closely associated with prematurity, low birth weight, Caesarian section, and, for both mother and fetus, increased risk of prolonged hospital stay, disability, or death [50, 51]. In the U.S., IVF is not provided by most health insurance plans and the average cost of a single cycle for IVF today is $\$12,400$ [52]; the average number of cycles per live birth is > 3 (2007 data) [53]. Poor outcomes with respect to these 3 domains (success rate, morbidity, and cost) are rooted, at least in part, to our inability to reliably predict which 1 - 2 embryos, produced *in vitro*, is likeliest to result in a live birth following transfer to the uterus.

Today, selection of specific embryos for uterine transfer is based primarily on morphologic parameters; only those that appear the most developmentally mature are selected. This practice is based on the notion that, since all embryos are fertilized at approximately the same time, those that have developed the furthest at a given time point are likeliest to have the greatest developmental potential. However, it is now accepted that morphologic parameters are not an entirely reliable index of embryo quality, and, as a consequence, intense interest is focused in developing more reliable methods for embryo selection [54, 55]. The low success rate, high risk of morbidity and mortality, and high cost could all be improved significantly if a metric were available with which to reliably predict the viability of each individual embryo, prior to transfer. This would make it possible to transfer only the healthiest and fewest number of embryos (ideally only one), and, thereby, reduce the rate of multiple births without reducing pregnancy rates [55, 56].

Dielectrophoresis (DEP) has been suggested as a potentially useful assay to guide embryo selection for transfer [57]. DEP refers to the response of the induced dipole moments of particles due to the application of an external non-uniform electric field [58]. It is used as a non-invasive technique to manipulate a multitude of objects ranging from cells [20, 59, 60] to nanowires [61, 62]. The response of an object, such as a cell, to DEP is characterized by the real part of the Clausius-Mossotti (CM) factor. This is an effective electrical polarizability of the object relative to that of the surrounding medium. The CM factor takes into account all of the physical properties of the object and media. This CM factor can either be positive or negative in value (attractive or repulsive forces) depending on the relative admittances of the particle (cell) and media. Cells in different physiologic states possess distinctly different electrical properties, resulting in different DEP responses [63, 64]. Accordingly, DEP has been used to distinguish between live, dead, and non-viable cells [65–67], as well as between different cells types [68].

In 2005, we reported a method termed Optoelectronic Tweezers (OET), which uses optical images to create DEP electrodes (light-induced dielectrophoresis) [69]. In the device, low intensity ($< 1 W/cm^2$) incoherent light interacts with a photosensitive substrate and, in conjunction with an externally applied electrical bias, creates localized DEP traps in the

illuminated areas (Figs. 1a and 1b). On-demand, parallel DEP trap generation is possible simply by altering the optical pattern. This technique affords many of the advantages of standard optical manipulation techniques (e.g., optical tweezers [12], plasmonic tweezers [16]), however using far less optical power (up to 10^5x less [69]) as well removing the requirement of static electrodes used for more conventional DEP manipulation platforms [59, 62, 70, 71].

While the DEP response of oocytes and 1-cell (pre-cleavage) stage embryos has been studied [57, 72], the response of post-cleavage embryos to DEP, and, how such responses scale with developmental stage, has not been reported. Since pre-transfer embryo viability screening is performed primarily on post-cleavage stage embryos [73], it is essential to both understand, and be able to predict, the latter's response to DEP.

Given the multitude of structural changes that occur throughout embryo development from the 1-cell to expanded blastocyst stages, we hypothesized that an embryo's response to OET should change, in a predictable fashion, in parallel to developmental stage. Changes in morphology have been correlated to significant changes in the electrical properties of 1-cell to blastocyst stage embryos of various species [57,74,75]. This scaling of electrical properties can result in large fluctuations in the DEP response of pre-implantation stage embryos and, therefore, provide a quantitative means by which to assess embryo morphology and/or health (Fig. 3.1c).

Using a hybrid inbred mouse model and standard OET apparatus, we first determined how embryos, cultured in an optimized culture medium (KSOM+AA), respond to OET (DEP) at varying stages of development (1-cell, 2-cell, 4-to-16-cell/morula, and, early and late blastocyst stages). Next, to assess whether this technique could be used to guide embryo selection, we compared responses from embryos cultured in KSOM+AA to morphologically identical embryos cultured in a sub-optimal medium (M16). *In vitro* culture in M16 yields, at all pre-implantation stages of development, a subset of embryos that are indistinguishable from ones cultured in KSOM+AA. However, M16 has been shown to sub-optimally sustain *in vitro* embryo development, as compared to KSOM+AA, at all stages of development. This difference in quality between the two media is magnified as cultured embryos progress to later stages of development *in vitro*. Finally, as a preliminary effort to assess the safety of OET for embryos, the survival and continued *in vitro* development of embryos following OET assay was analyzed.

3.2 Experimental Design Methodology

The embryo model used here is predicated on three key points: 1. Embryos cultured in a suboptimal medium are inherently different, less likely to survive *in vitro*, and/or result in a live birth, as compared with embryos cultured in optimized medium (KSOM+AA); 2. At any pre-implantation stage of development, embryos cultured in optimized medium can be visibly indistinguishable from embryos cultured in suboptimal medium; and 3. Clinically, embryo selection for IVF continues to be guided primarily by morphologic (visible) parameters. It is essential to review how embryo culture medium quality is defined.

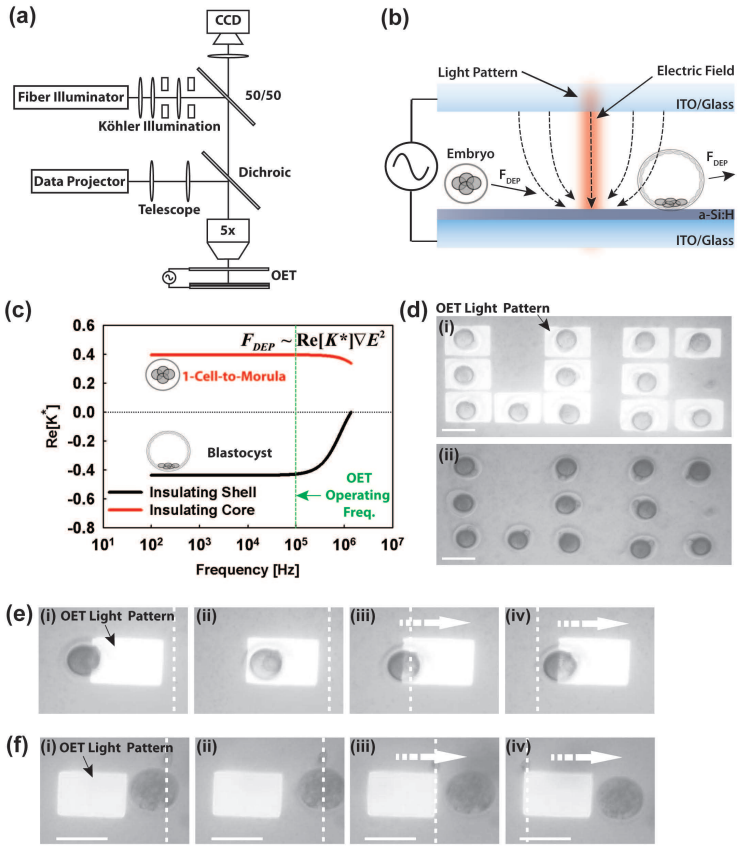

Figure 3.1: (a) Experimental Setup. Brightfield illumination and incident optical pattern are focused onto OET substrate. Electrical bias is applied to the OET chip via a function generator. Viewing occurs through a topside CCD camera. (b) Schematic of OET device operation for embryonic assessment. Incident light interacts with a photosensitive layer of a-Si:H. In conjunction with the externally applied bias, this causes the formation of electric field gradients (dotted lines) in the illuminated areas. These gradients result in a dielectrophoretic (DEP) force on embryos in the vicinity of the optical pattern. (c) Theoretical plot of Clausius-Mossetti (CM) factor for an insulating shell (blastocyst) and insulating core (1-cell-to-morula) versus frequency (Media conductivity: 10 mS/m). At the operating frequency (100 kHz), the model for the insulating shell (blastocyst) predicts a negative DEP (nDEP) response whereas it predicts a positive DEP (pDEP) response for the insulating core (1-cell-to-morula). (d) Demonstration of parallel manipulation of 1-cell embryos with optical pattern (i) and without (ii). (e) Sequence of images of a 1-cell embryo undergoing pDEP response. White dotted line indicates a stationary point on the OET chip. Embryo is spontaneously attracted to light pattern (i)-(ii). Stage is moved relative to light pattern resulting in movement of embryo (arrow) (iii)-(iv). (f) Sequence of images of a blastocyst undergoing nDEP response. White dotted line indicates a stationary point on the OET chip. Embryo is spontaneously repulsed from light pattern (i)-(ii). Stage is moved relative to light pattern resulting in movement of embryo (arrow) (iii)-(iv). Scale bar 100 μm.

In 1993, Lawitts and Biggers reported the formulation for KSOM medium. Beginning with a base-medium comprised of elements known to be necessary for embryo survival *in vitro*, they used a novel algorithm called sequential simplex optimization to identify what additional components, and at what relative concentrations, are necessary to allow *in vitro* developed embryos to match *in vivo* developed embryos, with respect to established viability parameters [76–78]. This formulation was later modified by Ho, Schultz *et. al.* to KSOM+AA, after showing that the addition of select amino acids consistently improved *in vitro* embryo development to the late blastocyst stage [76, 77]. Reverse-transcription polymerase chain assay studies have shown that culture in KSOM+AA results in housekeeping-gene and apoptosis-regulation gene expression that approximates expression in-vivo [77].

M16 medium is deficient in several compounds that previous work has shown are necessary to sustain optimum *in vitro* embryo development [76,77,79], and renders most out-bred mouse strain embryos subject to 2-cell block [76]. Furthermore, compared with control (*in utero* developed) embryos, a significantly smaller number of embryos cultured in M16 develop to reach the blastocyst stage. Of those that do, development takes place at a slower rate and with a lower number of inner cell mass cells [80]. More recently, Kamjoo *et. al* showed that beginning at the early blastocyst stage, embryos cultured in M16 displayed significantly fewer inner cell mass cells, and greater apoptosis, as compared with embryos cultured in KSOM+AA [81]. Hardy *et. al* showed that when the developmental rate for embryos cultured in M16 and KSOM is compared, the relative difference in rate steadily widens between the 1-cell and early blastocyst stages [80].

The prevailing view is that blocks in development observed *in vitro* are most likely caused by adverse culture conditions, such as constituent absence or imbalanced concentrations [82], and, that adverse culture conditions result in sub-optimal embryo development due to either impaired transmission of maternal genetic genes and/or gene-expression [83], or defective activation of the embryo's genome [84]. Prior to the introduction of KSOM+AA in 1995, the effects of culture medium formulation on post-transfer outcomes were rarely analyzed. This may be because media of this era were clearly not yet optimized to yield embryos developmentally comparable to controls (embryos developed in-vivo before transfer to a surrogate uterus). One such study, from 1970, showed that embryos cultured in a medium very similar to M16 (modified Brinster's Medium), resulted in pre- and post-transfer embryo quality, and live birth rates, which were significantly inferior compared with control embryos [85]. Shultz *et. al* have shown that in pups resulting from *in vitro* culture (as compared with in-vivo controls), culture medium can result in significant long-term alterations in behavior (e.g. anxiety, locomotor activity, and spatial memory) [86]. M16 remains commercially available today, but its use is limited to short-term culture at the 1 and 2 cell stages.

Given that KSOM+AA is the standard media used for most *in vitro* mouse embryo models, it was a clear choice for the "higher quality" media used in this study. As discussed, M16 is well documented to be inferior to KSOM+AA even though it has been widely used and reported on in the past. As a result, M16 was chosen as the "poor" quality media in this study.

3.3 Experimental Results

A total of 410 zygotes were harvested at the 1-cell stage and were divided equally into groups cultured in KSOM+AA and M16 medium. At the stages shown in Fig. 3.2a, cohorts of 29-43 embryos were taken from their respective culture medium, suspended in a low conductivity media (EP), and underwent OET assay (As defined in the Appendix B). The number of hours post fertilization that the embryo cohorts were assayed at each developmental group is tabulated in Fig. 3.2a. M16 cultured embryos generally required 6-12 hours of additional time in culture to reach equivalent late developmental stages, as embryos cultured in KSOM+AA. Maximum induced velocity (which is directly proportional to DEP force and, thus, the CM factor) was measured, using the manner described in Methods (See also, Video S1). Results are shown in Figs. 3.2b and 3.2c. All embryos from both the KSOM+AA and M16 groups assayed at the 1-cell, 2-cell, and 4-16 cell/morula stages exhibited a positive DEP response (pDEP) to the assay OET field (attraction to the light pattern). Among early blastocysts, the majority of embryos cultured in either media exhibited a negative DEP (nDEP) response (i.e. repulsion from the light pattern). All late blastocyst and hatching embryos cultured in either medium also showed an nDEP response. Late blastocysts, and in particular, those that were partially hatched, were generally too adherent to the OET substrate to allow them to be moved long distances by the OET field. Thus, a reliable maximum OET-induced velocity could not be calculated for these groups, and they were excluded from further analysis.

3.3.1 DEP Response of Pre-implantation Mouse Embryos

Several trends are evident from the velocity data collected at each stage. For KSOM+AA embryos, the mean maximum induced velocity significantly decreased (became less positive) between each successive stage of development ($p < 0.006$). Likewise, for M16 embryos, the mean maximum induced velocity also decreased significantly ($p < 0.0001$) at each successive stage of development. Second, there were significant differences in mean OET-induced velocity between comparable KSOM+AA and M16 matched-pair groups. Among matched cohorts (morphologically indistinguishable embryos grown in either KSOM+AA or M16) at the 1-cell, 2-cell, and early blastocysts stages, those cultured in KSOM+AA exhibited a significantly less positive/more negative response to OET as compared to those from the M16 group (Fig. 3.2b, c). The group containing a mixture of 4-16-cell stage embryos was excluded from analysis a prioi due to the within-group morphologic heterogeneity. While induced velocities for this group paralleled the observed downward trend across all developmental stages, mean velocity for the 4-16-cell stage did not differ significantly ($p = 0.59$) between the 2 groups (Fig. 3.2 b,c). Additionally, the variance among matched cohorts cultured in KSOM+AA and M16 and assayed at the 1-cell and 2-cell stages was not significantly different ($p = 0.67$ and $p = 0.87$, respectively). However, among embryos assayed at the 4-to-16-cell/morula and early-blastocyst stages, those cultured in KSOM+AA had significantly lower variance than matched cohorts cultured in M16 (Fig. 3.2b, $p < 0.0012$

(a)

	1 Cell	2 Cell	4-16 Cell/Morula	Early Blastocyst	Late Blastocyst
	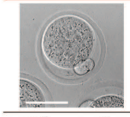	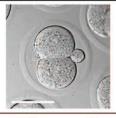	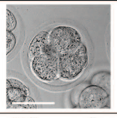	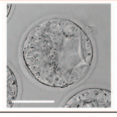	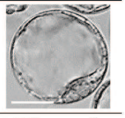
	# hrs. p.f.	*# hrs. p.f.*	*# hrs. p.f.*	*# hrs. p.f.*	*# hrs. p.f.*
KSOM	*12 (N=32)*	*36 (N=32)*	*60 (N=36)*	*84 (N=29)*	*108 (N=35)*
M16	*12 (N=32)*	*36 (N=43)*	*60-72 (N=35)*	*84-96 (N=31)*	*108-120 (N=35)*

(b)

	KSOM		M16		KSOM / M16
	$\bar{x}$	σ	$\bar{x}$	σ	*p-Value*
1 Cell	*49.4*	*5.35*	*52.7*	*4.83*	*0.00330*
2 Cell	*37.3*	*7.46*	*41.4*	*8.08*	*0.0327*
4-16 Cell	*32.5*	*3.38*	*33.4*	*5.62*	*0.594*
Early Blastocyst	*-8.28*	*6.91*	*1.94*	*13.7*	*0.0014*

(c)

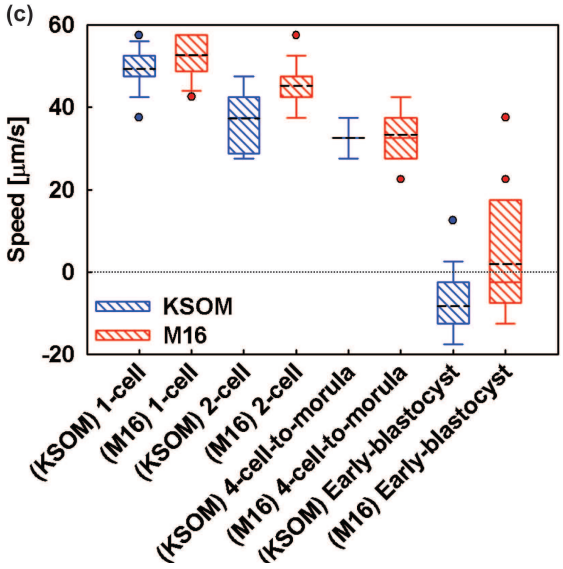

Figure 3.2: (a) Summary of experimental groups showing representative images (4-16-cell/morula group shows only an 8-cell embryo), average number of hours post-fertilization (p.f.) each group was assayed at and cohort sizes (N). Scale bar 50 μm. (b) Table summarizing the mean and standard deviation of embryo velocities in both medias (all units are $\mu m/s$) as well as the p-Value between the two distributions. (c) Box plot showing maximum induced velocity in the OET device as a function of embryonic morphology (1-cell, 2-cell, 4-to-16-cell/morula, early blastocyst) and growth medium (KSOM+AA, M16). Black dotted line indicates mean. Note the transition from pDEP to nDEP as the embryos progress from the 1-cell stage to early blastocysts. Additionally, at all stages, except the 4-to-16-cell/morula stage, KSOM embryos exhibit a significantly less positive speed.

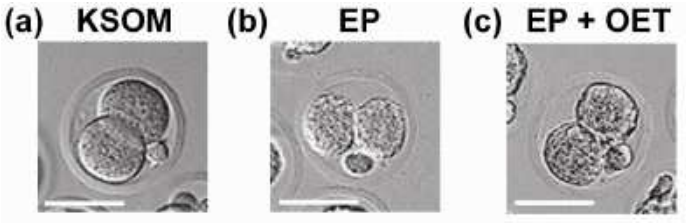

Figure 3.3: Representative pictures of 2-cell embryos after culture in KSOM (a), exposure to EP medium for 30 minutes (b), and assessment in OET while in EP medium (c). Scale bar 50 μm.

and $p < 0.015$, respectively).

3.3.2 Effects of OET Assay on *in vitro* Embryo Viability

Immediately after OET assay, embryos appeared slightly contracted and granular (Fig. 3.4). This effect on embryo morphology appears to be attributable to the EP medium, rather than OET assay itself (Fig. 3.3). To better understand whether potential adverse effects on the embryos due to EP and OET were reversible, embryos that underwent initial OET assay (T=0) at the 1-cell, 2-cell, 8-cell and early blastocyst stages, were recovered from the OET device, returned to incubation in KSOM+AA medium, and photographed every 24 hours thereafter. Ninety to 95% of embryos in each cohort continued to develop normally to the hatched blastocyst stage (Fig. 3.4).

To investigate the effects of long term exposure to the EP media used for OET assay, cohorts of 20 embryos cultured in KSOM+AA were assayed and extracted from the OET device at the 1-cell, 2-cell, 8-cell, and early blastocyst stages (Time, T=0 hrs.). After 24 hours, the maximum OET induced velocity for all embryos, at all stages assayed, had fallen to $< 5\ \mu m/sec$. One cohort of embryos (8-cell) also underwent repeat OET assay 5 hours after initial assay (Fig. 3.5). Four of the 20 embryos in this group appeared to have undergone additional cell division to between the 8-cell and morula stage. At this early time-point, mean OET induced velocity was significantly lower than the cohort's initial response at T=0 ($p < 0.001$) and mean variance was significantly greater than upon initial OET assay at T=0 ($p < 0.001$). Almost all embryos subjected to the EP media for $> 5\ hrs.$ underwent apoptosis and subsequent death. This clearly demonstrates that EP media is not optimized for embryo development and exposure to it during OET assay needs to be minimized.

3.3.3 Effects of OET Assay on Pup Yield

While Fig. 3.4 demonstrates that OET appears to have negligible effects on *in vitro* embryo development. The true test is to look at adverse effects on pup yield resulting from OET-related stress. To accomplish this, embryos at the blastocyst stage of development were split into two groups. The first, control, group was simply implanted into a recipient

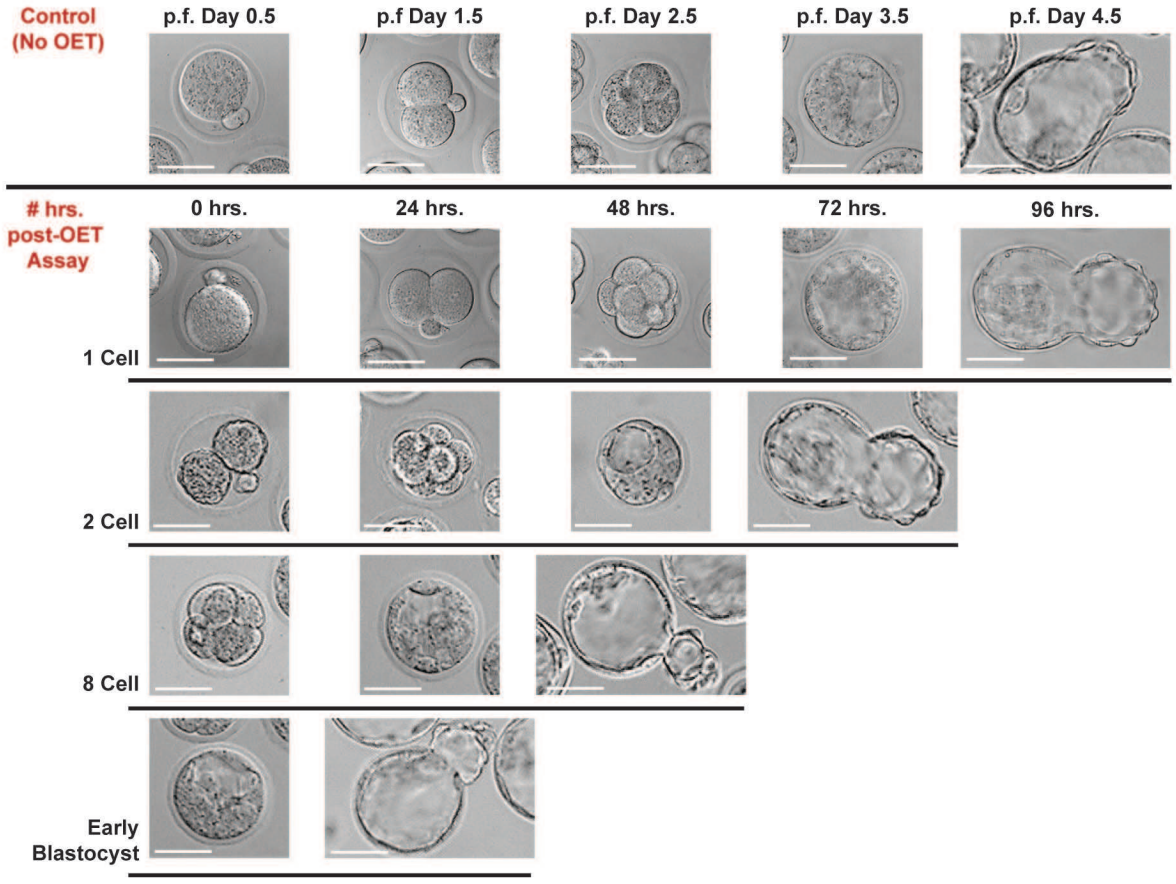

Figure 3.4: Representative pictures of embryos assayed in OET versus control group (not assayed in OET) at varying stages of development (1-cell, 2-cell, 8-cell, early blastocyst) and re-cultured in KSOM+AA media. Control group pictures are shown at 24 hour intervals post-fertilization (p.f.) starting at the 1-cell stage (p.f. Day 0.5) till the hatched blastocyst stage (p.f. Day 4.5). Post-OET Assay pictures were taken at 24 hr. intervals (following OET assay) until the embryos reached the hatched blastocyst stage. Nearly all $(90 - 95\%)$ assayed embryos, at all stages of development, progressed to the hatched phase. Scale bar 50 μm.

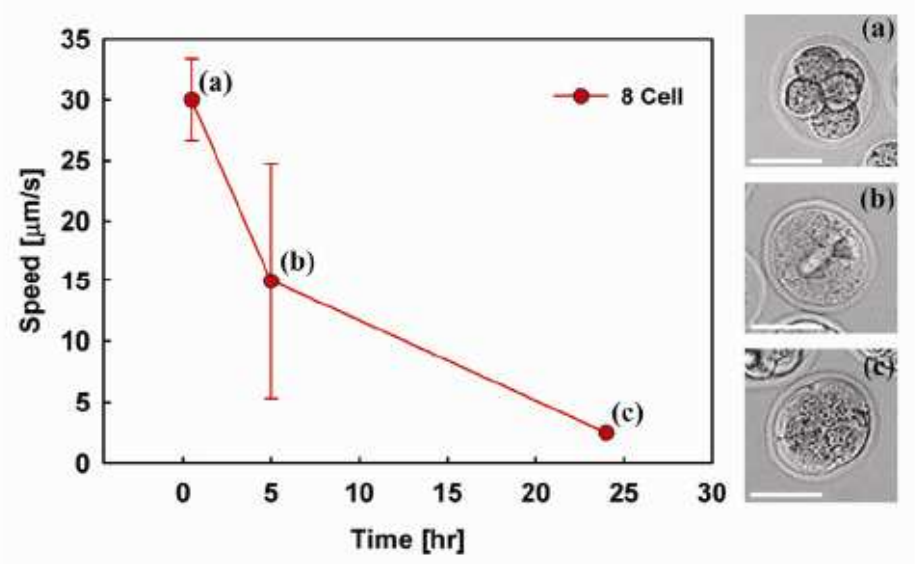

Figure 3.5: Maximum OET speed of 8-cell embryos and pictures after placement in EP media at 0 hrs. (a), 5 hrs. (b), and 24 hrs. (c). Cells within embryos undergo apoptosis after 5 hrs. and speed decreases monotonically to zero as time of incubation increases. Scale bar 50 μm.

mother (15 embryos per recipient). The second, experimental group, was placed (in groups of 15 embryos) into the OET media and device. The embryos in the OET device were then illuminated with light from the projector and the standard 20 Vppk, 100 kHz bias was applied for 2 minutes. Following this, the embryos were extracted from the device, placed in normal media and subsequently implanted into a recipient mother (15 embryos per recipient). This serves to simulate the conditions (and subsequent stress, if any) the embryos would experience during OET assay.

After a three-week gestation period, the resulting pups from both the control and experimental groups were tallied. At day of life (DOL) 4, the weights of all the pups were also measured. The results are shown in Fig. 3.6. In the control group, 36% of all implanted embryos resulted in live births versus 47% in the experimental (OET-stressed) group. Additionally, the average DOL 4 pup weight was 3.69 g and 3.35 g for the control and experimental groups, respectively. Both of these parameters show no statistical difference (p <0.05) between the control and experimental group. Therefore, this serves as a promising corollary to the *in vitro* work indicating that OET assay has little detrimental effect on embryo (and resulting pup) development.

3.3.4 Parallel Manipulation of Embryos

Finally, to demonstrate the ease of parallel assessment/control of embryos using OET, a small cohort of 12 embryos cultured in KSOM+AA were retrieved from media at the 1-cell

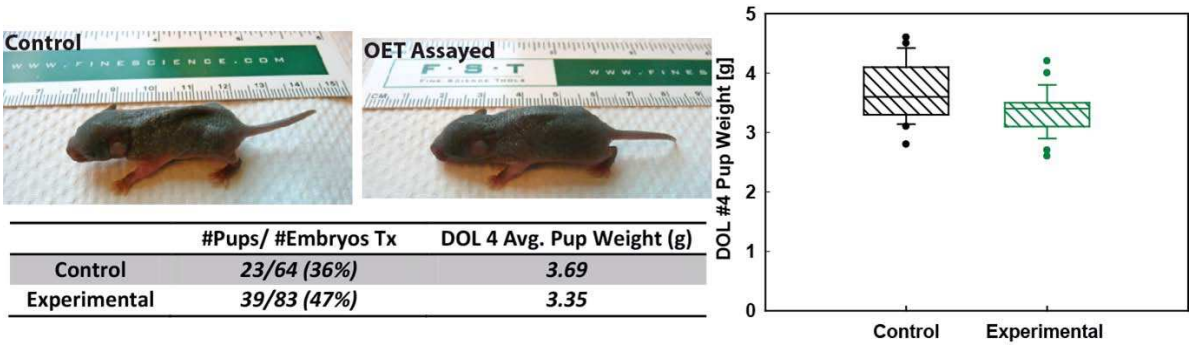

	#Pups/ #Embryos Tx	DOL 4 Avg. Pup Weight (g)
Control	*23/64 (36%)*	*3.69*
Experimental	*39/83 (47%)*	*3.35*

Figure 3.6: Clockwise from bottom left. Tabulation of live birth rate and DOL 4 average weight for both control and experimental (OET-stressed) groups. Sample pictures of pups from both control and experimental groups. Box plot of DOL 4 pup weight for both groups. There is no statistical difference (p <0.05) between the control and experimental groups for both pup yield and weight.

stage and underwent parallel OET manipulation to form the 2 letters "U" and "C" within the sorting chamber (Fig. 3.1d). All embryos responded positively to OET, and each was manipulated as shown in Fig. 3.1e. Multiple light patterns (1 per embryo) were used to independently manipulate each embryo. After positioning each embryo, its associated light pattern could be left on (Fig. 3.1d.i), or, turned off (Fig. 3.1d.ii), as desired. Each embryo remained in place after the OET-induced DEP trap was turned off.

3.3.5 Discussion

The observed progression from pDEP toward nDEP is likely due to changes in the electrical admittances of the developing embryo. At earlier stages of development (1-cell through 4-to-16-cell/morula), the embryo possesses a greater electrical admittance, relative to the surrounding medium. This is likely due to the highly conductive space between the zona pellucida and interiorly-located embryonic cells. This results in a positive CM factor, and, therefore, a pDEP response. However, starting at the early-blastocyst stage, the admittance of the embryos becomes smaller than that of the media, resulting in a negative valued CM factor, and, thus, an nDEP response. This is likely due to the formation of the trophoectoderm epithelium which electrically screens the highly conductive interior (blastocoele). Furthermore, as the embryo progresses from an early-stage to late-stage blastocyst, the trophectoderm's admittance decreases, resulting in an even larger nDEP response. This decrease (1000x) in admittance at the blastocyst stage has been confirmed by Benos *et. al* [74].

Given that OET can quantitatively distinguish embryos based on morphology, we hypothesized that the sensitivity of OET to detect such morphologic differences may be greater than current standard (purely observational) techniques. To assess this, the OET response of embryos cultured in either optimized culture medium (KSOM+AA) or sub-optimal medium

(M16) was analyzed. KSOM+AA is the standard medium used for *in vitro* mouse embryo culture models and has been systematically optimized over the years. M16, an "historic" medium formulation first reported in 1971, is deficient in several compounds that previous work has shown are necessary to sustain optimum *in vitro* embryo development [76]. Because cohorts were matched for morphologic parameters and differed only with respect to which medium each was cultured in, any difference in embryo response to OET is likely attributed to developmental effects resulting from the culture medium.

We observed that, beginning as early as the 1-cell stage, mean OET response among embryos cultured in M16 was consistently and significantly different ($p < 0.05$) than for matched cohorts cultured in KSOM+AA (Fig. 3.2b,c). Only the 4-16-cell cohort showed no significant difference, but, as mentioned, these groups contained subgroups of unequal numbers of embryos of varying morphology, and thus, these groups were not strictly comparable to one another.

If, as Biggers suggests, embryos are forced to "adapt" to abnormal conditions to survive (i.e. culture in M16), then, within any given cohort, some will adapt better than others, resulting in a spectrum of embryo viability and developmental potential [76]. Our results support this view: within all OET assayed cohorts, a range of OET responses was observed (Fig. 3.2). It is then reasonable to expect that, between the 2 culture groups at the same developmental stage, there will be some overlap. Though mean viability/developmental competence may differ significantly, a small subset of embryos cultured in the sub-optimal medium could be expected to have developmental potential comparable to sub-average embryos from the optimized medium group. Our results are again consistent with these assumptions: despite significant differences in mean OET response among matched cohorts cultured in both media, there was reasonable overlap in the actual OET response values of embryos from both media (Fig. 3.2). Furthermore, the variance in induced velocity among KSOM+AA cultured embryos decreased slightly ($p = 0.53$) and appeared to stabilize, whereas for matched cohorts cultured in M16, variance continued to increase through the early blastocyst stage ($p << 0.0001$). The upward trend in variance for M16 suggests that the longer the embryos are forced to adapt to a sub-optimal environment, the more the differences in viability and/or development are magnified.

Finally, the low conductivity (EP) medium in which the embryos are temporarily suspended in for OET assay deserves note. First, the medium conductivity must remain constant across all experiments in order to insure consistent results as the CM factor scales with media properties. Variation in conductivity of the final suspension was minimized through serial washing steps before each assay (See Table 3.1 for individual cohort solution conductivities.).

Second, the medium conductivity used must fall in between the low and high admittance states of the developing embryos. Media conductivities outside of this range will result in either a pDEP or nDEP response regardless of embryo morphology. Therefore, it can be presumed that optimized media conductivities for different strains of embryos will be necessary in order to produce the largest dichotomy in response. In the context of these experiments, it is important that the media conductivity remain relatively constant for all

	KSOM		M16	
	$\bar{x}$	σ	$\bar{x}$	σ
1 Cell	*19.4*	*0.05*	*19.8*	*<0.01*
2 Cell	*20.3*	*1.38*	*18.5*	*2.09*
4 Cell to Morula	*20.7*	*0.96*	*21.4*	*0.49*
Early Blastocyst	*20.6*	*1.59*	*21.6*	*0.80*

Table 3.1: Final conductivity (mS/m) of each embryo group immediately prior to OET assay. Overall KSOM+AA, conductivity (at all stages) was $20.22 \pm 1.24\ mS/m$, and for embryos cultured in M16 (all stages) was $20.21 \pm 1.78\ mS/m$.

groups due the dependence of the DEP response on the electrical properties of the media. This sensitivity to media conductivity is most prevalent at the point where the two complex permittivities are nearly identical (i.e. where the developing embryo transitions from a pDEP response to a nDEP response). To maximize internal consistency and precision, medium conductivity must be carefully monitored. It is also important to note that only certain conductivities of media (1 mS/m - 100 mS/m) can be used in the OET device presented here due to the fact that the liquid layer is part of the electrical circuit pertaining to device operation. For higher liquid conductivities (1 S/m), a different OET device has been developed [20]. However, as above, at these high conductivities the embryos are unlikely to exhibit the large full scale range of DEP responses observed here.

Finally, the OET-compatible medium used here (EP) has not been optimized for compatibility with embryos. However, embryos which were assayed and then immediately returned to culture conditions in KSOM+AA ($<$ 30 $min.$ exposure to EP) continued to develop at a normal rate with $>$ 90% reaching the late-blastocyst/hatched stage (Fig. 3.4). The latter suggests that minimizing exposure duration of each embryo to suspension media, and, use of a more embryo-compatible suspension medium, could preclude such potentially negative effects. Additionally, embryos placed in the EP medium, subjected to OET bias, and then implanted into recipients do not show any difference in pup yield (and weight) when compared to a control. Not surprisingly though, long term exposure ($>$ 5 $hrs.$) to EP media at room temperature consistently resulted in embryo death (Fig. 3.5). Such observations are encouraging and warrant further and more rigorous studies to assess potential adverse effects on the embryos caused by OET assay.

3.4 Summary

How then could OET be used to guide embryo selection for IVF? Our results suggest that, for morphologically similar appearing embryos at any given stage, the embryo with the most negative response to OET is likeliest to be the most developmentally mature and/or viable,

and should be selected for transfer. This approach is supported by both cross-developmental-stage, and, developmental-stage-matched, cross-medium comparisons (KSOM+AA and M16 cultured embryos). To date, it has simply been assumed that inferior embryo viability indices *in vitro* predict inferior viability post-transfer. The proposed ability of OET to guide IVF embryo selection and improve outcome measures can only be validated by assessing post-transfer outcomes of embryos of mixed developmental potential selected by OET. However, the mere possibility that OET can non-invasively discriminate among embryos based on factors that cannot be seen by conventional means is exciting, and would have numerous possible applications including improved embryo selection for clinical and veterinary IVF, and, as a means to guide embryonic stem cell harvest.

Chapter 4

OET Assisted Electroporation

I saw a begger leaning on his wooden crutch,
He said to me, "You must not ask for so much."
And a pretty woman leaning in her darkened door,
She cried to me, "Hey, why not ask for more?"
- Leonard Cohen, *Bird on a Wire*, 1968.

Now that we have shown the ability of OET to analyze, and subsequently profile, a sample we will move on to the next major aspect of the generic μTAS platform. In the this chapter, we will explore how OET can be used to process or, more specifically, electroporate individual cells towards the creation of a high-throughput, high-selectivity transfection platform.

4.1 Motivation

There has been an increasing amount of interest in the past decade in creating a system capable of performing single cell based assays for a variety of applications. One interesting application involves the creation of a chip with integrated cell membrane poration functionality. The ability to introduce foreign molecules into the intra-cellular space is important in applications ranging from genetic transfection to the study of cell-to-cell signaling [87, 88].

One of the most common membrane poration methods is electroporation. Temporary permeation of the cellular membrane is achieved in electroporation by subjecting the cell to an external electric field. If the field strength is large enough, it causes a temporary depolarization of the cell's bi-lipid membrane. This results in the formation of pores which allow molecules in the extra-cellular space to pass across the otherwise impermeable membrane. These molecules pass through the pores typically by either passive diffusion or field-assisted migration. The size and number of pores is highly dependent on field strength. It is typically understood that, in order for the membrane to reseal, the pores must be nano-scopic in diameter [89]. If the pores are too large, they will not reseal resulting in cell death and/or lysis. This is referred to as irreversible electroporation and, by itself, is widely used for applications ranging from tissue removal to the removal of intracellular content such as DNA

or proteins.

There are a variety of techniques that are used to enact electroporation today and each has its respective caveats. Current commercial techniques for performing electroporation involve either the bulk [90] or individual [91] electroporation of cells. These techniques are limited by either limited selectivity (bulk) or low throughput (individual), respectively. Many of these issues stem from the fact that macroscopic instruments are being designed to interface with microscopic objects, namely cells. As a result, much work is being performed to shrink the interface to the microscale.

Prior work on creating micro-poration platforms can be divided into four categories. The first, microelectrode electroporation, is the simplest technique and allows for high throughput electroporation with improved selectivity through the use of individually addressable microelectrodes [92–94]. However, it does not achieve true single cell selectivity. Here we define single cell selectivity as the ability to selectively porate a single cell amongst a greater population of cells. The second method involves creating microstructures which physically concentrate the field across the cell of interest [95–97]. These devices can afford high throughput as well as allow for different drugs to be injected into different cells, simultaneously. However, there is no mechanism for achieving single cell selectivity from a population of cells and cells cannot be porated in-situ. Optoporation is the third option and allows for single cell poration in-situ simply by moving a focused laser beam from one cell to another [94, 98–100]. However, it is difficult to parallelize the poration as multiple expensive lasers would be necessary. Though, there is promising work in this field that reduces the required optical power by coupling to nanoparticle arrays [101]. Yet another technique employed in microfluidic devices is chemical poration [102]. Here, cells are subjected to chemical stimulus which results in membrane poration. A major caveat of this method is the variation of cytotoxicity of the poration chemical with cell type [103]. Finally, microinjection affords single cell poration, with accurate dosage control, which none of the other techniques allow for. However, this technique requires a skilled user and is, generally, low throughput [104].

Despite vast improvements in cell poration platforms, there still exists an application region which affords both high throughput electroporation with single cell selectivity. By combining the parallel manipulation capabilities of OET with a mechanism for electroporation, this niche could potentially be filled.

In this chapter, we will first present some basic theory on the physics of electroporation and then introduce a couple different device structures, based on the OET platform, which build upon some of the drawbacks of existing techniques for implementing electroporation. Namely, we will strive to demonstrate a platform with the capacity for moderate/high throughput parallel electroporation (10 to 10^6 cells), while maintaining single cell selectivity. A platform of this nature will fill the void left by current commercial techniques and alleviate many of the issues presented by the current development efforts described above.

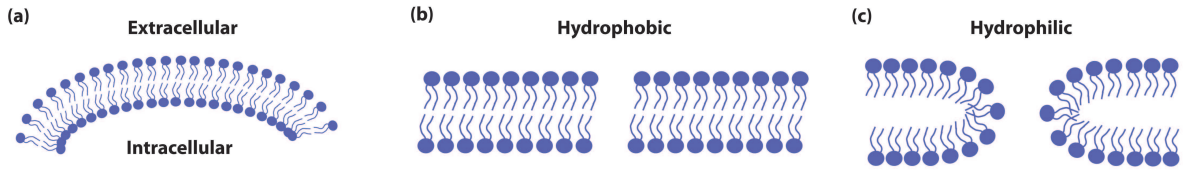

Figure 4.1: (a) Structure of lipid bilayer forming cell membrane. Membrane is composed of a bilayer of phospholipid groups forming a boundary between the intra- and extracellular space. (b) Hydrophobic pore. (c) Hydrophilic pore.

4.2 Electroporation Theory: Energetics

The theory behind the exact nature of pore formation and lifetime is not thoroughly understood. The most common theories involve modeling pore evolution as a stochastic process by which pores form and then drift and diffuse when exposed to high electric fields [105]. In this section, we will elucidate some of the basic principles underlying pore formation and lifetime using basic energetic arguments. The proceeding analysis is based on [106].

4.2.1 Membrane Pore Energy

The lipid membrane of a cell is comprised of two opposing layers of phospholipids each of which contain a hydrophilic head and two hydrophobic tails. These phospholipids arrange so that the hydrophilic heads point towards the interior and exterior of the cell while the hydrophobic tails point towards one another in order to prevent any contact with water (Fig. 4.1a), thus forming a bi-lipid membrane which isolates the interior of the cell from the external environment. Various proteins are also imbedded within the phospholipid matrix and serve a variety of functions including ionic transport and environmental sensing. Thermal fluctuations can disturb the equilibrium phospholipid matrix resulting in the creation of small pores (Fig. 4.1b). These pores are considered hydrophobic as the hydrophobic tails are exposed to the external aqueous environment. These pores are typically quite small (radius, r $\ll$ 0.5nm), non-conducting, and have lifetimes on the order of 10 ps [106].

The energy associated with these hydrophobic pores can be modeled by considering the matrix of phospholipids as one in which each phospholipid is connected to its neighbors with a simple linear spring. Therefore, for a small displacement of the phospholipid relative to its neighbors, the energy associated with this movement would be proportional to the square of the displacement. Hence, the energy of a hydrophobic pore should vary quadratically with the radius and can be expressed as:

$$U(r) = E_* \left(\frac{r}{r_*} \right)^2 \tag{4.1}$$

where r_*, E_*, and r are the maximum radius of a hydrophobic pore ($\approx 0.5nm$), energy associated with the largest hydrophobic pore ($\approx 45kT$), and radius of the actual pore,

respectively [106].

Due to the exposure of the hydrophobic tails to the extra-membrane space, the hydrophobic pore is not stable for large pore diameters. At a critical pore radius, r_*, the phospholipids will rearrange themselves to form a hydrophilic pore (Fig. 4.1c). In this vein of thought, all pores begin as hydrophobic pores and some of these which exceed a critical size become hydrophilic pores. These hydrophilic pores are typically larger ($r > 0.5nm$), conducting, and have longer lifetimes (seconds) [106]. The energy associated with a hydrophilic pore is considerable more complex than its hydrophobic counterpart. The energy can be expressed as:

$$U(r) = \beta \left(\frac{r*}{r}\right)^4 + 2\pi r\gamma - \pi r^2\sigma \tag{4.2}$$

where β is the steric repulsion coefficient, γ is the line tension, and σ is the membrane tension [106]. The first term in Eq. 4.2 is the due to the steric repulsion of the individual phospholipid heads. This places a lower bound on the size the hydrophilic pore, namely r_*. The second term refers to the line energy of the pore which is due to the fact that the lipid bilayer must be bent at along the pore perimeter, therefore the term is proportional to the pore circumference. The final term in the hydrophilic pore energy expression is due to the effects pore creation has on membrane tension. The creation of a pore reduces the membrane tension by an amount proportional to the pore area (accounting for the negative sign on the last term).

Fig. 4.2 shows a conceptual plot of the energy equations for both hydrophobic and hydrophilic pores. Many important insights into the pore formation process can be garnered here. First, the radius at which the two curves cross, r_*, is the minimum radius at which it is energetically favorable to form a hydrophilic pore. Pores below this critical radius will be hydrophobic and disappear quickly (10 ps), whereas pores larger than this radius will be hydrophilic and have much longer lifetimes. Second, there is an energy minimum,E_m ($\approx 45kT$), corresponding to pore radius r_m ($\approx 1nm$, [106]), just to the left of the hydrophobic/hydrophilic transition radius, r_*. This indicates that pores at this radius are relatively stable as they must surmount an energy barrier equal to $E_* - E_m$ ($\approx 18kT$) in order to disappear. Lastly, for pores with radii larger than a radius r_d ($\approx 20nm$, [106]) and resulting energy E_d ($\approx 277kT$, [106]), the pore energy begins to decrease, indicating it is energetically favorable for pores to become larger. This leads to membrane rupture and subsequent cell death. In the context of electroporation, this is referred to as irreversible electroporation.

Once a pore has formed, thermal fluctuations will cause pore size to spontaneously change. Additionally, as Fig. 4.2 demonstrates, there are certain pore radii which are more energetically favorable than others. This will lead to pore size drift. The drift velocity refers to the time rate of change of the pore radius and will be proportional to the derivative of Fig. 4.2.

$$v = \frac{dr}{dt} \propto \frac{\partial E}{\partial r} \tag{4.3}$$

where v is the drift velocity. This equation indicates that pores will tend to drift towards

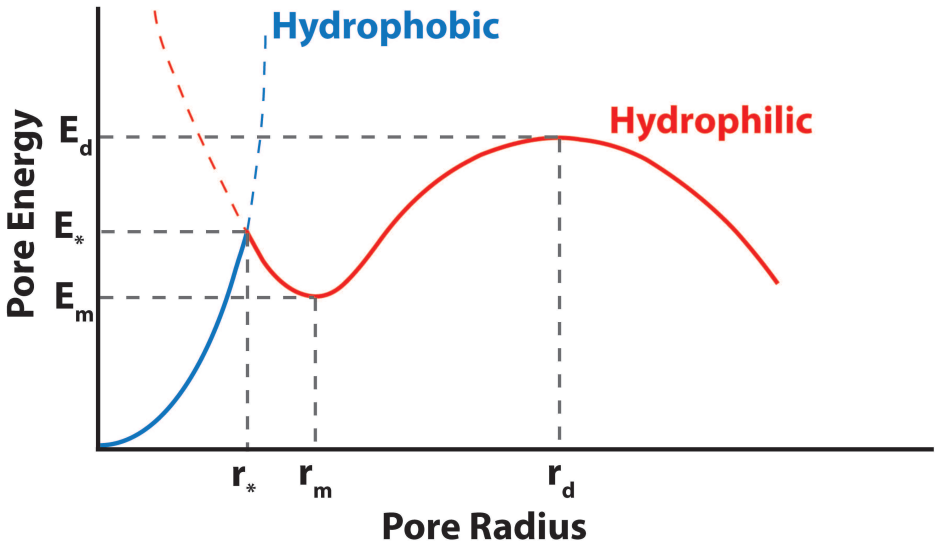

Figure 4.2: Qualitative plot showing hydrophobic (blue) and hydrophilic (red) pore energy as a function of radius. Note the dotted lines do not correspond to physically realizable pores. Hydrophilic pores become energetically favorable over hydrophobic pores at radius r_*, with a stable energy minimum at radius r_m, and for pores begin to grow uncontrolled for radii greater than r_d.

radii where the energy is at a minimum. Namely, for $r < r_*$ the pore will disappear, for $r_* < r < r_d$ the pore will trend towards r_m, and for $r > r_d$ the pore will grow until membrane rupture.

We aim to create pores which have lifetimes large enough to introduce foreign molecules (e.g. DNA) across the cell membrane. In order to get a lower bound on the lifetime require, let us assume we want a 100 bp ssDNA molecule with a diffusion constant of $D = 50\mu m^2/sec$ [107] to diffuse across a $L = 5$ nm cell membrane, we will require a time $t = L^2/D = 500ns$. This means our pore will need a lifetime $t > 500ns$. Given that the lifetime of a hydrophobic pore is only about 10ps, we must form a hydrophilic pore. However, the energy required for a hydrophobic pore to become hydrophilic, $E_* \approx 45kT$, is much greater than the ambient thermal energy, kT. Therefore, the spontaneous formation of a hydrophilic pore, and injection of the ssDNA, is highly unlikely unless we are able to to reduce this barrier. In the case of electroporation, we reduce this barrier through the application of an electric field.

4.2.2 Effects on Membrane Pore Energy Landscape through Application of an Electric Field

Now we will explore how the pore energy changes under application of an electric field (i.e. voltage). First, let's consider the hydrophobic pore. Upon application of an electric

field, a transmembrane voltage is built up. We can model this as a capacitor connected in a closed loop with a voltage source. Additionally, any hydrophobic pores in the membrane can also be modeled similarly albeit with a different capacitance (i.e. the permittivity of the pore is different than that of the membrane). Hydrophobic pores can be modeled as capacitors since they are considered to be non-conductive. When a hydrophobic pore forms, the overall energy in the system changes. The change in energy comes from two sources: the change in energy stored in the capacitor (membrane capacitor to pore capacitor) in our model and the work done by the voltage source to maintain a constant transmembrane/trans-pore potential:

$$\Delta U_{hydrophobic} = \Delta U_{cap} + \Delta U_{source} \tag{4.4}$$

where ΔU_{cap} and ΔU_{source} are the change in energy of the capacitor and voltage source, respectively. The change in capacitative energy is readily expressed as:

$$\Delta U_{cap} = 1/2 \Delta C V^2 \tag{4.5}$$

where V and ΔC are the transmembrane voltage and difference in capacitance between a membrane capacitor with radius r and a hydrophobic pore capacitor of the same area, respectively. Adopting a parallel plate model for the capacitance, ΔC is:

$$\Delta C = (\epsilon_m - \epsilon_p)\frac{\pi r^2}{t} \tag{4.6}$$

where ϵ_m, ϵ_p, and t are the permittivity of the membrane, permittivity of the pore, and thickness of the membrane/pore, respectively. Therefore,

$$\Delta U_{cap} = 1/2 \left((\epsilon_m - \epsilon_p)\frac{\pi r^2}{t} \right) V^2 \tag{4.7}$$

Remembering the passive sign convention, the amount of work, W, required to move an amount of charge ΔQ across a voltage V is equivalent to $-\Delta U_{source}$ and can be expressed as:

$$\Delta U_{source} = -W = -\Delta Q V = -\Delta C V^2 \tag{4.8}$$

$$= -\left((\epsilon_m - \epsilon_p)\frac{\pi r^2}{t} \right) V^2 \tag{4.9}$$

combining Eq. 4.4, Eq. 4.7 and Eq. 4.9 we obtain:

$$\Delta U_{hydrophobic} = -1/2 \left((\epsilon_m - \epsilon_p)\frac{\pi r^2}{t} \right) V^2 \tag{4.10}$$

Eq.4.10 shows that the application of an electric field (and subsequent buildup of a transmembrane potential V) will act to lower the overall hydrophobic pore energy given by

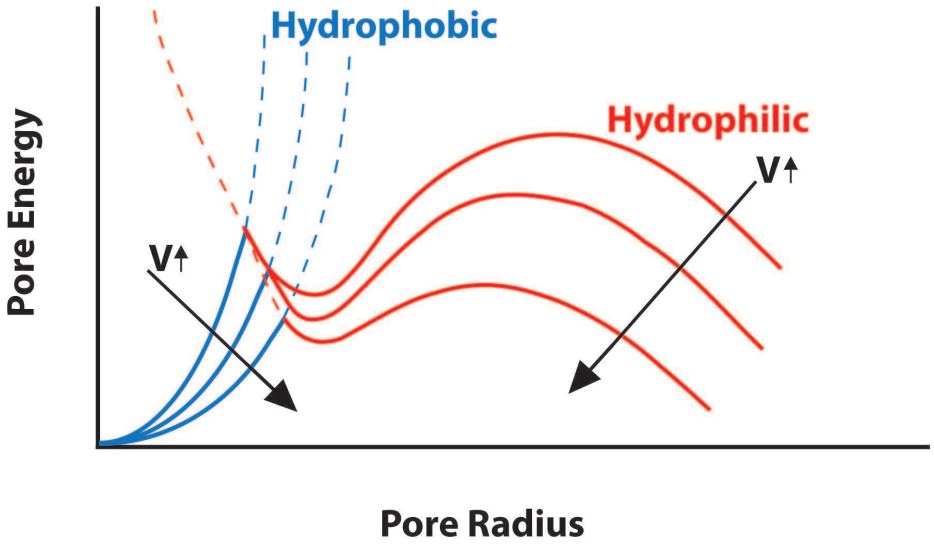

Figure 4.3: Qualitative plot showing effects of electric field on hydrophobic (blue) and hydrophilic (red) pores as a function of increasing transmembrane voltage V. Note how for increasing voltage the energy barrier for hydrophobic-to-hydrophilic pore transformation is lowered. Thus, the application of an electric field lowers the barrier to longer lasting pore formation (hydrophilic) and therefore allows time for exogenous molecules to enter the cell. Additionally, the energy barrier, E_d, and corresponding radius, r_d, also decrease for increasing voltage. This predicts irreversible electroporation for large voltages.

Eq. 4.1, as shown in Fig. 4.3. Therefore hydrophobic pores of larger radii will form more easily and, by extension, the energy barrier to create longer-lasting hydrophilic pores, E_*, is also reduced. It is also important to note that the electric field will also have an effect on the hydrophilic pores (which are now more easily nucleated from hydrophobic pores). The effect can be physically intuited by considering the fact that the hydrophilic pores are now conducting. There will now be a concentration of electric field lines at the pore as the electric field will preferentially bend towards the low impedance (relative to the rest of the membrane) pore. This will exert a stress on the pore walls which can be calculated using Maxwell stress tensors (See Fig. 4.4). This stress will act to reduce the overall pore energy for a given radius. The exact effects follow an empirically determined relationship, however, the qualitative effects are shown in Fig. 4.3. It should be noted that the energy barrier for rupture, $E_d - E_m$, is decreased and moves to smaller and smaller radii for larger and larger values of V. This means that for large values of V, it becomes energetically favorable to create larger and larger pores which will lead to membrane rupture (i.e. irreversible electroporation).

As the preceding discussion has shown, the application of an electric field lowers the energy barrier required to form the longer lasting hydrophilic pores required for introduction of exogenous material into the cell. In addition, it also promotes the formation of hydrophobic

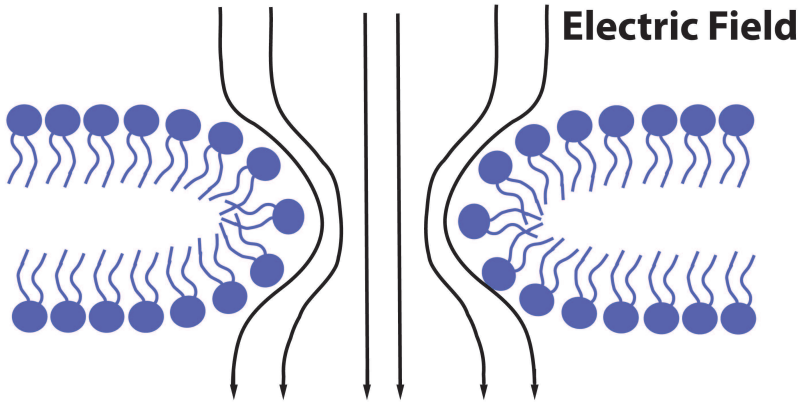

Figure 4.4: Diagram showing how existence of a conducting (hydrophilic) pore causes electric field constriction in the pore. This constriction creates a stress on the pore walls effectively decreasing the pore's energy for a given radius.

pores which are the precursors to hydrophilic pores. The model presented also predicts that for large enough voltages, it will be energetically favorable to form larger and larger pores which will eventually lead to cell membrane rupture and cell death.

In the next section, we will present two platforms which provide an ability to combine parallel, single cell manipulation with electroporation in order to create a platform capable of both moderate/high throughput electroporation while maintaining single cell selectivity. All subsequent experiments use a variant of the basic OET/OEW apparatus described in Appendix C.1.

4.3 Device Operation and Experimental Results

4.3.1 Electrode-based Electroporation

Electroporation with microelectrodes is one of the simplest techniques wherein individually addressable microelectrodes are patterned onto the device substrate and subject cells to controlled electric field doses. Since selectivity will scale with electrode number, the complexity and cost of the device increases substantially if one wants to achieve true single cell accuracy (i.e. a large number of electrodes will require multiple metal layers with a need for on-chip addressing and decoding). A more ideal approach would be to have a small number of electrodes that form electroporation sites for individual cells and then use a technique such as OET to bring the cells of interest to the electroporation sites. By combining OET's ability to select and manipulate individual cells with microelectrodes, high selectivity can be achieved with far fewer number of electrodes (Fig. 4.5).

A simple two-mask process was used to integrate the microelectrodes onto the traditional OET structure. The OET device was fabricated as described previously. The electrodes were defined via a lift-off process using a 10-nm/60-nm layer of evaporated Cr/Au. Isolation of

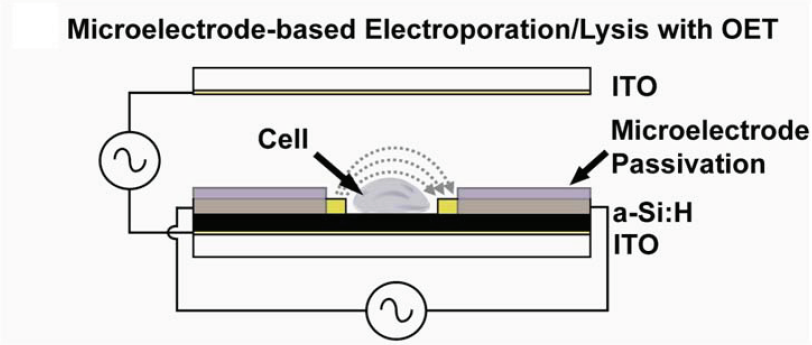

Figure 4.5: OET integrated with on-chip microelectrodes for single cell electroporation.

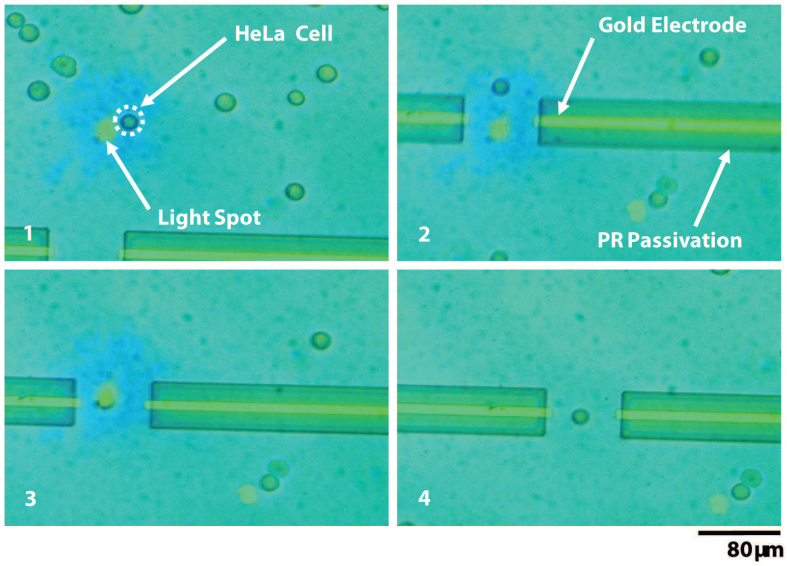

Figure 4.6: An individual HeLa cell is selected and moved with OET to the electroporation region directly between the two Au electrodes.

the electrodes was then achieved by patterning another layer of photoresist on top of the electrode leads.

In order to demonstrate the capabilities of integrating OET with the microelectrodes for single cell electroporation/lysis, we place a population of suspended cells onto the integrated device. We then select a single cell with OET and move it from the general population to the region between the two electrodes (5 Vppk, 100 kHz). This process can be seen in Fig. 4.6. One can see that in panel 4 the cell is located directly between the two Au electrodes and is awaiting the electroporation bias.

Next we apply the electroporation bias between the two gold electrode leads (6 Vppk, 3 VDC, 100 kHz, 1 msec). After the bias is applied the cell's membrane is permeated allowing

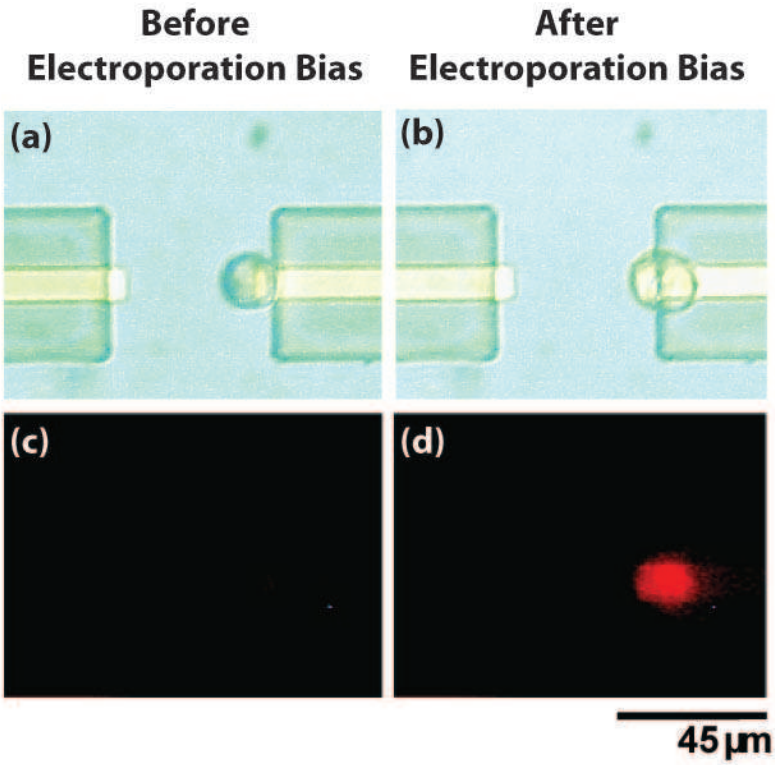

Figure 4.7: Top panels (a, b) show bright field images of the HeLa cell. Bottom panels (c, d) show the corresponding PI fluorescence images. The cell positioned via OET between the two Au electrodes is subjected to the electroporation pulse applied between the two electrodes and subsequently fluoresces red indicating successful electroporation

the PI dye to enter the cell. Fig. 4.7 shows the results of this experiment where the cell fluoresces strongly red (Fig. 4.7d) after the bias pulse is applied, demonstrating successful membrane poration. It should be noted that when the microelectrode is biased, the cell between the electrodes experiences a DEP force which causes it to be attracted to the metal electrode (Fig. 4.7b). Oftentimes, the cell is then permanently adhered to the metal surface, making subsequent movement with OET impossible. This could be eliminated by designing a physical barrier between the cell and metal electrode.

4.3.2 Light-induced Electroporation

Here we present a novel technique for the in situ electroporation of single cells in parallel. By using a photosensitive surface, patterned light creates virtual electrodes which locally concentrate the field across the cell resulting in electroporation. The device seamlessly integrates with optoelectronic tweezers [108] (OET) which creates a device capable of parallel single cell movement and electroporation. Finally, we integrate lithographically defined

microfluidic channels onto the device to allow for the delivery of various reagents to the cells of interest. In this manner, we aim to create an electroporation platform capable of parallel processing with single cell selectivity.

Background

The device consists of two main modalities wherein either light-induced electroporation can occur or light-induced manipulation can occur (optoelectronic tweezers). The two modes of operation are switched between through a change of electrical bias.

Light-induced electroporation

Electroporation requires that a cell be subjected to a high electric field (kV/cm). In order to achieve single cell selectivity, the regions of high electric field concentration must be controlled with subcellular resolution. The presented device uses patterned light to create localized high field regions dynamically and in parallel.

A schematic of the device is shown in Fig. 4.8. The device consists of two glass substrates which are both coated with a layer of the transparent conductor indium tin oxide (ITO). The bottom substrate is coated with a photosensitive film (a-Si:H). A layer of lithographically patterned SU-8 defines the channel geometry and serves as the spacer between the top and bottom substrates. The space between the two substrates is filled with a solution containing the cells of interest. An AC bias is applied between the two ITO layers. In the absence of light, most of the electric field is concentrated across the highly resistive photoconductive layer. However, upon illumination, the resistance of the photoconductive layer (in the illuminated areas) decreases by many orders of magnitude due to creation of electron-hole pairs. This causes large electric fields to exist in the liquid layer wherever the device is illuminated. Therefore, if an object, such as a cell, is illuminated, the electric field will be concentrated across it. If the field exceeds some threshold value, the cell's membrane will permeate allowing exogenous molecules to enter the cytosol. The optical power density required to operate the device is low (1 W/cm^2). This means that a standard projector can be used to illuminate the device, thus, allowing for arbitrary optical pattern generation. In this way, parallel electroporation can occur.

Optoelectronic tweezers

For OET manipulation, the device geometry is identical to that necessary for light-induced electroporation depicted in Fig. 4.8. Once again, upon illumination, a localized electric field is created in the liquid layer. This localized electric field necessarily sets up localized electric field gradients. Particles in the presence of these gradients experience a dielectrophoretic (DEP) force. Therefore, particles can be manipulated in parallel simply by changing the illumination pattern.

Finally, it should be noted that the fields experienced by the cells during OET manipulation are below the electroporation threshold. Therefore, cell membranes are not compromised during manipulation. As mentioned above, the difference in operation between the

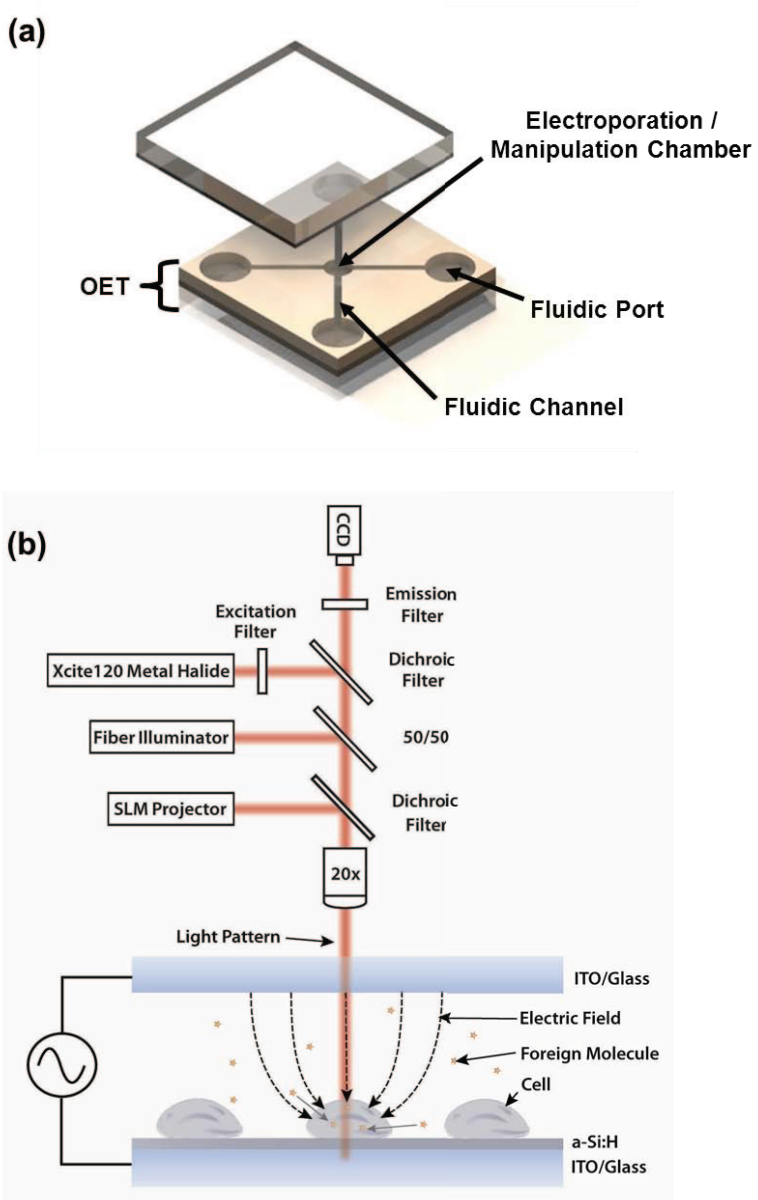

Figure 4.8: (a) Overall device layout where microfluidic channels define electroporation/manipulation areas and allow for perfusion of different reagents. OET and electroporation function are coupled through a change in device bias. (b) Cross section of device showing experimental setup and mechanism of light-induced electroporation. Optical patterns cause electric field concentration across illuminated cells resulting in selective electroporation.

OET modality and electroporation modality is a change in electrical bias. Specifically, the bias is increased for the electroporation regime relative to the manipulation regime.

Results

Cell preparation

HeLa cells at a concentration 2×10^6 $cells/ml$ were washed three times and suspended in commercially available electroporation buffer (Cytopulse Sciences, Cytoporation Media T, 10 mS/m). Propidium Iodide (PI) (Invitrogen) dye was then added to the solution at a concentration of 2 μM. Another solution containing Calcein AM (CaAM) (Invitrogen) at a concentration 6 μM in electroporation buffer was also prepared. The cell solution was then introduced into the chip via a syringe pump. The CaAM solution was introduced later using the on-chip microfluidic channels to assess cellular viability following electroporation.

Parallel single cell electroporation

In order to study electroporation, PI dye is added to the cellular solution as above. PI is a membrane impermeant dye which has low auto fluorescence. However, in the presence of DNA, the dye will bind to the nucleic acids and, as a result, fluoresce strongly red. Successfully electroporated cells will uptake the PI dye molecules and, subsequently, will develop a strong red fluorescent signature.

To demonstrate the capabilities of the OET electroporation assay we first use OET to select and array a number of individual cells. Next, we select some number of these cells (by illuminating them with the optical pattern) and increase the device bias. Unless otherwise stated, the electroporation bias is applied for 5 seconds at 100 kHz. The electroporation bias occurs at a frequency of 100 kHz because at this frequency the field in the liquid layer (which the cells experience) is maximized. This is also why DEP positioning occurs at the same frequency since the DEP force is also proportional to field strength (Fig. 4.10). It has been found that for pulse durations longer than 4 ms the amount of dye uptake in HeLa cells remains relatively constant [92]. Since we are mainly interested in studying the effects of the electric field on the cell, we kept the electroporation bias time much, much longer than this (i.e. 5 sec). This attempts to isolate the electric field as the main parameter of interest.

The applied electroporation bias causes poration of the cell membrane to occur and results in uptake of the PI dye in solution. The results of this are shown in Fig. 4.9. First, cells are manipulated into a 2x2 array (0.2 kV/cm). The accompanying fluorescent image shows no dye uptake indicating that normal OET operation does not cause membrane damage. Next, the two cells on the diagonal are illuminated and the electroporation bias is applied (1.5 kV/cm, 100 kHz, 5 $sec.$). The subsequent fluorescent image shows that only those cells that were selected are electroporated. The cells immediately adjacent to the electroporated cells are not affected by the electroporation bias. Finally, the remaining two un-electroporated cells are selected and subjected to the electroporation bias. Now, all four cells fluoresce red, indicating successful electroporation.

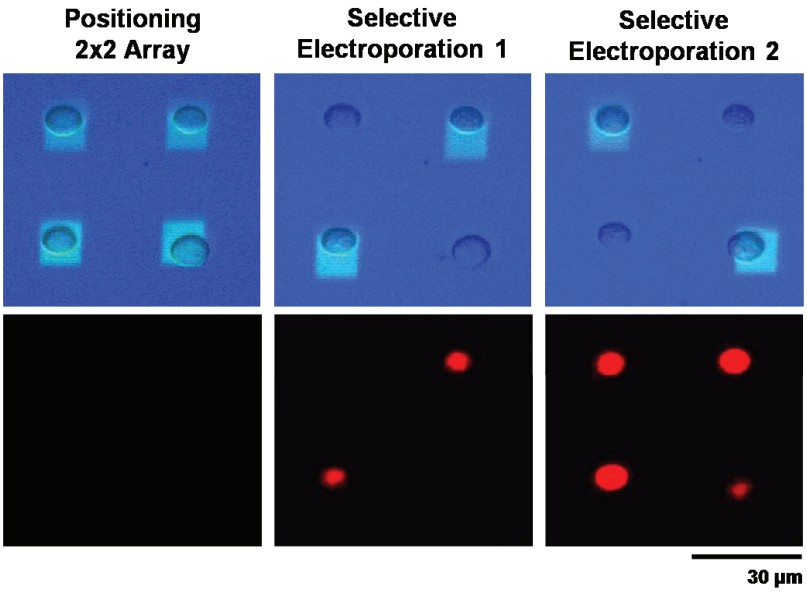

Figure 4.9: Top row shows bright field image of cells and optical pattern. Bottom row shows corresponding PI dye fluorescence. Cells are first arrayed using OET (0.2 kV/cm). OET manipulation bias does not cause electroporation. Two cells on the diagonal are then subjected to the electroporation bias (1.5 kV/cm) and, subsequently, fluoresce (image taken 5 minutes following electroporation bias). Finally, the remaining two cells are porated, resulting in the fluorescence of all cells (image taken 5 minutes following electroporation bias).

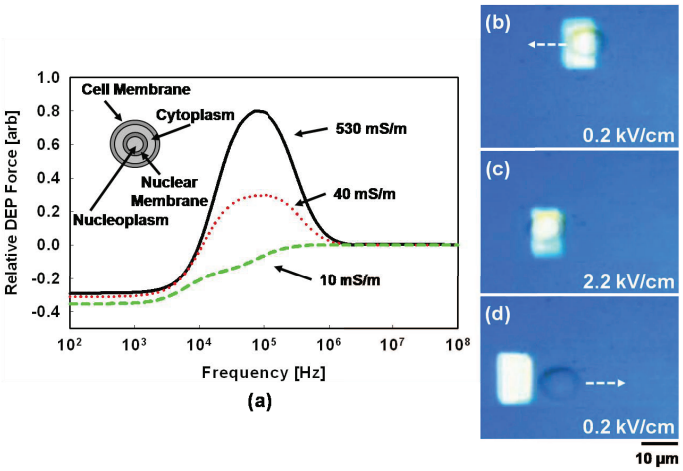

Figure 4.10: (a) Normalized DEP force in the device as a function of frequency for different cytosolic conductivities. Electroporation causes a reduction in cytosolic conductivity resulting in a varying DEP force. If the fluid exchange during electroporation is large enough, the force can switch from positive to negative. (b)-(d) Demonstration of transition from pDEP to nDEP. (b) At low bias, the cell experiences pDEP and is attracted to the light pattern. (Arrow indicates direction of movement) (c) Electroporation bias is applied resulting in fluidic exchange across membrane. (d) Upon returning to low bias (after 30 *sec.* to allow the cell membrane to reseal), the cell now experiences nDEP and is repelled from the light pattern.

DEP force Scaling

Under normal electroporation and manipulation conditions, the reported device does not cause any significant changes in the electrical characteristics of the cell. However, if the bias is substantially increased across the cell, dramatic changes in the electrical characteristics and, subsequently, the DEP response will occur. It should be noted that under these extreme operating conditions, the viability of the cells in the device is significantly decreased.

During electroporation, fluid is being exchanged across the cell membrane due to the creation of nanoscopic pores. If the fluidic exchange is substantial, it can cause a large change in the electrical characteristics of the cell. Since the effects of DEP are still present when operating the device in the electroporation regime; one would expect that the change in the electrical properties of the cell due to electroporation will also change the DEP response. The DEP force scales as described in Chapter 2:

$$\boldsymbol{F}_{DEP} \propto Re\left[\frac{\epsilon_p^* - \epsilon_m^*}{\epsilon_p^* + 2\epsilon_m^*}\right] \nabla(\boldsymbol{E}_{rms})^2 \tag{4.11}$$

where $\boldsymbol{E}_{rms}$ is the rms electric field and ϵ_p^* and ϵ_m^* are the complex conjugates of the effective permittivity of the particle and media, respectively. The complex conjugate of the permittivity is equal to $\epsilon - j\sigma/\omega$ where ϵ, σ, ω are the electrical permittivity, conductivity, and

frequency, respectively. The quantity multiplying the gradient in electrical field squared is known as the Clausius-Mossotti (CM) factor. Its value can be either positive or negative (force can be attractive or repulsive) depending on the relative electrical properties of the particle and media.

In the described device, the cells are suspended in a low conductivity media (10 mS/m). This is done to reduce the effects of joule heating due to the presence of large electric fields. This heating can reduce cellular viability. Additionally, it has been reported that the use of low conductivity media increases electroporation yield [109]. This is believed to be due to the fact that in low conductivity media (relative to that of the cytosol), the cells experience an electro-deformation force which enhances molecular uptake [110].

While the media is low conductivity, the interior (cytoplasm) of the cell is highly conducting (0.5 S/m). At the frequency of operation of the device (typically 100 kHz), this results in a CM factor of 0.8. This means that cells will be strongly attracted towards the light pattern. However, during electroporation, the outside media mixes with intracellular fluid and results in an effective lowering of the cytoplasmic conductivity. This results in a lowering of the CM factor. If enough fluid exchange occurs, the CM factor can actually switch from positive to negative in value. This means that a cell can go from being attracted to the light pattern to being repulsed from it.

A plot of the relative DEP force (in our device) versus frequency for varying cytosolic conductivities is shown in Fig. 4.10a. This figure was generated by simulating the device, as described in the previous section, in a FEM software package and extracting the resulting electric field gradients at varying frequencies. These gradients are then used to calculate the resulting DEP force. The resulting forces are then normalized to each other.

Here we use a four shell model for the effective complex permittivity of the cell using typical cellular parameters to account for the presence of the nuclear envelope and cell membrane [111]. The force approaches zero at high frequencies due to the small impedance of the photoconductive layer (at these frequencies) causing the electric field to primarily exist in the liquid and prevent effective optical switching. Notice that the relative DEP force decreases as a function of decreasing cytoplasmic conductivity. As the conductivity of the interior of the cell approaches that of the media, the force switches polarity and goes from positive DEP (pDEP) to negative DEP (nDEP) (Note that the cell membrane must remain intact for this to occur).

Certainly, if the field strength is high enough, the cell will undergo lysis. However, if the cell undergoes lysis, the function of the membrane of the cell as an electrical insulator will cease. This will result in the free mixing of intracellular contents with external solution. The lysed cell would be then electrically indistinguishable from the surrounding media and, thus, no DEP would occur (i.e. the CM factor is zero). This fact has been used to sort live cells from dead cells [18].

In the case presented here, a strong nDEP response is observed (the cell is actively repulsed from the light pattern, Fig. 4.10d) after excessive electrical stimulation. This means that the conductivity of the membrane is quite low (i.e. the cell continues to act like an insulating shell, with the conductivity of the cytoplasm very similar to that of the media). It

is typically very difficult to achieve true cell lysis with the optical powers and electric fields reported in this paper. Therefore, we believe that the onset of nDEP in this case is a result of a decrease in the cytoplasmic conductivity to near that of the surrounding media and not a result of cell lysis.

Fig. 4.10b-d shows the evolution of a cell switching from pDEP to nDEP as a result of the applied electroporation bias. Initially, the cell experiences pDEP and is attracted to the light pattern. The electroporation bias (2.2 kV/cm) is applied and then the bias is turned off for 30 seconds to allow the cell's membrane to reseal. When the manipulation bias (0.2 kV/cm) is reapplied, the cell now experiences nDEP. As mentioned above, when subjected to these large field strengths, the cell is likely no longer viable (as we will show later) and this provides an upper limit on the fields that may be applied without harming the cell. The variation of the DEP force with electroporation may be used as a way to monitor, or study, the extent of fluid exchange that occurs within a single cell.

Cell viability

For many applications of electroporation (such as gene transfection), one requires that the pores induced in the cell membrane reseal and the cell retain its viability. This is known as reversible electroporation. In order to assess this, we use a combination of two dyes to indicate both electroporation and cell viability. As before, we porate the cells in the presence of PI to indicate successful electroporation. We then use the onboard fluidic channels to exchange the media surrounding the porated cells with new media containing a dye which indicates cell viability. The cells are held in place during media exchange using OET. The viability dye used is CaAM. This dye, initially non-fluorescent, will passively diffuse across the cell membrane. Once inside, enzymes present in the cytosol break down the CaAM molecule to produce a product that fluoresces green and is membrane impermeable. A cell which fluoresces strongly green in the presence of CaAM, has an intact membrane and the necessary enzymes to produce the fluorescent derivative. These two traits are strong indicators that the cell is still viable. Therefore, after media exchange, we expect reversibly porated cells to fluoresce both red and green.

A panel depicting the evolution of the above process is shown in Fig. 4.11. An individual cell, immersed in a solution containing PI, is selected and positioned using OET (0.2 kV/cm). Initially, both PI and CaAM fluorescence are negligible. The electroporation bias (1.5 kV/cm) is then applied to the cell, resulting in PI dye uptake. The CaAM signature is still blank at this point as no CaAM is present. Finally, the media is exchanged with CaAM-containing solution (0.1 $\mu L/min.$ (corresponding to 50 $\mu m/sec.$ linear flow speed in the inner chamber), 15 $min.$) and the cell, subsequently fluoresces green (due to CaAM) and red (due to PI dye present previously). This indicates that successful reversible electroporation has occurred.

In order to more fully understand the field dependence of the electroporation mechanism, we repeat the above process for a variety of field strengths and monitor the fluorescence intensity of both PI and CaAM dye for each cell. Fig. 4.12 shows the results of this experiment. At low electric fields, membrane poration does not occur. This results in negligible PI dye

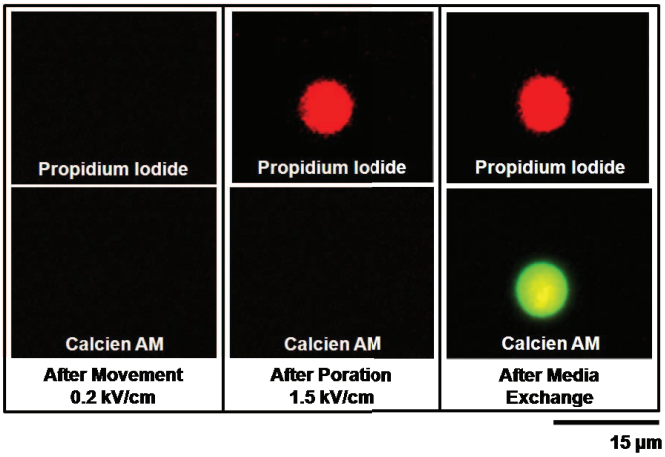

Figure 4.11: The top row shows PI fluorescence and the bottom row shows CaAM fluorescence. A single cell is suspended in a solution only containing PI (6 μM). In the first panel, no dye uptake is observed following positioning of the cell with OET (0.2 kV/cm). In the second panel, the cell is subjected to the electroporation bias (1.5 kV/cm) resulting in PI dye uptake (image taken 5 minutes following electroporation bias). In the third panel, the media is exchanged (0.1 $\mu L/min.$, 15 $min.$) using microfluidic channels with a solution containing CaAM ($2\mu M$). The cell now exhibits CaAM and PI response verifying successful reversible electroporation.

fluorescence and strong CaAM fluorescence (indicating good cellular viability). Above about 1.4 kV/cm, the cell's membrane is perforated and, as a result, PI dye fluorescence increases sharply. The CaAM fluorescence intensity initially remains unchanged from the unporated state, indicating successful reversible electroporation, until the field strength reaches approximately 2.3 kV/cm. At this point, the CaAM fluorescence drops off sharply indicating that the viability of the cells has decreased. This is most likely due to excessive fluid exchange across the membrane resulting in a diluted intra-cellular space and/or the failure of field induced pores to reseal. This simple analysis indicates that the field strengths necessary for the successful electroporation of HeLa cells for PI uptake should be in the range of 1.4-2.3 kV/cm. These values agree with those previously reported for this cell line and dye [92]. The ability to track and map an individual cell's response to field strength (versus a population) is necessary for optimizing electroporation efficacy, where efficacy relates to the ability to reliably transfer the molecule of interest into the cell and achieve a desired cellular response.

Light-induced cell transfection via electroporation

The true test of any electroporation platform is whether it can successfully insert foreign DNA into cells in a manner that causes the cell to express the protein that inserted DNA sequence codes for. This process is known as transfection. In order to evaluate whether or not the Light-induced Electroporation technique can successfully transfect cells, $\approx$ 10000 HeLa cells are suspended in 1.5μL of electroporation buffer with $10\mu g/\mu L$ Green Fluorescent

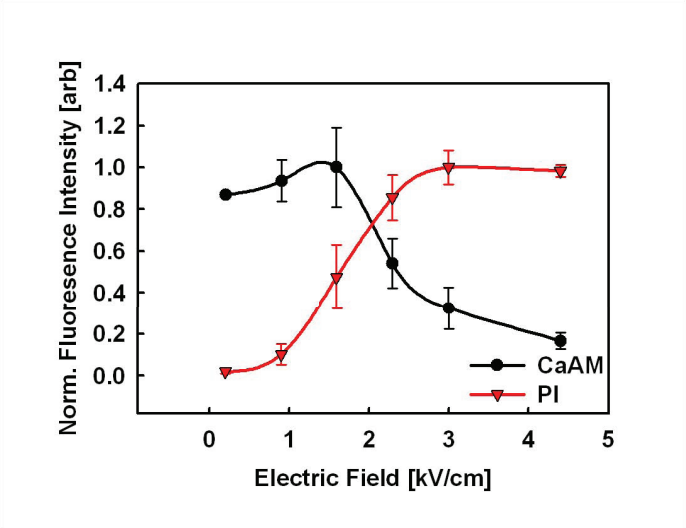

Figure 4.12: Individual HeLa cells are subjected to varying electric field strengths and the corresponding PI and CaAM fluorescence intensity is measured. Points and error bars correspond to the mean and standard deviation fluorescence intensity of 5 HeLa cells, respectively. PI dye uptake begins at field strengths of greater than about 1.4 kV/cm. CaAM dye fluorescence begins to decrease for field strengths in excess of 2.3 kV/cm. This indicates that the optimal dosage for PI dye electroporation in HeLa cells is in the range of 1.4-2.3 kV/cm.

Protein (GFP) plasmid and placed in the OET device.

Custom software is then used to raster scan the cell/GFP solution. At each field of view, cells are detected using automated image processing, a corresponding light pattern is then projected on to each identified cell, and an electroporation bias is applied. This process is depicted in Fig. 4.13. Fig. 4.14 shows the automated cell recognition and pattern generation working.

Once all cells have been subjected to the electroporation bias, the cells are removed from the OET chip and placed in a 96-well plate along with $300\mu L$ of DMEM + 10%FBS + 100:1 PenStrep and incubated at $37°C$ with 5% CO_2 for 24 hours.

Fig. 4.15a shows the dependence of normalized GFP transfection yield versus electric field for both a sinusoidal and exponentially-decaying pulse. For HeLa cells, exponentially decaying pulses is considerably more (>2x) effective for GFP transfection. Additionally, the optimal electric field for transfection is different for the two biasing schemes. For the sinusoidal pulse, the optimal field dosage is $\approx 1.9kV/cm$ while it is only $\approx 1.2kV/cm$ for exponentially-decaying pulses. This may explain why the exponentially-decaying pulse, versus the sinusoidal pulse, is more effective at transfection as the threshold for HeLa cell death (as discussed in the preceding sections)is about $2kV/cm$. Therefore, the dosage required to successfully deliver GFP via a sinusoidal pulse likely also results in cell death. Fig. 4.15b shows three representative images (bright field and fluoresence) of successfully

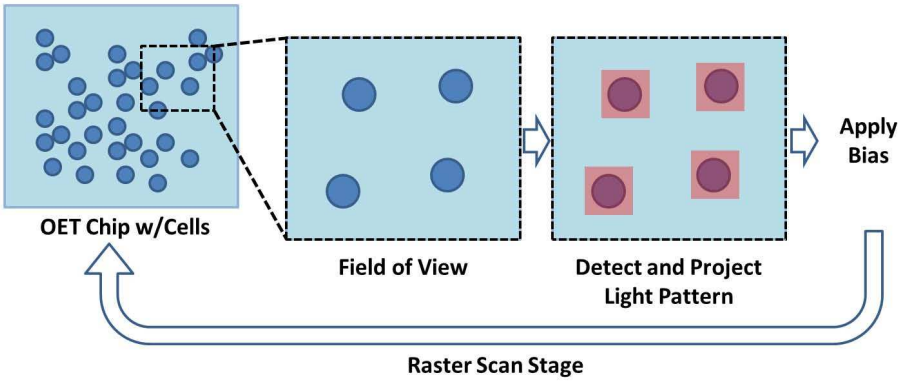

Figure 4.13: In an automated cell transfection protocol, a population of cells is rasterscanned. In each field of view, cells are identified and a custom light pattern is generated to ensure each cell is illumated. Finally, an electroporation bias is applied to transfect the cells.

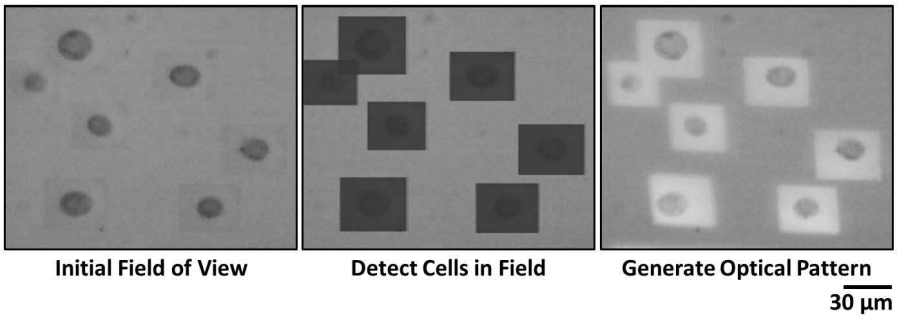

Figure 4.14: For each field of view, cells are identified using software and a custom optical pattern is generated that illuminates each individual cell prior to electroporating it.

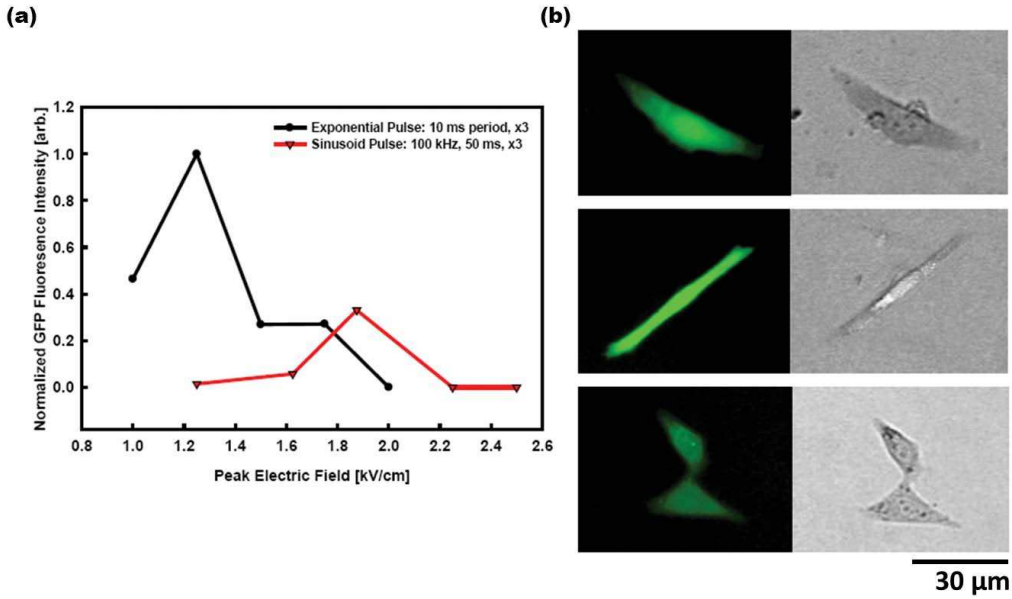

Figure 4.15: (a) Dependence of normalized HeLa cell GFP transfection yield versus electric field dosage for both sinusoidal and exponentially-decaying pulses. Exponentially-decaying pulses at 1.2 kV/cm optimize HeLa cell GFP transfection. (b) Representative bright field and, corresponding, fluorescence images of successfully GFP-transfected HeLa cells.

GFP-transfected cells.

4.4 Discussion

Each of the two devices presented here has a variety of pros and cons associated with it dependent on the user's application and requirements.

The first device, consisting of OET integrated with microelectrodes, can achieve both cell lysis and electroporation easily through use of off-chip electronics. By using OET to bring cells of interest to the electroporation/lysis site, fewer electrodes are necessary to achieve single cell resolution which reduces device complexity and cost. Additionally, since it uses OET, it affords full 2-D movement capabilities regardless of particle size. However, this device has a variety of cons. First, it requires a separate bias source for cellular stimulation and the device fabrication is more involved. Also, cells must be transported to the electrical stimulation area and cannot be porated/lysed in-situ. Additionally, upon stimulation, cells are attracted to the exposed metal (via DEP) and often become so well adhered to the electrode that subsequent movement of the cell is difficult. This is a major issue for applications involving electroporation where the cell must be later extracted for culturing/analysis. This issue can be combated by altering electrode/cell interface by introducing barriers between

the cell and electrode. Lastly, due to the fact that this technique uses OET, the top substrate must be conductive and this makes integration with on-board fluidics for extraction of lysed material/cells more difficult. However, a basic process has been developed to integrate channels on to the traditional OET device involving the lithographic patterning of SU-8 to define channel sidewalls on the OET bottom substrate and subsequent bonding of the top substrate using a UV-curable epoxy. This process allows one to use arbitrary top and bottom substrates, however it is considerably more complex than traditional methods (e.g. PDMS-based).

The second device involves the use of conventional OET to cause the electroporation of cells through a simple change in device bias. This device is the simplest of all three as there is no additional processing involved past the a-Si:H deposition and only one electrical bias source is needed. Also, cells can be electroporated in-situ. Additionally, full 2-D movement capability requires no special design considerations. A drawback of this approach is that the applied electroporation/lysing voltage is higher than that required by the other devices by 10x. As explained previously, this is because the electrode spacing in OET is dictated by the chamber gap which must be large enough to accommodate the cell diameter. Another issue, as discussed above, is that integration with fluidics is more involved due to the reliance on a conductive top substrate. However, as mentioned above, processes do exist for the integration of channels with the OET device. Transfection has been achieved with this technique, however, the yields at this moment at low compared to traditional means. Typical transfection yields via light-induced electroporation are in the range of 5%. In order to rival traditional bulk electroporation techniques, this yield should be close to 70-80%. They is a variety of mechanisms which could contribute to this discrepancy. One of the main contributors is likely decrease in cell viability due to long-term exposure to a non-native cell culture environment. The cells must remain in the electroporation buffer, and OET chip, for at least 20 minutes in order for the entire chip to be raster scanned and each cell electroporated. During this time the cells are not only suspended in a low conductivity buffer but they are also experiencing $\approx 10\%$ of the electrical bias being applied even when they are not illuminated (this is limited by the dark conductivity of the a-Si:H photoconductor being used). Potentially this could be improved by moving to a larger field of view (smaller number of rasters and applied bias'). However, as the field of view increases the optical pattern intensity decreases. This will, in turn, decrease the illuminated a-Si:H conductivity and reduce the electric field the cells experience during electroporation. This can likely be overcome through creative use of high powered data projectors and simple optics. By the same token, by moving to a larger field of view, the number of cells electroporated at once is increased and the throughput is, subsequently, also increased.

4.5 Summary

The electroporation of cells is a widespread and important application for a variety of biological applications. Current research has tried to improve upon some of the drawbacks

of conventional techniques by harnessing the power of microfabrication and microfluidics. However, there still exists a need for an electroporation platform allowing for high throughput electroporation with single cell selectivity. To address this issue, we have presented two devices to achieve parallel, single cell electroporation with full OET manipulation capability. Each device has a variety of attributes which correspond to the user's specific needs. These simple demonstrations realize the ability to integrate OET with other technologies in pursuit of a system capable of true parallel, single cell manipulation and stimulation.

Chapter 5

A Unified Platform for Optoelectrowetting and Optoelectronic Tweezers

To carve out your place in the world of Gravity, you must make a commitment...It's a Meritocracy out here, with gravity as the auditor. Inconsistency, incompetence, and lies are all cut short by the ground. It will stop you if you can't stop yourself.

- Mark Twight, *Kiss or Kill: Confessions of a serial climber*, 2001.

With the conclusion of the previous chapter, we have shown that the light-induced electrokinetic platform is capable of both analyzing and processing a sample; the last major component we need to address is the ability of light-induced electrokinetics to purify/sort a sample. In order to do this, in this chapter we will combine the particle manipulation capabilities of OET with the droplet manipulation capabilities of OEW.

5.1 Motivation

The field of microfluidics and micro total analysis systems has seen tremendous growth in the last decade. While many had hoped for a large-scale commercialization of the technology by now, the killer application for these devices remains elusive [112]. The eventual products that manifest out of this research will likely incorporate a multitude of the features and phenomena (e.g. capillary action, electrophoresis, electroosmosis, electrowetting, dielectrophoresis, etc.) associated with the field. The integration of multiple techniques on-chip allows for a versatile and powerful microsystem for applications in the biological and chemical processing fields. In the context of this report, an interesting example involves the integration of individual droplet control (i.e. electrowetting-on-dielectric [22, 43, 113, 114] (EWOD)) along with a manipulation technique for particles within the droplets. A successful device would enable a variety of applications ranging from on-chip sample concentration/purification to

single particle encapsulation.

The concept of integrating individual droplet control along with a means of controlling the particles within those droplets is not new. In fact a variety of work exists attempting to merge these two techniques. Not surprisingly, all prior work utilizes EWOD as the means for droplet manipulation. However, the particle manipulation techniques are more diverse and include electrophoresis [113], magnetophoresis [115], dielectrophoresis (DEP) [116, 117], and optoelectronic tweezers (OET) (also known as light-induced DEP (LiDEP)) [118]. Of all the particle manipulation techniques listed, DEP (also OET) is likely the most versatile as it acts on any polarizable particle (even charge neutral ones) and the particle's response is intrinsically related it's unique impedance spectrum enabling a means for particle sorting and identification.

While all of this work takes great strides towards realizing an integrated droplet/particle manipulation system, each reported platform suffers from three distinct drawbacks. First, each reported system restricts particle movement to specific regions of the chip. This is essentially a constraint imposed by the fact that the electrodes required for droplet manipulation (EWOD) are geometrically different (read smaller) from those used for particle manipulation. Therefore, droplet and particle manipulation can only occur where EWOD-specific and particle-specific electrodes exist, respectively. This limits the number of particle manipulation sites and requires careful electrode layout for a given application. Secondly, all of these platforms require relatively complex fabrication. Namely, they require at least 1 lithographic step. This, once again, is due to the use of discrete patterned microelectrodes for droplet and particle manipulation. Finally, none of these devices enables full 2-dimensional single particle control (In fact, with the exception of the 1-dimensional single particle control afforded by Shah et al., the other techniques can only move ensembles of particles) [118]. For some applications, such as selective single particle encapsulation, the ability to select and move individual particles over an arbitrary path in the droplet is critical.

In this report, we aim to address these issues by presenting a platform that uses opto-electrowetting (OEW) [28, 29, 119] and OET [69] (chosen through a simple change in device bias) to enable droplet and particle control, respectively. This technique requires no lithographically defined microelectrodes, since electrodes are created using patterned light, and, as such, device fabrication requires only planar deposition (no lithography). Additionally, since patterned light acts to define the electrodes, particle/droplet manipulation can occur anywhere on the surface of the device and full 2-dimensional single particle control is enabled.

5.2 Device Operation

An understanding of how both OEW and OET can be achieved on the same device is depicted in Fig. 5.1. The actual device used is shown in Fig. 5.1a. Here a liquid droplet is sandwiched between a top, Teflon-coated indium-tin-oxide (ITO) electrode and a bottom ITO electrode coated with a photosensitive layer of a-Si:H, an insulating layer of Al_2O_3, and a Teflon layer.

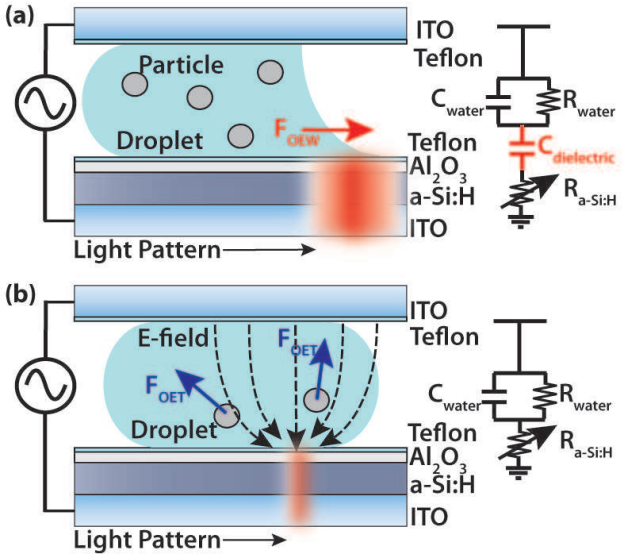

Figure 5.1: (a) Diagram of device operating in OEW modality (valid for frequencies, f ¡ 100 kHz). Incident light interacts with photoconductive a-Si:H layer and locally concentrates electric field across a thin Al_2O_3 and Teflon dielectric layer ($C_{dielectric}$). This causes aqueous droplets in the vicinity to move towards the light pattern. Particles within the droplet are transported along with the droplet. (b) Diagram of device operating in OET modality ($f > 100kHz$). In this modality, the electrically insulating Al_2O_3 and Teflon layers are shorted out ($C_{dielectric}$) and field is now concentrated in the liquid/droplet layer. Therefore, particles within the droplet experience a DEP force when in the vicinity of incident optical energy. In this regime, the device electrically looks identical to standard optoelectronic tweezers.

An external bias is then applied between the two ITO electrodes. In the absence of incident light, the electric field primarily exists in the highly-resistive a-Si:H layer. However, upon illumination, the conductivity of the a-Si:H layer increases dramatically and causes the electric field, in general, to drop across a combination of the dielectric (oxide and Teflon) and liquid layers. If the majority of the field drops across the dielectric layer, then the droplet will experience a net electromechanical force towards the illuminated region (i.e. OEW). However, if the majority of the field drops across the liquid layer, electric field gradients will exist in the liquid (due to the spatial localization of the light pattern) and exert dielectrophoretic forces on particles within the droplet (i.e. OET).

The question then becomes how one controls whether the field drops primarily across the dielectric or liquid layer. Since this is essentially just a question of which layer's impedance is larger, the answer is through the proper choice of the externally applied electrical frequency. This can be seen by comparing the equivalent device circuit diagrams of Fig. 5.1a and Fig. 5.1b. In Fig. 5.1a, a capacitor is present to model the effect of the dielectric layer. Below a critical frequency, the impedance of this capacitor will dominate over the liquid layer impedance. However, above this critical frequency, the impedance of the dielectric becomes negligible compared to the liquid resistance. Namely, the device goes from operating in in the OEW regime to the OET regime. It should be noted that electrically, Fig. 5.1b looks electrically identical to the traditional OET device (i.e. optoelectronic tweezers13).

A simplified graphical depiction of the frequency dependence of the device is shown in Fig. 5.2a. Here we schematically plot the magnitude of the impedance versus frequency. Z_d, Z_l, Z_{di}, and Z_w refer to the impedances' of the a-Si:H in the dark state, a-Si:H in the light state, dielectric, and liquid layer. For simplicity and clarity, the a-Si:H is modeled a simple resistor and the electrical double layer of the water is neglected. In order for effective switching of the voltages during illumination, the impedances of the various layers of interest must fall between the light and dark state of the a-Si:H.

In Fig. 5.2a, one can see there are three major frequencies f_{min}, f_c, and f_{max} which define the operating regions for OEW and OET. Below f_{min}, the impedance of the dielectric layer is larger than the dark impedance of the a-Si:H and, thus, no voltage switching can occur. Between f_{min} and f_c, and under illumination, the voltage will primarily drop across the dielectric layer (since its impedance is larger than that of the liquid layer) causing OEW to occur. Between f_c and f_{max}, the field now drops primarily across the liquid layer, resulting in OET. Finally, above f_{max}, the impedance of the liquid becomes so low that it drops below Z_l inhibiting effective voltage switching. With this, one can define the frequency range $\mathbf{f_{EW}}$ and $\mathbf{f_{DEP}}$, over which OEW and OET will operate, respectively, as:

$$f_{min} < \mathbf{f_{EW}} < f_c < \mathbf{f_{DEP}} < f_{max} \tag{5.1}$$

Finally, using the simple electrical circuit model in Fig. 5.1a, the device dimensions and properties given in the Materials and Methods section, and the standard constitutive equations for electrowetting [42] and dielectrophoresis [58], we can then plot the normalized force as a function of frequency. The results are shown in Fig. 5.2b. One can clearly

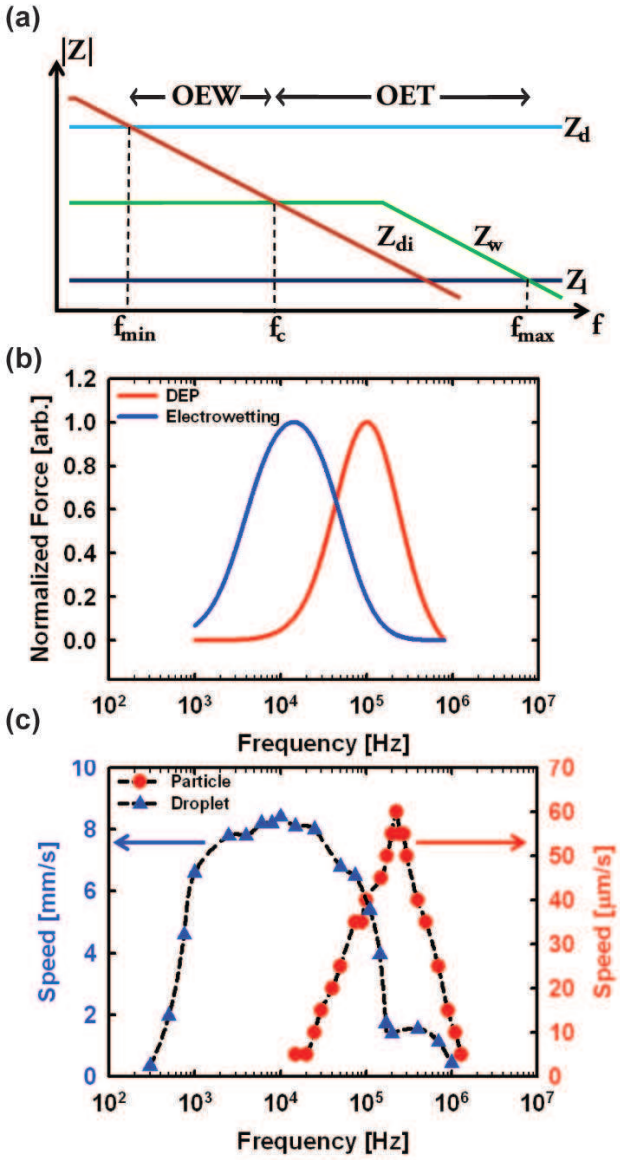

Figure 5.2: (a) Graphical depiction (not to scale) of the frequency response of device showing impedance of a-Si:H in the light (Z_l) and dark (Z_d) states as well as the impedance of the liquid (Z_w) and dielectric layers (Z_{di}). OEW occurs between f_{min} and f_c, while OET occurs between f_c and f_{max}. (b) Theoretical frequency response of the normalized electrowetting force (blue) acting on a droplet and the DEP force (red) acting on an insulating bead within the droplet. OEW force is maximized at around 10-20 kHz and OET actuation is maximized at around 100-200 kHz. (c) Experimental data showing speed (which is proportional to force) of a 12.5 nL droplet (blue, 40 Vppk (volts peak-to-peak)) and speed of a 10 μm polystyrene bead (red, 10 Vppk). The droplet movement is maximized at 10 kHz due to electrowetting, though a secondary hump is present at 200 kHz due to DEP enhancement of droplet movement. Bead speed is maximized at 200 kHz due to DEP.

see a distinct peak for electrowetting (i.e. ideal $\mathbf{f_{EW}}$) at about 10-20 kHz and one for dielectrophoresis (i.e. ideal $\mathbf{f_{DEP}}$) an order of magnitude higher at 100-200 kHz. These peaks are easily engineered simply by varying the relative thicknesses of the various device layers (e.g. oxide, a-Si:H, and/or liquid).

5.3 Materials and Methods

5.3.1 Device Fabrication

The device is depicted in Fig. 5.1a. The device consists of an ITO (300 nm) coated glass substrate, a 1 μm thick photoconductive a-Si:H layer deposited via PECVD (Oxford Plasmalab 80plus), a 100 nm film of Al_2O_3 deposited by ALD (Picosun Sunale R150) and a 25 nm film of spin coated 0.2% Teflon (3000 rpm, 30 s). The top substrate is formed from another Teflon-coated ITO glass wafer. The entire fabrication process does not require any photolithographic steps. The two substrates are then placed on top of one another separated by a spacer layer of double-sided tape (100 μm) forming the microfluidic manipulation chamber.

5.3.2 Sample Preparation

Samples are prepared by suspending 10 μm fluorescent polystyrene beads (Polysciences Inc.) or HeLa cells in a 10 mS/m isotonic aqueous solution along with 0.2% Pluronic F-68 surfactant (Sigma Aldrich). Droplets of the polystyrene or cell mixture are then deposited on the device and surrounded by silicone oil (1.0 cSt Trimethylsiloxy-terminated Polydimethylsiloxane, Gelest Inc).

5.3.3 Experimental Setup

Device bias is applied between the two ITO layers (10-40 Vppk (volts peak-to-peak), 1-500 kHz) (Agilent 33220A). Optical patterns are generated by a commercial data projector (Dell 4210X) controlled by an external computer and focused onto the device using a 1:1 telescope. Viewing occurs through a continuous zoom lens system (Navitar 12X) connected to a CCD camera (Sony XCD-X710CR). Fluorescent illumination (EXFO, XCite 120) along with appropriate filters (Chroma Technology) is also integrated into the optical train to enhance viewing of the polystyrene beads. Speed measurements for the polystyrene beads and cells are extracted using a motorized stage controller (Newport ESP300). Note this setup varies from the one described in Appendix C.1; however, in principle, these experiments can be performed on either setup. In this case, since we are looking at objects that vary in size from millimeters (droplets) to microns (particles) we decided to use an adjustable zoom lens system in order to better visualize device results.

5.4 Results and Discussion

5.4.1 Speed vs. Frequency Characterization

In order to experimentally determine the effective operating regimes of the device, a 12.5 nL, 10 mS/m aqueous droplet containing 10 μm polystyrene beads was placed in the device and the droplet's resulting maximum speed was measured as a function of frequency at 40 Vppk. Next, the speed of a 10 μm polystyrene bead (while the droplet remained stationary) was measured as a function of frequency at 10 Vppk. The resulting speeds are depicted in Fig. 5.2c. One can see that the droplet speed peaks at 8 mm/s at around 10 kHz and the bead speed peaks around 200 kHz at 60 $\mu m/s$. These results agree well with the predictions of Fig. 5.2b.

Also, it is interesting to note the additional bump in droplet speed at 200 kHz. This is likely due to DEP enhancement of the droplet movement (i.e. liquid dielectrophoresis [120]) which peaks at this same frequency (as indicated by the particle speed). It is important to note that even at 200 kHz, where particle speed is at a maximum, the droplet can still be moved (albeit slowly). This movement is likely unwanted as the droplet movement will affect the particle placement and movement. This can be prevented by selecting a light pattern that is small relative to the droplet (but still large enough to move the particles of interest), thus preventing droplet movement. Additionally, using a lower voltage for particle manipulation compared to that used for droplet movement will prevent unwanted droplet translation.

5.4.2 Particle Concentration

One potential application/benefit of having an integrated platform for droplet and particle manipulation is the ability to perform on-chip sample concentration/purification. This process is depicted in Fig. 5.3a. Here, particles are concentrated towards one end of the droplet using OET. Next, the droplet is split using OEW into two droplets, one containing the concentrated particles while the other remains empty. In this manner, the concentration/purity is effectively doubled.

Fig. 5.3b-i shows video frames of this process. Fluorescent, polystyrene beads are suspended in a 335 nL, 10 mS/m aqueous buffer. A light pattern is then swept across the droplet at 16 Vppk, 200 kHz and the beads are pushed (via negative DEP) towards the bottom of the droplet. Next, two light patterns are positioned at the top and bottom of the droplet and a 32 Vppk, 10 kHz bias is applied. This causes the droplet to split into two resulting in a concentrated droplet (Fig. 5.3h) and a diluted droplet (Fig. 5.3i).

As a means of quantitatively measuring the effectiveness of the concentration process a concentration efficiency is typically defined as [113]:

$$\text{Efficiency} = (\#\text{ of beads in concentrated droplet})/(\#\text{ of beads in original droplet}) \quad (5.2)$$

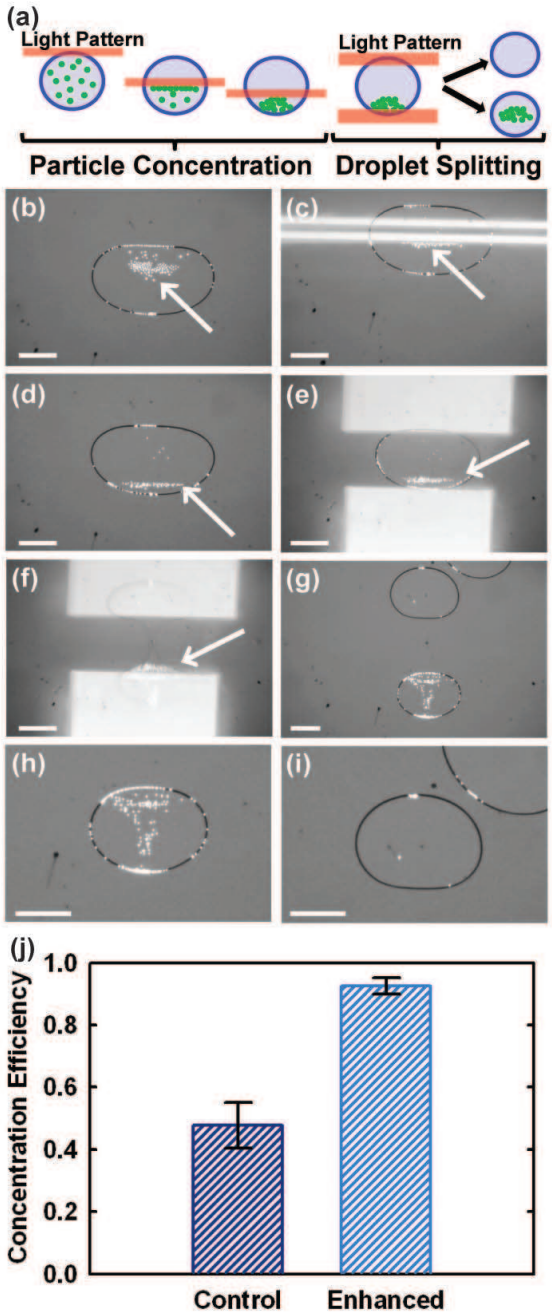

Figure 5.3: (a) Method of particle concentration. (b)-(i) Experimental demonstration of particle concentration. A 335 nL droplet containing fluorescent polystyrene beads (white arrow) is placed in the device (b). A light pattern is swept across the device (c) (16 Vppk, 200 kHz) resulting in OET on the beads and causing a concentration of beads at one end of the droplet (d). Next the droplet is split (e)-(g) using OEW (32 Vppk, 10 kHz) resulting in a concentrated (h) and diluted (i) droplet. Scale bar 750 μm. (j) Plot of the concentration efficiency for a control group (without OET) and an enhanced group (with OET). The enhanced group average efficiency is 93%.

Fig. 5.3j shows a comparison of the efficiency factors for a control group (without OET pre-concentration) and an enhanced group (with OET pre-concentration). The control group efficiency is, unsurprisingly, about 50% while the enhanced group shows an average efficiency of 93%. The remaining 7% of beads not remaining in the concentrated droplet are typically either adhered to the surface or oil-water interface and prevent efficient movement during OET pre-concentration.

It should be noted that the times required for this process are fairly slow (minutes). The constraining factor here is the rate at which the particles can be concentrated to one end of the droplet. In the case presented here, the 10 μm beads must be displaced a maximum of 2 mm (diameter of 335 nL droplet). So, at a nominal particle speed of 10 $\mu m/s$ (Fig. 5.2c), this requires more than 3 minutes. Of course, this speed can be increased by applying larger voltages, however, as discussed earlier, too large a voltage results in droplet movement as well (due to DEP of the droplet itself), which is undesirable. More realistically, the speed can be increased by increasing the optical power density on the substrate. This, in effect, creates more carriers in the a-Si:H layer and subsequently increases the field gradients/DEP force seen by the particles. In these experiments, an optical power density of $< 1\ W/cm^2$ is used. By using a higher powered projector or a more sensitive photoactive layer (e.g. phototransistor), electric field gradients can be easily increased, resulting in higher actuation speeds (100 $\mu m/s$). With this increase in speed, the concentration steps can be brought down into the 10s of seconds.

This technique could serve as an alternative to magnetic bead purification [121]. Except in this case, various types of beads (with varying electrical and, thus, DEP responses) could be functionalized. Then using the varying DEP responses, the beads with one functionalization could be sorted from others resulting in a simultaneous and/or selective purification strategy.

5.4.3 Serial Particle Concentration

A feature of this platform that is difficult to reproduce with standard microelectrode-based devices is the ability to perform serial particle concentration. This process is depicted in Fig. 5.4a. Here, like in Fig. 5.3a, particles are concentrated towards one end of the droplet and the droplet is split into a concentrated and diluted droplet. However, now one takes the concentrated droplet and repeats the process serially. Since the effective volume is reduced in half each time, the concentration will double each time resulting in an exponential increase in particle concentration as a function of the number of iterative concentrations performed. Fig. 5.4b shows the exponential increase in particle concentration for 4 iterations, resulting in a 10x concentration enhancement relative to the starting value. This process typically can continue until the resulting droplets are too small to split using OEW. This is generally dictated by the aspect ratio (droplet diameter : droplet height) of the droplet. Typically, the minimum aspect ratio at which a droplet can still be reliably split with this technique is 4:1.

The reason this is difficult to perform with existing techniques is that the lithographically defined electrode size determines the minimum droplet that can be manipulated/split.

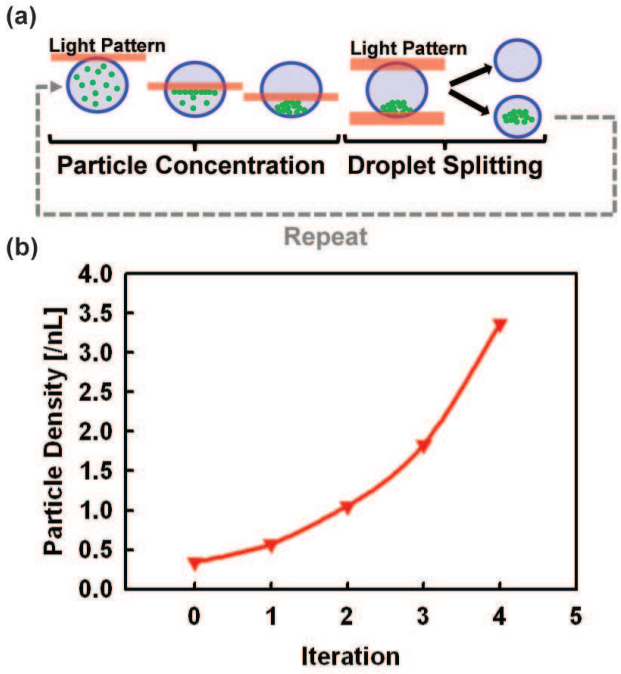

Figure 5.4: (a) Method of serial particle concentration. (b) Particle density as a function of number of times the particle concentration process of Fig. 5.3a has been performed. The particle density increases exponentially as a function of iteration number. The final particle density is 10x the original.

Therefore, since the droplet size is halved each time in this process, a large number of individually addressable electrodes are required resulting in relatively complex fabrication and addressing schemes. In this case, however, the electrode is determined by the size of the light pattern, and, therefore, smaller and smaller light patterns can be projected to account for the varying droplet diameters. Of course, the minimum projected light pattern is limited as well, and this will be the smaller of either the diffraction limit of the projected light or the diffusion length of the photoconductive material (both are typically on the order of 100 nm).

5.4.4 Single Cell Selection and Encapsulation

The ability to encapsulate single cells in micro-scale droplets is of great interest for those interested in fields such as single cell analysis and/or sorting. Traditionally, this process relies on a statistical approach which ensures that some percentage of generated droplets contain single cells and does not afford the ability to select individual cells from a population for encapsulation [122, 123]. However, work using optical tweezers has achieved the ability to encapsulate individual cells selectively [124]. But, the large optical power necessitated by optical tweezers is often detrimental to living structures [125]. Since the technique presented here requires far less optical power (10^5x) [69], cells are far less susceptible to damage.

Fig. 5.5 demonstrates the ability to select an individual HeLa cell from a cohort and then encapsulate it. The process is depicted in Fig. 5.5b-g where an individual HeLa cell is selected from a group of three. The selected cell is moved via OET (16 Vppk, 10 kHz) to one end of the droplet while the other two cells are moved towards the other end of the droplet. Note that under these conditions, the cells experience a positive DEP force here as compared to the negative DEP force experienced by the polystyrene beads. Then the droplet is split using OEW (32 Vppk, 200 kHz) resulting in one 75 nL droplet containing the selected cell (Fig. 5.5f) and one 75 nL droplet containing the remaining two cells (Fig. 5.5g). This demonstrates the ability to perform single particle manipulation continuously over the entire surface of the device and then, subsequently, encapsulate that particle. Once again, this would be very difficult to implement with non-optically-based techniques (i.e. microelectrode-based) as a large number of individually addressed electrodes would be necessary to insure single particle control.

It should be briefly mentioned that during DEP manipulation the cells are subjected to a non-zero electric field (<0.8 kV/cm in this case). This can presumably lead to unwanted cell perturbations. However, we have previously shown that cell viability is maintained under these conditions indicating that the electric field effects, in this case, are negligible 4. Additionally, the cells are placed in an isotonic buffer that has a substantially lower (100x) conductivity than that of culture media. This constrains the time the cells can be manipulated to a couple of hours while maintaining cell viability. This low conductivity buffer is required since the device will only operate over a certain range of liquid conductivities that is fundamentally controlled by the light and dark conductivities of the a-Si:H layer. We have recently developed a device capable of operating in cell culture media using a phototransistor-

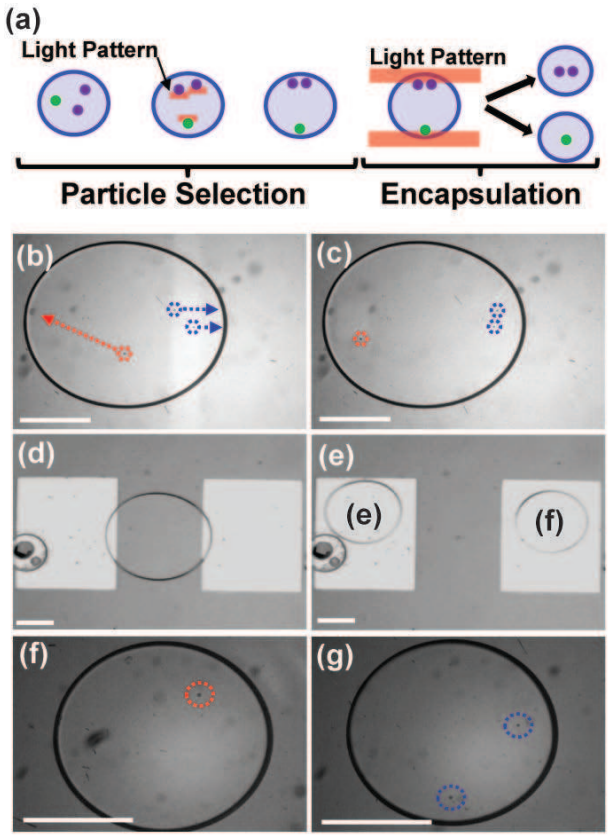

Figure 5.5: (a) Method of single cell selection and encapsulation. (b)-(c) A group of three HeLa cells are exist within a 150 nL droplet. One cell is selected (red) and moved towards one side of the droplet while the other two (blue) are moved towards the opposite side (16 Vppk, 200 kHz). (d)-(e) Next, the droplet is split with OEW into two 75 nL droplets (36 Vppk, 10kHz). The resulting droplets contain the single cell of interest (f) and the remaining two cells (g). Scale bar 500 μm.

based structure [126]. In the future, this device can be integrated with the existing droplet manipulation platform to allow for cell manipulation in a native environment.

5.5 Conclusions

A unified platform for on-chip particle and droplet manipulation is introduced. The technique uses optoelectrowetting and optoelectronic tweezers as the manipulation modalities. Switching between droplet and particle manipulation is achieved through a change in the externally applied electrical frequency. The device allows for the continuous manipulation of both droplets and particles over its surface by eliminating the need for lithographically patterned microelectrodes. As such, the fabrication process is much simplified and requires no photolithography. Finally, the use of light to pattern the electrodes enables full 2-dimensional single particle control.

Droplet and 10 μm particle speeds of up to 8 mm/s and 60 $\mu m/s$, respectively, are achieved under modest bias conditions. The ability to perform particle/sample concentration with efficiencies of 93% as well as the ability to repeat this process serially resulting in an exponentially increasing particle density and a 10x concentration enhancement. Finally, the ability to effect single cell selection and encapsulation is demonstrated.

The development of a device that allows for a seamless integration of both droplet and particle manipulation that is simultaneously low-cost, high-resolution, and reconfigurable may one day form a foundation for a multitude of applications in both biology and chemistry. With that said, we have demonstrated the final requirement of our generalized μTAS platform as depicted in Fig. 1.1.

Chapter 6

Conclusion

Just because an idea is true doesn't mean it can be proved. And just because an idea can be proved doesn't mean its true. When the experiments are done, we still have to choose what to believe.

- Jona Lehrer, *The Truth Wears Off*, *The New Yorker*, December 13, 2010.

The preceding chapters have served to illustrate the generic applicability of the light-induced electrokinetic platform, namely by the use of optoelectronic tweezers and opto-electrowetting, as applied to micro-total-analysis systems. By removing the necessity of discretely patterned electrodes and, instead, using light interacting with a continuous photosensitive film, one is able to easily effect parallel single particle and/or droplet control. In additional to pure manipulation, these platforms can realize a multitude of additional tasks. These include the ability to analyze and interrogate individual particles by measuring their dielectrophoretic response; we demonstrated this by quantitatively assessing the morphology (and, thus, developmental potential) of individual embryos. Next, we reported the ability of these platforms to process/alter a sample; specifically, through careful selection of device bias, we were able to electroporate individual cells in parallel, enabling high-throughput, high-resolution transfection. Finally, we showed, that while OET and OEW are traditionally treated as separate devices, they can be combined seamlessly to effect both particle and droplet control. With this, we demonstrated the ability to concentrate, or purify, a sample as well as sort out individual cells for single-cell encapsulation. These three results demonstrate the ability of the light-induced electrokinetic platform to achieve the three general requirements of the μTAS platform presented in Fig. 1.1.

While the embryo assessment and electroporation work was all completed on the OET device, there, at least in principle, is no major barrier to performing these functions on the integrated OEW/OET platform described in the previous chapter. This is because the embryo assessment and cell electroporation both occur at a frequency which is in the DEP operating regime of the OEW device and, thus, the OEW device should electrically look identical to OET. One possible complication would be the effect of using complex electroporation biasing waveforms which have important low frequency contributions which may be screened by the presence of the additional oxide layer in the OEW structure. Additionally,

certain analyses which require sorting/profiling based on a structure's response to varying frequencies may be impeded due to the fact that the DEP operating regime in the OEW device is limited to a smaller frequency range than in the traditional OET structure. While the DEP operating regimes can be adjusted by varying the oxide thickness in the OEW device, these are important limitations which need to be taken into account when considering application/experimental/device design.

This evidence described in this thesis suggests that the presented platform can implement, on-demand, a variety of different μTAS applications in a massively parallel fashion simply by altering the device bias and optical pattern generation. This continuous and dynamic nature suggests that the same platform can be used in a multitude of ways and removes the throughput and/or adaptability constraints imposed by more application-specific devices. The ability to program and control the biasing and optical pattern generation to fully realize this platform's potential will likely be one of the major hurdles faced next by this technology. In this case, the 'tyranny of numbers' (of discretized on-chip μTAS functions) will evolve into the 'tyranny of bits' (of computational power). But, if the last half-century is any indication of the future, Jack Kilby's 'good idea' will likely rise to meet this challenge.

Appendix A

Optoelectronic Tweezer Fabrication

A.1 a-Si:H Deposition and Characterization

The OET device used in this paper was fabricated, see Fig. A.1, on a commercially available glass substrate coated with a 300 nm layer of sputtered ITO with a sheet resistance of 10 $\Omega/square$. A 2 μm layer of a-Si:H was then deposited in an Oxford Plasmalab 80plus plasma-enhanced chemical vapor deposition (PECVD) system. The process conditions for the a-Si:H recipe were: 400 $sccm$ Ar, 100 $sccm$ $10\%SiH_4 : Ar$, at a pressure of 900 $mTorr$, a temperature of 350°C, and with an RF bias of 100 W. The a-Si:H layer thickness was chosen because at the excitation wavelength (635 nm), 90% of the incident light is absorbed within a distance of 1 to 2 μm.

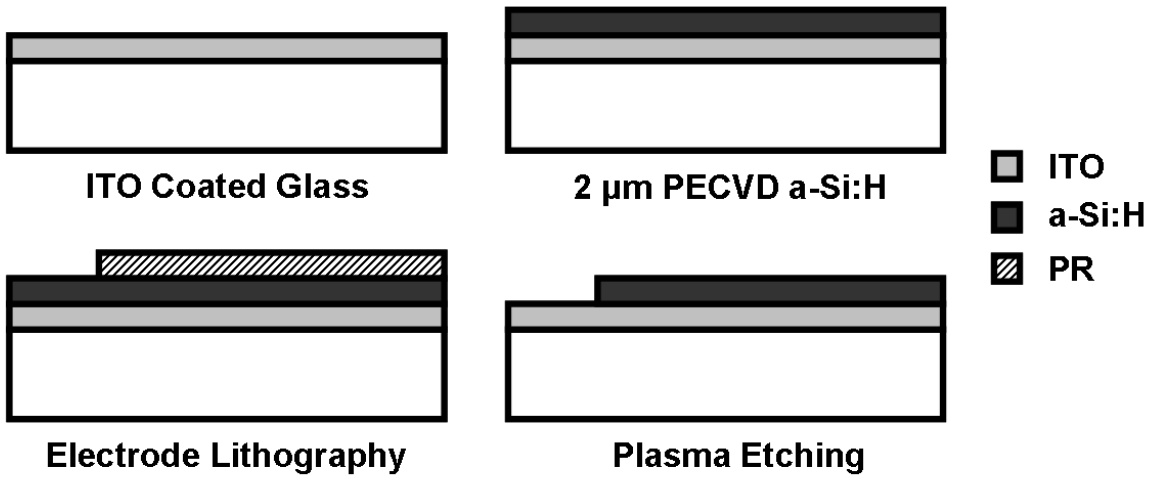

Figure A.1: The OET device fabrication begins with an Indium Tin Oxide (ITO) coated glass wafer upon which 2 μm of a-Si:H are deposited via PECVD. Next, a lithography step patterns the bottom electrode which is etched in plasma.

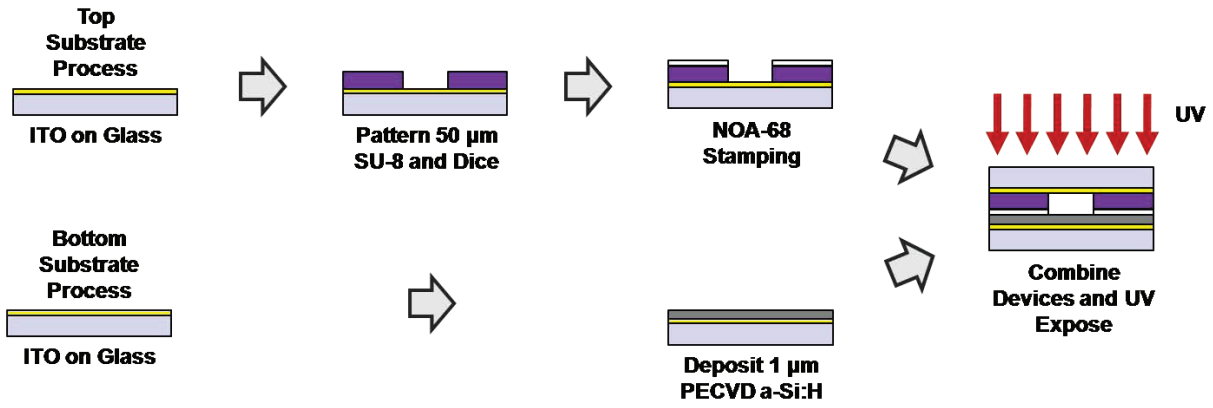

Figure A.2: Channels are defined in SU-8 on the topside OET substrate and bonded to the bottom OET substrate using a UV-curable epoxy.

Previous reported versions of the OET device have an ohmic contact layer between the ITO and a-Si as well as a thin nitride layer on top of the a-Si:H to combat stress issues. We have tuned the a-Si:H deposition to eliminate the stress and, thus, the need for the nitride layer. Additionally, the ohmic contact layer was found to be unnecessary for the operation of the OET device.

The topside device consists of another piece of ITO coated glass. The top and bottom device were separated by a 100-200 μm thick spacer of double-sided tape.

A.2 Channel Integration

The fabrication of the described device is shown in Fig. 2. The starting substrates are 6" glass wafers with a 300 nm layer of sputtered ITO (Thin Film Devices). A 1 μm layer of hydrogenated amorphous silicon (a-Si:H) is deposited via plasma-enhanced chemical vapor deposition (PECVD) on the bottom substrate (100 $sccm$ $10\%SiH_4 : Ar$, 400 $sccmAr$, 900 $mTorr$, 350°C, 200 W). The topside device is coated with a 55 μm layer of SU-8 (Microchem, SU-8 2050) and patterned to define the channel geometry. The top and bottom wafers are then diced into 2x2 cm chips with a dicing saw (ESEC 8003). Access ports are drilled into the top substrate using a diamond-coated 750 μm drill bit and drill press. Next, a UV-curable epoxy (Norland, NOA-68), is spin coated onto a dummy wafer to form a 10-20 μm layer. A block of polydimethylsiloxane is then used to transfer the uncured epoxy from the dummy wafer to the top of the SU-8 channels. The top and bottom substrates are then brought into contact (no alignment is necessary as the bottom substrate is featureless) and UV exposed using a hand-held UV gun (Norland, Opticure-4, 10 sec). Finally, fluidic interface connectors are attached to the topside device using additional UV curable epoxy. The fluidic channel layout for all devices in this paper is shown in Fig. 1a (Not to scale). All channels used in

this paper are 55 μmin height. Fluidic channels leading to the central cell chamber are 255 μm in width. The inner-circular chamber where electroporation and manipulation occurs has a diameter of 1.1 mm. The total channel length, from port to port, is 10 mm.

By allowing for arbitrary top and bottom substrates this process allows us to integrate lithographically defined microfluidic circuits with OET/electroporation functionality.

Appendix B

Embryo Work Materials and Methods

B.1 Ethics Statement

Care and handling of all experimental animals used in this work were in accordance with University of California San Francisco's institutional animal care and use committee policies.

B.2 Device Fabrication

A 6" glass wafer with a 300 nm layer of sputtered indium tin oxide (ITO) (Thin Film Devices, USA) was coated with a 1 μm layer of hydrogenated amorphous silicon (a-Si:H) deposited via plasma-enhanced chemical vapor deposition (PECVD) (100 $sccm$ 10% SiH_4 : Ar, 400 $sccmAr$, 900 $mTorr$, 350 $^{\circ}C$, 200 W). The a-Si:H coated ITO wafer, along with another 6" ITO-coated glass wafer, was then diced into 2x2 cm chips with a dicing saw (ESEC 8003) forming the bottom and top OET substrates, respectively. The bottom OET substrate (a-Si:H coated ITO) was then subjected to a brief oxygen plasma (51.1 $sccmO_2$, 300 W, 1 $min.$) and placed in a solution of 2-[Methoxy(polyethyleneoxy)propyl]trimethoxysilane (Gelest Inc., USA) for 2 hours. The immersed chips were then rinsed in ethanol and air dried. This resulted in a thin layer of poly-ethylene glycol (PEG) on the surface of the bottom substrate which aided in reducing adherence of the embryos to the surface. Electrical contacts were made to the ITO on both the top and bottom substrate using an electrically conductive silver epoxy.

B.3 OET Apparatus

A custom-built microscope (e.g. See Appendix C.1) was assembled and used for all experiments herein (Fig. 1a). The sample was placed on an XYZ micro manipulator (Newport, USA) connected to a mechanical stage drive (Newport LTA-HL and Newport ESP300-1NN111), which allowed the stage to be moved at a known rate. Viewing occurred from the

topside via a 5x objective lens. Brightfield illumination was provided via a fiber illuminator (model OSL1, Thorlabs, USA) coupled through a 50/50 beam splitter. The optical patterns used for manipulation were formed using a commercial data projector (2400MP, Dell, USA) controlled by an external computer running commercial presentation software (Powerpoint 2003, Microsoft, USA). The images were focused onto the substrate by means of a telescope and long-pass dichoric mirror. Viewing and image capture occurred via a CCD camera (model XCD-X710CR, Sony, USA) connected to an external computer. Electrical bias was applied using a standard function generator (model 33220A, Agilent, USA).

B.4 Embryo Harvest and in vitro Culture

Ovulation was induced by administering 5 IU PMS (IP) followed 48hrs later by 5 IU HCG (IP) to 20 C57BL6 x DB2 F1 3-4 week old females (Charles River Labs, Worcester, MA.). Females were mated to 5 month old Male C57Bl6 mice (Harlan Laboratories, Inc). The following morning females were checked for the presence of a copulation plug. Embryos were then harvested from the oviducts of the plugged females. The cumulus cells where digested with 300 ug/ml Hyaluronidase (Sigma H4272) in M2 medium (Milipore, Billerica, MA). A total of 410 embryos were harvested and washed with M2, divided randomly into equal groups of 100, washed with respective pre warmed, C02 equilibrated culture medium and placed in 50ul drops (33 embryos/drop) of pre warmed and C02 equilibrated medium under mineral Oil: KSOM+AA supplemented with amino acids (KSOM+AA) or M16 (Milipore, Billerica, MA.). Embryos were incubated at constant 37 C, 5%C02 (Fisher Scientific, USA). Embryo culture dishes were examined once daily beginning 8 hours from the midpoint of the dark cycle post-fertilization embryo development day (d) (d0.5), at the 1-cell stage. The above was performed on two consecutive days to have two developmental stages to evaluate on each day. The daily stages for these embryos are as follows: d1.5 (2-cell stage), d2.5 (4-cell to compacted 16-cell stage), d3.5 and d4.5 (early and late blastocyst stages, respectively). Embryos were examined and photographed under $200x$ and $800x$ microscope magnification using a Nikon Diaphot 200 Differential Interference Contrast (DIC) microscope connected to a CCD (COHU DSP 3600 Series, Poway, CA.). Embryos that failed to progress to the 2-cell stage, or appeared developmentally delayed by > 24 hours at time evaluation of were removed from the culture dish and excluded from analysis.

B.5 In vitro development in KSOM+AA and M16

Ninety-percent of embryos cultured in either medium developed to the 2-cell stage on d1.5. All embryos that failed to progress to the 2-cell stage, and any abnormal or non-viable appearing embryos were excluded from the study and removed. On the morning of d2.5, many were noted to have already progressed to the 8 and 16-cell stages. To optimize statistical power for this group, we elected to assay mixtures of equal numbers of 4-cell, 8-cell, and compacted 16-cell embryos from each group. On the mornings of d3.5 and d4.5,

approximately 70% of embryos cultured in KSOM+AA had progressed to the blastocyst stage, compared with only 35% of the M16 embryos. This difference in development rate between medium groups made it necessary to collect identical-appearing embryos from M16, for comparison to those in KSOM+AA, at a period of time 6-12 hours longer than required for the KSOM+AA group.

B.6 Embryo selection and preparation for OET assay

When, at time of primary examination (morning of p.f. days 0.5, 1.5, 2.5, 3.5 and 4.5), a minimum of 15 embryos had reached one of the given stages (1-cell, 2-cell, 4 to compacted 16-cell, early and late blastocyst), cohorts of 15-20 morphologically indistinguishable embryos were collected by aspiration micropipette and prepared for OET assay. To control for delayed maturation in either of the two media, embryos were collected only if a minimum of 15 embryos met criteria for collection (development to the target stage, with identical morphology within and across media groups for the given target stage. If fewer than 15 embryos met criteria for collection, none were collected and the entire medium-specific cohort was re-assessed every 4 hours thereafter, until a minimum of 15 embryos met criteria. Any abnormal and/or non-viable appearing embryos were excluded from the study and were removed at time of primary assessment every 24 hours.

Upon collection from medium, embryos were washed three times in Cytoporation (EP) Media T (Cytopulse Sciences, USA). EP medium is an isotonic OET-compatible buffer of minimal electric conductivity (10 mS/m). Embryo cohorts were collected in a blinded fashion, suspended in $50 - 100$ μL of EP medium, and placed onto the OET embryo sorting platform. The conductivity of the final solution containing each embryo cohort was measured. For embryos cultured in KSOM+AA, mean conductivity (at all stages) was 20.221.24 mS/m, and for embryos cultured in M16 (all stages) was 20.211.78 mS/m. Media conductivities at each stage of development for both KSOM+AA and M16 are tabulated in Table 3.1.

B.7 OET Assay

The top OET substrate of the device was placed on top of the solution containing the embryos and separated from the bottom substrate by a 200 μm spacer. The device, now containing the embryos, was placed upon the manipulation stage and electrical bias was applied (20 $Vppk$, 100 kHz).

The DEP response and maximal DEP-induced velocity was then measured by projecting a rectangular light pattern onto the substrate (Fig. 3.1). The light pattern was positioned such that the leading edge of the light pattern was coincident with the outer edge of the embryo. The stage was then translated at varying speeds to extract the maximum speed at which the embryo could be moved by the adjacent light pattern. A positive dielectrophoretic (pDEP) response was defined when the embryo was attracted towards the center of the light pattern when the light pattern was brought near the embryo (Fig. 3.1). The fastest pDEP

speed was defined as the maximum stage speed (light pattern) at which the embryo could still stay within the confines of the light pattern (i.e. the minimum speed at which the light pattern could no longer trap the embryo). pDEP speeds are annotated as a positive number. A negative dielectrophoretic (nDEP) response was recorded when the embryo was repulsed away from the edge of the light pattern when the light pattern was brought near the embryo (Fig. 3.1). The fastest nDEP speed was determined by finding the maximum stage (light pattern) speed at which the embryo could still stay outside the perimeter of the light pattern. nDEP speeds are annotated as a negative number.

B.8 OET assay of embryos subjected to varying times in EP Media

Cohorts of 20 randomly selected embryos from cohorts cultured in KSOM+AA were individually retrieved from the OET device immediately following assay at the 1-cell, 2-cell, 4-cell/morula, and early blastocyst stages (time, $T = 0\ hrs.$). Each cohort was left in EP medium, at room temperature, for 24 *hours* ($T = 24\ hrs.$), and thereafter, each was photographed (800X microscopy) and underwent repeat OET assay. An 8-cell group was also assayed at the 5 hr. mark (Fig. 3.5).

B.9 Embryo survival and development in culture after OET assay

Twenty randomly selected embryos from each cohort cultured in KSOM+AA were extracted from the OET device after OET assay at the 1-cell, 2-cell, 8-cell, and early blastocyst stages. These were re-suspended in KSOM+AA and returned to incubation conditions. The embryos were then observed and photographed ($800x$) at 24 *hour* intervals over 1-4 days (until the hatched blastocyst stage was reached) to assess the effects of OET on viability and development (Fig. 3.4).

B.10 Medium Conductivity

The conductivity of the EP medium in which all batches of embryos were suspended during OET assay was measured (immediately before assay) using a hand-held conductivity meter (model B-173, Horiba, Japan).

B.11 Statistical Analysis

All calculations were performed using the STATA 10 (College Station, TX.) statistical analysis software package. To test the difference in mean velocities, a two-sample Wilcoxon

Rank-Sum test was performed. To test the difference in variance among groups, Levene's robust test for equality of variance was used.

Appendix C

Experimental Setup Parts List

The spreadsheet on in Table C.1 lists all parts used to create a basic OET/OEW platform. Prices are as of 06/2010. The prescribed setup uses a 10x objective with an additional fluorescent beam line for fluorescent microscopy. Fluorescent filters are not included. A picture of the constructed setup is shown in Fig. C.1 and a schematic of the optical train is shown in Fig. C.2.

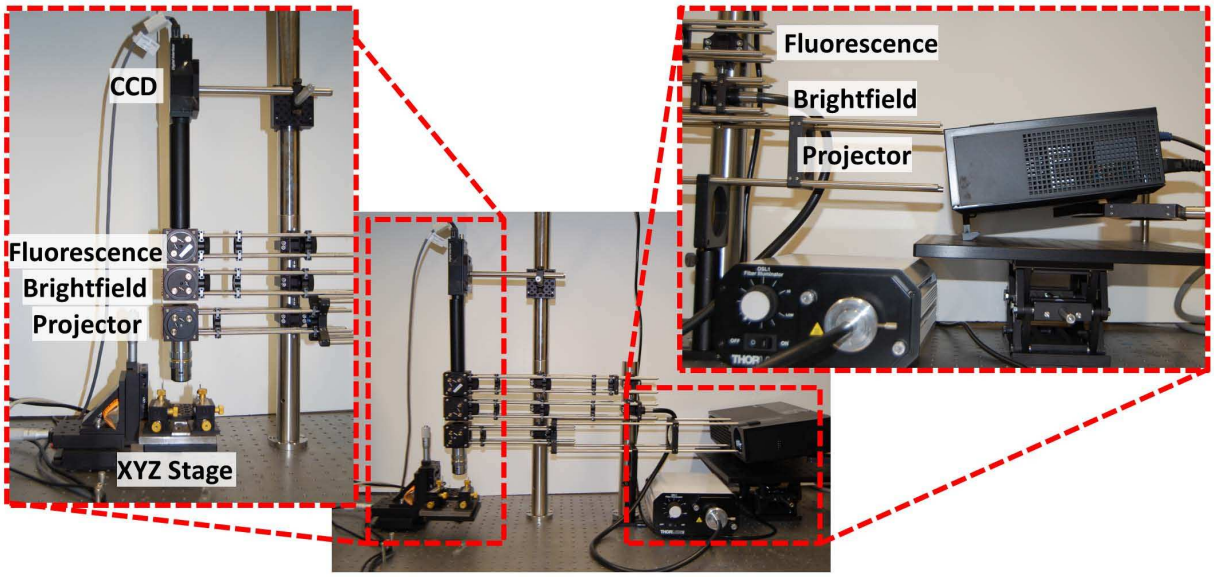

Figure C.1: Photograph of OET experimental setup constructed with parts listed in Table C.1. Setup contains an optical train for the projector, brightfield illumination and fluorescence illumination. Viewing occurs through a 10x objective connected to a CCD camera. The sample sits on an XYZ micromanipulator stage.

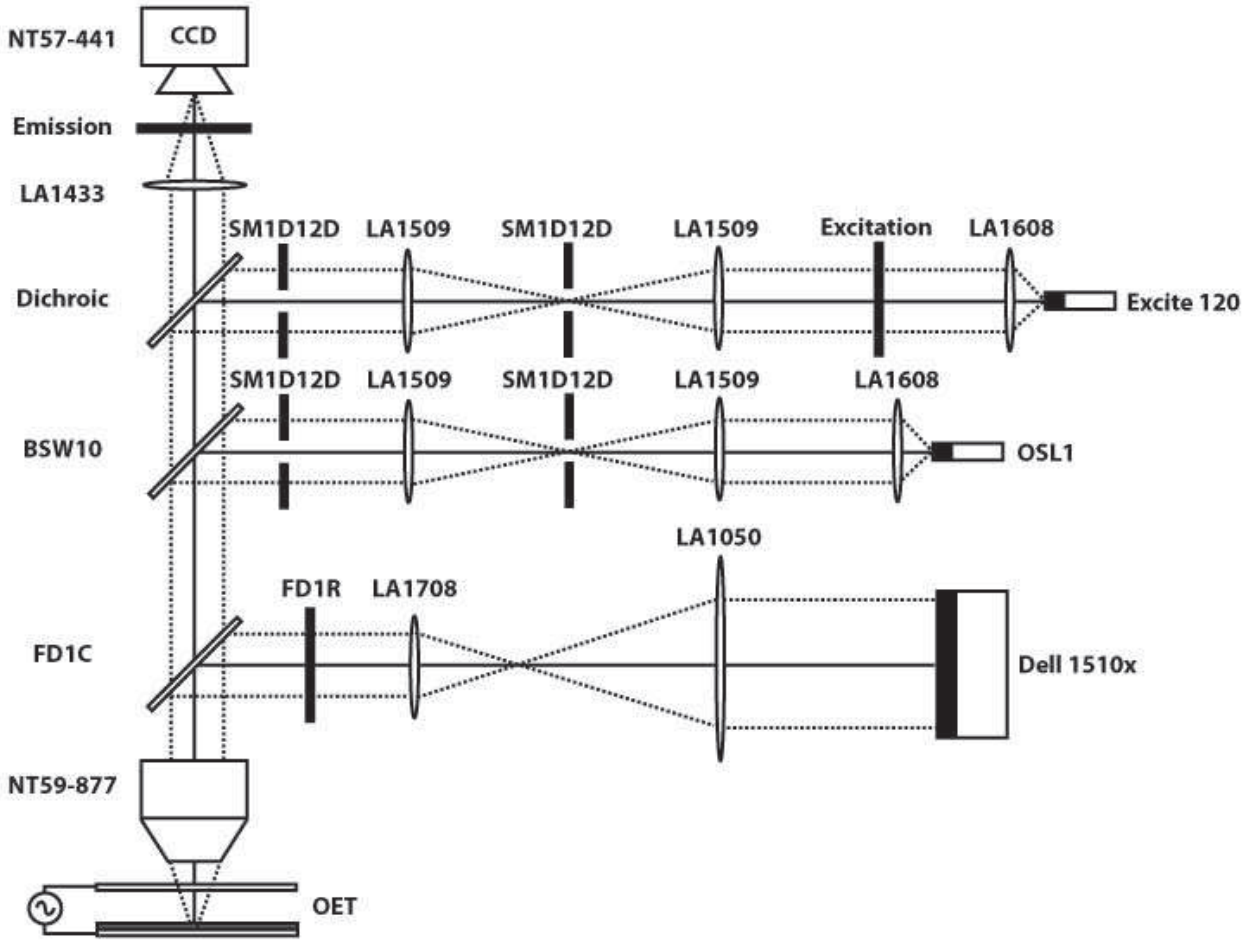

Figure C.2: Schematic of optical train for standard OET/OEW setup using parts list in Table C.1. Not to scale.

Quantity	Part Number	Description	Price	Total
	Thor Labs			
2	P14	1.5" 14" Post	$77.00	$154.00
1	P8	1.5" 8" Post	$53.60	$53.60
2	PB1	Post Base	$23.70	$47.40
5	C1526	30 mm mounting post adaptor	$71.00	$355.00
1	C1501	Large P-Series Post Clamp	$61.00	$61.00
20	ER8	8" Cage Rod	$9.95	$199.00
4	ER6	6" Cage Rod	$8.30	$33.20
1	LCP02	30 mm to 60 mm Cage Plate Adapter	$37.80	$37.80
4	CP02	SM1 Threaded 30 mm Cage Plate	$15.70	$62.80
3	C4W	30 mm Cage System Cube	$57.90	$173.70
3	B1C	Blank Cover Plate with Rubber O-Ring	$15.30	$45.90
3	B5C	1" Cage Cube Optic Mount	$30.50	$91.50
2	B4C	Rotatable Kinematic Cage Cube Platform	$91.70	$183.40
1	B3C	Rotatable Cage Cube Platform	$23.20	$23.20
11	STK01	Cage Assembly Optic Swapper Plate	$35.70	$392.70
2	AD8F	SM1 Adapter for Ø8 mm Collimators	$27.50	$55.00
3	LCP01	60 mm Threaded Cage Plate	$31.30	$93.90
1	SM1E60	6" Extension Tube for SM1 Lens Tube	$42.00	$42.00
1	SM1L30	SM1 Lens Tube, 3" Long	$25.75	$25.75
4	SM1D12D	Ring-Activated SM1 Iris Diaphragm	$58.10	$232.40
1	MB12	Aluminum Breadboard, 12" x 12" x 1/2"	$161.10	$161.10
1	L490	7" x 4" Heavy Duty Lab Jack	$550.80	$550.80
6	TR4	1/2" x 4" Post	$5.87	$35.22
3	RA90	Right Angle Post Clamp, Fixed 90 Degree Adapter	$9.93	$29.79
4	LA1509	N-BK7 Plano-Convex Lens, Ø1", f = 100.0 mm, Uncoated	$18.50	$74.00
1	LA1433	N-BK7 Plano-Convex Lens, Ø1", f = 150.0 mm, Uncoated	$18.00	$18.00
2	LA1608	N-BK7 Plano-Convex Lens, Ø1", f = 75.0 mm, Uncoated	$19.20	$38.40
1	BSW10	1" UVFS Broadband Beamsplitter, Coating: 400-700 nm, t=5 mm	$102.00	$102.00
1	FD1C	1" Subtractive Dichroic Color Filter, Cyan	$23.20	$23.20
1	FD1R	1" Additive Dichroic Color Filter, Red	$23.20	$23.20
1	LA1050	N-BK7 Plano-Convex Lens, Ø2", f = 100.0 mm, Uncoated	$25.80	$25.80
1	LA1708	N-BK7 Plano-Convex Lens, Ø1", f = 200.0 mm, Uncoated	$17.80	$17.80
1	OSL1	High Intensity Fiber Coupled Light Source, 110-120VAC	$497.50	$497.50
1	PT3	1" XYZ Translation Stage	$829.90	$829.90
1	T3788	BNC Adapters - BNC To Test Clips	$11.90	$11.90
	Edmund Optics			
1	NT57-441	Sony XCD-X710 1/3" Color Firewire.a Camera	$1,583.00	$1,583.00
1	NT59-877	10X EO M Plan Apo Long Working Distance Infinity-Corrected	$675.00	$675.00
	Newport			
1	CB-2	Construction Bases, 2.5 x 3.5 in.	$87.90	$87.90
	Dell.com			
1		Dell 1510X Projector	$809.00	$809.00
	Scholar's Work Station			
1	Computer w/firewire		$1,000.00	$1,000.00
	Agilent			
1		33210A Function / Arbitrary Waveform Generator, 10 MHz	$1,256.00	$1,256.00
	Quater Research			
2		XYZ 300 TR	$475.00	$950.00
	EXFO			
1		Excite 120	$4,000.00	$4,000.00
			Sum	$15,162.76
			Tax	$1,478.37
			Total	**$16,641.13**

Table C.1: OET/OEW parts list for fluorescent 10x setup.

Bibliography

[1] J. Kilby, *What If He Had Gone on Vacation*, vol. http://www.ti.com/corp/docs/kilbyctr/vacation.shtml. Texas Instruments, 2011.

[2] A. Manz, N. Graber, and H. Widmer, "Miniaturized total chemical analysis systems: A novel concept for chemical sensing," *Sensors and Actuators B: Chemical*, vol. 1, no. 1-6, pp. 244 – 248, 1990.

[3] T. Thorsen, S. J. Maerkl, and S. R. Quake, "Microfluidic large-scale integration," *Science*, vol. 298, no. 5593, pp. 580–584, 2002.

[4] T. Junno, K. Deppert, L. Montelius, and L. Samuelson, "Controlled manipulation of nanoparticles with an atomic force microscope," *Applied Physics Letters*, vol. 66, no. 26, pp. 3627–3629, 1995.

[5] Y. Li, C. Dalton, J. Crabtree, G. Nilsson, and K. V. I. S. Kaler, "Continuous dielectrophoretic cell separation microfluidic device," *Lab on a Chip*, vol. 7, pp. 239–248, 2007.

[6] A. B. Fuchs, A. Romani, D. Freida, G. Medoro, M. Abonnenc, L. Altomare, I. Chartier, D. Guergour, C. Villiers, P. N. Marche, M. Tartagni, R. Guerrieri, F. Chatelain, and N. Manaresi, "Electronic sorting and recovery of single live cells from microlitre sized samples," *Lab on a Chip*, vol. 6, no. 1, pp. 121–126, 2006.

[7] G. Roman, Y. Chen, P. Viberg, A. Culbertson, and C. Culbertson, "Single-cell manipulation and analysis using microfluidic devices," *Analytical and Bioanalytical Chemistry*, vol. 387, no. 1, pp. 9–12, 2007.

[8] A. Ashkin, J. M. Dziedzic, J. E. Bjorkholm, and S. Chu, "Observation of a single-beam gradient force optical trap for dielectric particles," *Opt. Lett.*, vol. 11, pp. 288–290, May 1986.

[9] D. G. Grier, "A revolution in optical manipulation," *Nature*, vol. 424, no. 6950, pp. 810–816, 2003.

[10] S. Rao, S. Blint, B. Cossins, V. Guallar, and D. Petrov, "Raman study of mechanically induced oxygenation state transition of red blood cells using optical tweezers," *Biophysical Journal*, vol. 96, no. 1, pp. 209–216, 2009.

[11] K. C. Neuman and A. Nagy, "Single-molecule force spectroscopy: optical tweezers, magnetic tweezers and atomic force microscopy," *Nat Meth*, vol. 5, no. 6, pp. 491–505, 2008.

[12] A. Ashkin, J. M. Dziedzic, and T. Yamane, "Optical trapping and manipulation of single cells using infrared laser beams," *Nature*, vol. 330, no. 6150, pp. 769–771, 1987.

[13] E. R. Dufresne and D. G. Grier, "Optical tweezer arrays and optical substrates created with diffractive optics," *Review of Scientific Instruments*, vol. 69, no. 5, pp. 1974–1977, 1998.

[14] K. C. Neuman, E. H. Chadd, G. F. Liou, K. Bergman, and S. M. Block, "Characterization of photodamage to escherichia coli in optical traps," vol. 77, no. 5, pp. 2856–2863, 1999.

[15] S. K. Mohanty, A. Rapp, S. Monajembashi, P. K. Gupta, and K. O. Greulich, "Comet assay measurements of dna damage in cells by laser microbeams and trapping beams with wavelengths spanning a range of 308 nm to 1064 nm," *Radiation Research*, vol. 157, no. 4, pp. 378–385, 2002.

[16] A. N. Grigorenko, N. W. Roberts, M. R. Dickinson, and Y. Zhang, "Nanometric optical tweezers based on nanostructured substrates," *Nat Photon*, vol. 2, no. 6, pp. 365–370, 2008.

[17] M. Xiaoyu and L. Y. Lin, "Trapping and manipulation of biological particles through a plasmonic platform," *IEEE Journal of Selected Topics in Quantum Electronics*, vol. 13, no. 6, pp. 1655–1662, 2007.

[18] P. Y. Chiou, A. T. Ohta, and M. C. Wu, "Massively parallel manipulation of single cells and microparticles using optical images," *Nature*, vol. 436, no. 7049, pp. 370–372, 2005.

[19] A. T. Ohta, P. Y. Chiou, T. H. Han, J. C. Liao, U. Bhardwaj, E. R. B. McCabe, F. Yu, R. Sun, and M. C. Wu, "Dynamic cell and microparticle control via optoelectronic tweezers," *Journal of Microelectromechanical Systems*, vol. 16, no. 3, pp. 491–499, 2007.

[20] H.-Y. Hsu, A. T. Ohta, P.-Y. Chiou, A. Jamshidi, S. L. Neale, and M. C. Wu, "Phototransistor-based optoelectronic tweezers for dynamic cell manipulation in cell culture media," *Lab on a Chip*, vol. DOI: 10.1039/b906593h, 2009.

[21] P. Y. Chiou, A. T. Ohta, A. Jamshidi, H.-Y. Hsu, J. B. Chou, and M. C. Wu, "Light-actuated ac electroosmosis for optical manipulation of nanoscale particles," in *Proceedings of Solid-State Sensor, Actuator, and Microsystems Workshop*, (Hilton Head), pp. 56–59, 2006.

[22] S. K. Cho, H. J. Moon, and C. J. Kim, "Creating, transporting, cutting, and merging liquid droplets by electrowetting-based actuation for digital microfluidic circuits," *Journal of Microelectromechanical Systems*, vol. 12, no. 1, pp. 70–80, 2003.

[23] M. G. Pollack, A. D. Shenderov, and R. B. Fair, "Electrowetting-based actuation of droplets for integrated microfluidics," *Lab on a Chip*, vol. 2, no. 2, pp. 96–101, 2002.

[24] Y.-H. Chang, G.-B. Lee, F.-C. Huang, Y.-Y. Chen, and J.-L. Lin, "Integrated polymerase chain reaction chips utilizing digital microfluidics," *Biomedical Microdevices*, vol. 8, no. 3, pp. 215–225, 2006.

[25] H. Moon, A. R. Wheeler, R. L. Garrell, J. A. Loo, and C. J. Kim, "An integrated digital microfluidic chip for multiplexed proteomic sample preparation and analysis by maldi-ms," *Lab on a Chip*, vol. 6, no. 9, pp. 1213–1219, 2006.

[26] J. R. Millman, K. H. Bhatt, B. G. Prevo, and O. D. Velev, "Anisotropic particle synthesis in dielectrophoretically controlled microdroplet reactors," *Nature Materials*, vol. 4, no. 1, pp. 98–102, 2005.

[27] Y. Li, W. Parkes, L. I. Haworth, A. A. Stokes, K. R. Muir, P. Li, A. J. Collin, N. G. Hutcheon, R. Henderson, B. Rae, and A. J. Walton, "Anodic ta2o5 for cmos compatible low voltage electrowetting-on-dielectric device fabrication," *Solid-State Electronics*, vol. 52, no. 9, pp. 1382–1387, 2008.

[28] P. Y. Chiou, H. Moon, H. Toshiyoshi, C. J. Kim, and M. C. Wu, "Light actuation of liquid by optoelectrowetting," *Sensors and Actuators a-Physical*, vol. 104, no. 3, pp. 222–228, 2003.

[29] P. Y. Chiou, S.-Y. Park, and M. C. Wu, "Continuous optoelectrowetting for picoliter droplet manipulation," *Applied Physics Letters*, vol. 93, no. 22, p. 221110, 2008.

[30] T. B. Jones, *Electromechanics of Particles*. Cambridge: Cambridge University Press, 1995.

[31] K. Svoboda and S. M. Block, "Biological applications of optical forces," *Annual Review of Biophysics and Biomolecular Structure*, vol. 23, pp. 247–285, 1994.

[32] D. Shaw, *Introduction to Colloid and Surface Chemistry*, vol. 1. Burlington, MA: Butterworth Heinemann, 1992.

[33] J. Lyklema, *Fundamentals of Interface and Colloid Science*, vol. 2. London: Academic Press, 1991.

[34] P. Wang, Z. L. Chen, and H. C. Chang, "A new electro-osmotic pump based on silica monoliths," *Sensors and Actuators B-Chemical*, vol. 113, no. 1, pp. 500–509, 2006.

[35] A. Ramos, H. Morgan, N. G. Green, and A. Castellanos, "Ac electric-field-induced fluid flow in microelectrodes," *Journal of Colloid and Interface Science*, vol. 217, no. 2, pp. 420–422, 1999.

[36] A. Ramos, H. Morgan, N. G. Green, and A. Castellanos, "Ac electrokinetics: a review of forces in microelectrode structures," *Journal of Physics D-Applied Physics*, vol. 31, no. 18, pp. 2338–2353, 1998.

[37] A. Castellanos, A. Ramos, A. Gonzalez, N. G. Green, and H. Morgan, "Electrohydrodynamics and dielectrophoresis in microsystems: scaling laws," *Journal of Physics D-Applied Physics*, vol. 36, no. 20, pp. 2584–2597, 2003.

[38] A. Einstein, *Investigations on the Theory of Brownian Movement*. New York: Dover, 1956.

[39] A. Jamshidi, P. J. Pauzauskie, A. T. Ohta, P. Y. Chiou, H.-Y. Hsu, P. Yang, and M. C. Wu, "Semiconductor nanowire manipulation using optoelectronic tweezers," in *20th IEEE International Conference on Micro Electro Mechanical Systems (MEMS)*, (Kobe, Japan), 2007.

[40] A. Jamshidi, H. Y. Hsu, J. K. Valley, A. T. Ohta, S. Neale, and M. C. Wu, "Metallic nanoparticle manipulation using optoelectronic tweezers," in *22nd IEEE MEMS*, (Sorrento), 2009.

[41] H. Y. Hsu, A. T. Ohta, P. Y. Chiou, A. Jamshidi, and M. C. Wu, "Phototransistor-based optoelectronic tweezers for cell manipulation in highly conductive solution," in *The 14th International Conference on Solid-State Sensors, Actuators and Microsystems (Transducers 2007)*, (Lyon, France), 2007.

[42] V. Bahadur and S. V. Garimella, "An energy-based model for electrowetting-induced droplet actuation," *Journal of Micromechanics and Microengineering*, vol. 16, no. 8, pp. 1494–1503, 2006.

[43] F. Mugele and J. C. Baret, "Electrowetting: From basics to applications," *Journal of Physics-Condensed Matter*, vol. 17, no. 28, pp. R705–R774, 2005.

[44] P. C. Steptoe and R. G. Edwards, "Birth after the reimplantation of a human embryo," *Lancet*, vol. 2, no. 8085, p. 366, 1978.

[45] A. T. Kjellberg, P. Carlsson, and C. Bergh, "Randomized single versus double embryo transfer: obstetric and paediatric outcome and a cost-effectiveness analysis," *Hum Reprod*, vol. 21, no. 1, pp. 210–6, 2006.

[46] G. Kovalevsky and P. Patrizio, "High rates of embryo wastage with use of assisted reproductive technology: a look at the trends between 1995 and 2001 in the united states," *Fertil Steril*, vol. 84, no. 2, pp. 325–30, 2005.

[47] J. Reefhuis, M. A. Honein, L. A. Schieve, A. Correa, C. A. Hobbs, and S. A. Rasmussen, "Assisted reproductive technology and major structural birth defects in the united states," *Hum Reprod*, vol. 24, no. 2, pp. 360–6, 2009.

[48] A. K. Ludwig, K. Diedrich, and M. Ludwig, "The process of decision making in reproductive medicine," *Semin Reprod Med*, vol. 23, no. 4, pp. 348–53, 2005.

[49] S. A. R. T. www.sartcorsonline.com/, "Society of assisted reproductive technology (sart): Assisted reproductive success rates. national summary and fertility clinic reports. centers for disease control, usa.," 2007.

[50] T. Gurgan and A. Demirol, "Why and how should multiple pregnancies be prevented in assisted reproduction treatment programmes?," *Reprod Biomed Online*, vol. 9, no. 2, pp. 237–44, 2004.

[51] T. Bergh, A. Ericson, T. Hillensjo, K. G. Nygren, and U. B. Wennerholm, "Deliveries and children born after in-vitro fertilisation in sweden 1982-95: a retrospective cohort study," *Lancet*, vol. 354, no. 9190, pp. 1579–85, 1999.

[52] A. S. R. M. www.asrm.org, "American society of reproductive medicine: Frequently asked questions about infertility," 2009.

[53] C. D. C. www.cdc.gov/ART, "Assisted reproductive technology," no. September 8, 2009, 2009.

[54] Z. P. Nagy, D. Sakkas, and B. Behr, "Symposium: innovative techniques in human embryo viability assessment. non-invasive assessment of embryo viability by metabolomic profiling of culture media ('metabolomics')," *Reprod Biomed Online*, vol. 17, no. 4, pp. 502–7, 2008.

[55] C. M. Warner, P. W. Lampton, J. A. Newmark, and J. Cohen, "Symposium: innovative techniques in human embryo viability assessment. soluble human leukocyte antigen-g and pregnancy success," *Reprod Biomed Online*, vol. 17, no. 4, pp. 470–85, 2008.

[56] W. B. Schoolcraft, D. K. Gardner, M. Lane, T. Schlenker, F. Hamilton, and D. R. Meldrum, "Blastocyst culture and transfer: analysis of results and parameters affecting outcome in two in vitro fertilization programs," *Fertil Steril*, vol. 72, no. 4, pp. 604–9, 1999.

[57] S. W. Dessie, F. Rings, M. Holker, M. Gilles, D. Jennen, E. Tholen, V. Havlicek, U. Besenfelder, V. L. Sukhorukov, U. Zimmermann, J. M. Endter, M. A. Sirard, K. Schellander, and D. Tesfaye, "Dielectrophoretic behavior of in vitro-derived bovine metaphase ii oocytes and zygotes and its relation to in vitro embryonic developmental competence and mrna expression pattern," *Reproduction*, vol. 133, no. 5, pp. 931–946, 2007.

[58] T. B. Jones, *Electromechanics of Particles*. Cambridge: Cambridge University Press, 1995.

[59] S. Fiedler, S. G. Shirley, T. Schnelle, and G. Fuhr, "Dielectrophoretic sorting of particles and cells in a microsystem," *Analytical Chemistry*, vol. 70, no. 9, pp. 1909–1915, 1998.

[60] A. T. Ohta, P. Y. Chiou, T. H. Han, J. C. Liao, U. Bhardwaj, E. R. B. McCabe, F. Yu, R. Sun, and M. C. Wu, "Dynamic cell and microparticle control via optoelectronic tweezers," *Microelectromechanical Systems, Journal of*, vol. 16, no. 3, pp. 491–499, 2007.

[61] A. Jamshidi, P. J. Pauzauskie, P. J. Schuck, A. T. Ohta, P.-Y. Chiou, J. Chou, P. Yang, and M. C. Wu, "Dynamic manipulation and separation of individual semiconducting and metallic nanowires," *Nat Photon*, vol. 2, no. 2, pp. 86–89, 2008.

[62] P. A. Smith, C. D. Nordquist, T. N. Jackson, T. S. Mayer, B. R. Martin, J. Mbindyo, and T. E. Mallouk, "Electric-field assisted assembly and alignment of metallic nanowires," *Applied Physics Letters*, vol. 77, no. 9, pp. 1399–1401, 2000.

[63] H. Y. P. R. V. J. Gascoyne, P. and F. Becker, "Dielectrophoretic separation of mamallian cells studied by computerized image analysis.," *Measurement Science & Technology*, vol. 3, pp. 439–445, 1992.

[64] X. Wang, F. F. Becker, and P. R. Gascoyne, "Membrane dielectric changes indicate induced apoptosis in hl-60 cells more sensitively than surface phosphatidylserine expression or dna fragmentation," *Biochim Biophys Acta*, vol. 1564, no. 2, pp. 412–20, 2002.

[65] Y. Huang, R. Holzel, R. Pethig, and X. B. Wang, "Differences in the ac electrodynamics of viable and non-viable yeast cells determined through combined dielectrophoresis and electrorotation studies," *Phys Med Biol*, vol. 37, no. 7, pp. 1499–517, 1992.

[66] Y. Huang, X. B. Wang, F. F. Becker, and P. R. Gascoyne, "Introducing dielectrophoresis as a new force field for field-flow fractionation," *Biophys J*, vol. 73, no. 2, pp. 1118–29, 1997.

[67] J. Yang, Y. Huang, X. B. Wang, F. F. Becker, and P. R. Gascoyne, "Cell separation on microfabricated electrodes using dielectrophoretic/gravitational field-flow fractionation," *Anal Chem*, vol. 71, no. 5, pp. 911–8, 1999.

[68] F. F. Becker, X. B. Wang, Y. Huang, R. Pethig, J. Vykoukal, and P. R. Gascoyne, "Separation of human breast cancer cells from blood by differential dielectric affinity," *Proc Natl Acad Sci U S A*, vol. 92, no. 3, pp. 860–4, 1995.

[69] P. Y. Chiou, A. T. Ohta, and M. C. Wu, "Massively parallel manipulation of single cells and microparticles using optical images," *Nature*, vol. 436, no. 7049, pp. 370–2, 2005.

[70] U. Lei, C. W. Huang, J. Chen, C. Y. Yang, Y. J. Lo, A. Wo, C. F. Chen, and T. W. Fung, "A travelling wave dielectrophoretic pump for blood delivery," *Lab on a Chip*, vol. 9, no. 10, pp. 1349–1356, 2009.

[71] N. Manaresi, A. Romani, G. Medoro, L. Altomare, A. Leonardi, M. Tartagni, and R. Guerrieri, "A cmos chip for individual cell manipulation and detection," *Solid-State Circuits, IEEE Journal of*, vol. 38, no. 12, pp. 2297–2305, 2003.

[72] W. Choi, J. S. Kim, D. H. Lee, K. K. Lee, D. B. Koo, and J. K. Park, "Dielectrophoretic oocyte selection chip for in vitro fertilization," *Biomedical Microdevices*, vol. 10, no. 3, pp. 337–345, 2008.

[73] R. K. Creasy, R. Resnik, and J. D. Iams, *Creasy and Resnik's maternal-fetal medicine : principles and practice*. Philadelphia, PA: Saunders/Elsevier, 2009.

[74] D. J. Benos, "Developmental changes in epithelial transport characteristics of preimplantation rabbit blastocysts," *The Journal of Physiology*, vol. 316, no. 1, pp. 191–202, 1981.

[75] J. F. Palmer and C. Slack, "Some bio-electric parameters of early xenopus embryos," *Journal of Embryology and Experimental Morphology*, vol. 24, no. NOV, pp. 535–&, 1970.

[76] J. D. Biggers, "Reflections on the culture of the preimplantation embryo," *International Journal of Developmental Biology*, vol. 42, no. 7, pp. 879–884, 1998.

[77] Y. Ho, K. Wigglesworth, J. J. Eppig, and R. M. Schultz, "Preimplantation development of mouse embryos in ksom: augmentation by amino acids and analysis of gene expression," *Mol Reprod Dev*, vol. 41, no. 2, pp. 232–8, 1995.

[78] J. A. Lawitts and J. D. Biggers, "Culture of preimplantation embryos," *Methods Enzymol*, vol. 225, pp. 153–64, 1993.

[79] G. T. Erbach, J. A. Lawitts, V. E. Papaioannou, and J. D. Biggers, "Differential growth of the mouse preimplantation embryo in chemically defined media," *Biology of Reproduction*, vol. 50, no. 5, pp. 1027–1033, 1994.

[80] F. Devreker and K. Hardy, "Effects of glutamine and taurine on preimplantation development and cleavage of mouse embryos in vitro," *Biology of Reproduction*, vol. 57, no. 4, pp. 921–928, 1997.

[81] M. Kamjoo, D. R. Brison, and S. J. Kimber, "Apoptosis in the preimplantation mouse embryo: effect of strain difference and in vitro culture," *Mol Reprod Dev*, vol. 61, no. 1, pp. 67–77, 2002.

[82] J. A. Lawitts and J. D. Biggers, "Overcoming the 2-cell block by modifying standard components in a mouse embryo culture medium," *Biology of Reproduction*, vol. 45, no. 2, pp. 245–251, 1991.

[83] M. J. Goddard and H. P. M. Pratt, "Control of events during early cleavage of the mouse embryo: an analysis of the 2-cell block," *Journal of Embryology and Experimental Morphology*, vol. 73, no. 1, pp. 111–133, 1983.

[84] J. M. Robl, J. K. Lohse-Heideman, and N. L. First, "Strain differences in early mouse embryo development in vitro: Role of the nucleus," *Journal of Experimental Zoology*, vol. 247, no. 3, pp. 251–256, 1988.

[85] P. Bowman and A. McLaren, "Viability and growth of mouse embryos after in vitro culture and fusion," *Journal of Embryology and Experimental Morphology*, vol. 23, no. 3, pp. 693–704, 1970.

[86] D. J. Ecker, P. Stein, Z. Xu, C. J. Williams, G. S. Kopf, W. B. Bilker, T. Abel, and R. M. Schultz, "Long-term effects of culture of preimplantation mouse embryos on behavior," *Proc Natl Acad Sci U S A*, vol. 101, no. 6, pp. 1595–600, 2004.

[87] S. Boitano, E. R. Dirksen, and M. J. Sanderson, "Intercellular propagation of calcium waves mediated by inositol trisphosphate," *Science*, vol. 258, no. 5080, pp. 292–295, 1992.

[88] K. Braet, C. Mabilde, L. Cabooter, G. Rapp, and L. Leybaert, "Electroporation loading and photoactivation of caged insp3: tools to investigate the relation between cellular atp release in response to intracellular insp3 elevation," *Journal of Neuroscience Methods*, vol. 132, no. 1, pp. 81–89, 2004.

[89] J. C. Weaver, "Electroporation of cells and tissues," *Plasma Science, IEEE Transactions on*, vol. 28, no. 1, pp. 24–33, 2000.

[90] E. Neumann, M. Schaeferridder, Y. Wang, and P. H. Hofschneider, "Gene-transfer into mouse lyoma cells by electroporation in high electric-fields," *Embo Journal*, vol. 1, no. 7, pp. 841–845, 1982.

[91] J. A. Lundqvist, F. Sahlin, M. A. I. Aberg, A. Stromberg, P. S. Eriksson, and O. Orwar, "Altering the biochemical state of individual cultured cells and organelles with ultramicroelectrodes," *Proceedings of the National Academy of Sciences of the United States of America*, vol. 95, no. 18, pp. 10356–10360, 1998.

[92] H. Q. He, D. C. Chang, and Y. K. Lee, "Using a micro electroporation chip to determine the optimal physical parameters in the uptake of biomolecules in hela cells," *Bioelectrochemistry*, vol. 70, no. 2, pp. 363–368, 2007.

[93] T. Jain and J. Muthuswamy, "Microsystem for transfection of exogenous molecules with spatio-temporal control into adherent cells," *Biosensors and Bioelectronics*, vol. 22, no. 6, pp. 863–870, 2007.

[94] L. A. MacQueen, M. D. Buschmann, and M. R. Wertheimer, "Gene delivery by electroporation after dielectrophoretic positioning of cells in a non-uniform electric field," *Bioelectrochemistry*, vol. 72, no. 2, pp. 141–148, 2008.

[95] M. Khine, C. Ionescu-Zanetti, A. Blatz, L. P. Wang, and L. P. Lee, "Single-cell electroporation arrays with real-time monitoring and feedback control," *Lab on a Chip*, vol. 7, no. 4, pp. 457–462, 2007.

[96] A. Valero, J. N. Post, J. W. van Nieuwkasteele, P. M. ter Braak, W. Kruijer, and A. van den Berg, "Gene transfer and protein dynamics in stem cells using single cell electroporation in a microfluidic device," *Lab on a Chip*, vol. 8, pp. 62–67, 2008.

[97] Y. Huang and B. Rubinsky, "Microfabricated electroporation chip for single cell membrane permeabilization," *Sensors and Actuators a-Physical*, vol. 89, no. 3, pp. 242–249, 2001.

[98] J. S. Soughayer, T. Krasieva, S. C. Jacobson, J. M. Ramsey, B. J. Tromberg, and N. L. Allbritton, "Characterization of cellular optoporation with distance," *Anal. Chem.*, vol. 72, no. 6, pp. 1342–1347, 2000.

[99] S. L. Gac, E. Zwaan, A. v. d. Berg, and C.-D. Ohl, "Sonoporation of suspension cells with a single cavitation bubble in a microfluidic confinement," *Lab on a Chip*, vol. 7, no. 12, pp. 1666–1672, 2007.

[100] U. K. Tirlapur and K. Konig, "Cell biology - targeted transfection by femtosecond laser," *Nature*, vol. 418, no. 6895, pp. 290–291, 2002.

[101] T.-H. Wu, S. Kalim, C. Callahan, M. Teitell, and P.-Y. Chiou, "Light image patterned molecular delivery into live cells using gold particle coated substrate," in *IEEE/LEOS Summer Topical Meetings, 2008 Digest of the*, pp. 195–196, 2008.

[102] M. Yamada, J. Kobayashi, M. Yamato, M. Seki, and T. Okano, "Millisecond treatment of cells using microfluidic devices via two-step carrier-medium exchange," *Lab on a Chip*, vol. 8, no. 5, pp. 772–778, 2008.

[103] P. L. Felgner, T. R. Gadek, M. Holm, R. Roman, H. W. Chan, M. Wenz, J. P. Northrop, G. M. Ringold, and M. Danielsen, "Lipofection - a highly efficient, lipid-mediated dna-transfection procedure," *Proceedings of the National Academy of Sciences of the United States of America*, vol. 84, no. 21, pp. 7413–7417, 1987.

[104] A. Adamo and K. F. Jensen, "Microfluidic based single cell microinjection," *Lab on a Chip*, vol. 8, no. 8, pp. 1258–1261, 2008.

[105] J. C. Weaver and Y. A. Chizmadzhev, "Theory of electroporation: A review," *Bioelectrochemistry and Bioenergetics*, vol. 41, no. 2, pp. 135–160, 1996.

[106] W. K. Neu, "Molecular basis and energetics of electroporation," *UC Berkeley Electroporation Lectures*, 2009.

[107] E. N. Axel, M. G. Jean, T. Bernard, R. Hongji, D. Claude, C. M. Laurette, D. Guy, and W. S. Gary, "Diffusion coefficient of dna molecules during free solution electrophoresis," *ELECTROPHORESIS*, vol. 22, no. 12, pp. 2424–2432, 2001.

[108] P. Y. Chiou, A. T. Ohta, and M. C. Wu, "Massively parallel manipulation of single cells and microparticles using optical images," *Nature*, vol. 436, no. 7049, pp. 370–372, 2005.

[109] V. L. Sukhorukov, R. Reuss, D. Zimmermann, C. Held, K. J. Mller, M. Kiesel, P. Gener, A. Steinbach, W. A. Schenk, E. Bamberg, and U. Zimmermann, "Surviving high-intensity field pulses: Strategies for improving robustness and performance of electrotransfection and electrofusion," *Journal of Membrane Biology*, vol. 206, no. 3, pp. 187–201, 2005.

[110] V. L. Sukhorukov, H. Mussauer, and U. Zimmermann, "The effect of electrical deformation forces on the electropermeabilization of erythrocyte membranes in low- and high-conductivity media," *Journal of Membrane Biology*, vol. 163, no. 3, pp. 235–245, 1998.

[111] J. S. Crane and H. A. Pohl, "Theoretical models of cellular dielectrophoresis," *Journal of Theoretical Biology*, vol. 37, no. 1, pp. 15–41, 1972.

[112] H. Becker, "Hype, hope and hubris: the quest for the killer application in microfluidics," *Lab on a Chip*, vol. 9, no. 15, pp. 2119–2122, 2009.

[113] S. K. Cho, Y. J. Zhao, and C. J. Kim, "Concentration and binary separation of micro particles for droplet-based digital microfluidics," *Lab on a Chip*, vol. 7, no. 4, pp. 490–498, 2007.

[114] A. R. Wheeler, "Chemistry: Putting electrowetting to work," *Science*, vol. 322, no. 5901, pp. 539–540, 2008.

[115] W. Yizhong and et al., "Efficient in-droplet separation of magnetic particles for digital microfluidics," *Journal of Micromechanics and Microengineering*, vol. 17, no. 10, p. 2148, 2007.

[116] S.-K. Fan, P.-W. Huang, T.-T. Wang, and Y.-H. Peng, "Cross-scale electric manipulations of cells and droplets by frequency-modulated dielectrophoresis and electrowetting," *Lab on a Chip*, vol. 8, no. 8, pp. 1325–1331, 2008.

[117] Y. Zhao, U.-C. Yi, and S. K. Cho, "Microparticle concentration and separation by traveling-wave dielectrophoresis (twdep) for digital microfluidics," *Microelectromechanical Systems, Journal of*, vol. 16, no. 6, pp. 1472–1481, 2007.

[118] G. J. Shah, A. T. Ohta, E. P. Y. Chiou, M. C. Wu, and C.-J. C. J. Kim, "Ewod-driven droplet microfluidic device integrated with optoelectronic tweezers as an automated platform for cellular isolation and analysis," *Lab on a Chip*, vol. 9, no. 12, pp. 1732–1739, 2009.

[119] S. N. Pei, J. K. Valley, S. L. Neale, A. Jamshidi, H.-Y. Hsu, and M. C. Wu, "Light-actuated digital microfluidics for large-scale, parallel manipulation of arbitrarily sized droplets," in *Micro Electro Mechanical Systems (MEMS), 2010 IEEE 23rd International Conference on*, pp. 252–255.

[120] T. B. Jones, "On the relationship of dielectrophoresis and electrowetting," *Langmuir*, vol. 18, no. 11, pp. 4437–4443, 2002.

[121] M. A. M. Gijs, "Magnetic bead handling on-chip: new opportunities for analytical applications," *Microfluidics and Nanofluidics*, vol. 1, no. 1, pp. 22–40, 2004.

[122] J. F. Edd, D. Di Carlo, K. J. Humphry, S. Koster, D. Irimia, D. A. Weitz, and M. Toner, "Controlled encapsulation of single-cells into monodisperse picolitre drops," *Lab on a Chip*, vol. 8, no. 8, pp. 1262–1264, 2008.

[123] S. Koster, F. E. Angile, H. Duan, J. J. Agresti, A. Wintner, C. Schmitz, A. C. Rowat, C. A. Merten, D. Pisignano, A. D. Griffiths, and D. A. Weitz, "Drop-based microfluidic devices for encapsulation of single cells," *Lab on a Chip*, vol. 8, no. 7, pp. 1110–1115, 2008.

[124] M. Y. He, J. S. Edgar, G. D. M. Jeffries, R. M. Lorenz, J. P. Shelby, and D. T. Chiu, "Selective encapsulation of single cells and subcellular organelles into picoliter- and femtoliter-volume droplets," *Analytical Chemistry*, vol. 77, no. 6, pp. 1539–1544, 2005.

[125] K. C. Neuman, E. H. Chadd, G. F. Liou, K. Bergman, and S. M. Block, "Characterization of photodamage to escherichia coli in optical traps," *Biophysical Journal*, vol. 77, no. 5, pp. 2856–2863, 1999.

[126] H.-Y. Hsu, A. T. Ohta, P.-Y. Chiou, A. Jamshidi, S. L. Neale, and M. C. Wu, "Phototransistor-based optoelectronic tweezers for dynamic cell manipulation in cell culture media," *Lab on a Chip*, vol. 10, no. 2, pp. 165–172.